

FUNDAMENTAL UNDERSTANDING OF THE INTERFACIAL BEHAVIOR OF MOLTEN SALT BASED NANOFLUIDS ON SOLID SURFACES

By

ARGYRIOS ANAGNOSTOPOULOS

A thesis submitted to
The University of Birmingham
for the degree of
DOCTOR OF PHILOSOPHY

School of Chemical Engineering
College of Engineering and Physical Sciences
The University of Birmingham
February 2020

UNIVERSITY OF
BIRMINGHAM

University of Birmingham Research Archive

e-theses repository

This unpublished thesis/dissertation is copyright of the author and/or third parties. The intellectual property rights of the author or third parties in respect of this work are as defined by The Copyright Designs and Patents Act 1988 or as modified by any successor legislation.

Any use made of information contained in this thesis/dissertation must be in accordance with that legislation and must be properly acknowledged. Further distribution or reproduction in any format is prohibited without the permission of the copyright holder.

ABSTRACT

The main issues of molten salts in concentrated solar power plants are their poor thermophysical properties and corrosion issues. To improve their properties nanoparticles are doped in molten salts. These suspended particles have an effect not only on the thermal, but also other properties such as viscosity and wettability, the latter having often been overlooked. In this work molten nitrate salts are doped with amorphous SiO_2 and graphite particles. A series of contact angle measurements are conducted to study the effects of nanoparticle concentration, composition, particle geometry, temperature and surface type. A small fraction of nanoparticles leads to a shift of the transition from non-wetting to wetting at higher temperatures. Furthermore, wettability studies on different surfaces provide insights into the physiochemical mechanism of molten salt corrosion. Molecular Dynamics simulations of the nitrate salts-based silica nanofluids are also conducted. Novel interatomic parameters are calculated for the molten nitrate salts as well as the $\alpha\text{-SiO}_2$ and are used to predict the wetting behavior of the molten NaNO_3 and KNO_3 and their mixtures with and without $\alpha\text{-SiO}_2$ nanoparticles, in order to provide a better understanding of the wetting behavior of molten salt based nanofluids.

ACKNOWLEDGEMENT

I would like to express my great appreciation to my lead supervisor Professor Yulong Ding. He gave me the opportunity to work in the emerging field of energy storage in a large group where state of art collaborative research on the field is conducted. I am also very grateful to Dr. Alessio Alexiadis my co-supervisor for his guidance in terms of molecular modelling. Our long conversations on materials science in the molecular scale were very important for me to develop an understanding of the scope of conducting research in the atom scale. I would also like to thank specifically Dr. Helena Navarro for always being there to help me with the experiments conducted during my doctoral research, listening to my concerns and providing tons of advices and Dr. Yaroslav Grosu for several thoughtful discussions in the area of nanofluids and material interfaces and suggestions on how to use my knowledge to tackle new problems. Additionally, I would also like to thank Dr. Sonia Fereres who gave this research work a more practical note and Anabel Palacios for allowing me to use some of her data in this work and writing several publications together. Finally, I would like foremostly to thank my parents for raising me up to the task and providing alongside my girlfriend constant emotional support throughout the duration of these studies.

Table of Contents

ABSTRACT	i
ACKNOWLEDGEMENT	iii
List of Figures.....	viii
List of Tables.....	xiv
List of Abbreviations	xv
List of Publications	xvi
Chapter 1 Introduction.....	1
Chapter 2 Literature Review.....	11
2.1 Molten salt nanofluids: Controversies	11
2.1.1 Controversies in property measurements.....	11
2.1.2 Nanoparticle Agglomeration Prevention	13
2.1.3 Stability Studies	15
2.2 The Effect of wettability on corrosion	18
2.3 The Effect of wettability on composite materials performance	23
2.4 Studies on the wetting and surface tension of molten salts.....	28
2.5 Molecular Simulations of Contact angle of Nanodroplets.....	32
2.5.1 Introduction and Recent Advances.....	32
2.5.2 Studies on finite size effects	34
2.5.3 Studies on systematic errors in contact angle calculations.....	37
2.6 Molecular Simulation of Molten Salts	38

2.6.1	Structure	38
2.6.2	Surface Tension and Wettability	40
2.7	Molecular Simulation of wetting of Nanofluids.....	44
2.8	Summary.....	48
Chapter 3	Materials and Methods	50
3.1	Materials used in Experiments	50
3.2	Sample Preparation	52
3.3	Experimental Methods	54
3.3.1	Contact Angle	54
3.3.2	Rheometer.....	56
3.3.3	Differential Scanning Calorimetry (DSC)	58
3.3.4	X-ray Diffraction (XRD).....	58
3.4	Molecular Simulations	59
3.4.1	Theory	60
3.4.2	Extracting Variables.....	68
Chapter 4	Experimental Results.....	79
4.1	Effect of Nanoparticle addition on the Wetting and Rheological Properties of Solar Salt-SiO ₂	79
4.1.1	Contact Angle Results	80
4.1.2	Viscosity results.....	82
4.1.3	Discussion	84
4.2	Effect of Surface Type on the Wetting behavior of Solar Salt	93

4.3	Inhibition through graphitization of structural materials from hot corrosion by molten $\text{Li}_2\text{CO}_3\text{-Na}_2\text{CO}_3\text{-K}_2\text{CO}_3$ salt for concentrated solar power	96
4.3.1	Corrosion Inhibition Results.....	96
4.3.2	Wettability studies on graphitized surfaces.....	97
4.4	CA of NaNO_3 , KNO_3 and LiNO_3 on MgO (1 1 0)	102
4.5	Effect of particle size on the CA of MSNFs. A study on the wettability of graphite doped Solar Salt.....	106
Chapter 5	Molecular Dynamics Simulations.....	111
5.1	Development of Simplified Force Field parameters for the simulation of molten nitrate salt mixtures.....	111
5.1.1	Advantages of Lennard-Jones force fields in cross-term interactions.	111
5.1.2	Lennard-Jones Parameters for simulation of Solar Salt	112
5.1.3	Prediction of the Local-Structures of NaNO_3 and KNO_3	116
5.1.4	Prediction of the Transport Properties and Surface Tension of molten nitrate salts	119
5.1.5	Novel Lennard-Jones Parameters for simulation of Amorphous Silica	124
5.1.6	Amorphous Silica Simulation details.....	126
5.1.7	Prediction of the Local Structure of Amorphous Silica.....	127
5.1.8	Prediction of Bulk Properties of $\alpha\text{-SiO}_2$	130
5.1.9	Summary	131
5.2	Application of the new Force-Field parameters in Molten Salt/Nanoparticle interface.....	133

5.3 Wettability of NaNO ₃ and KNO ₃ on MgO and Carbon Surfaces – Understanding the Substrate and the Length Scale Effects.....	138
5.3.1 Introduction.....	138
5.3.2 Simulation details	140
5.3.3 Experimental Results.....	148
5.3.4 Simulation Results.....	149
5.3.5 Prediction of Molten Salt Properties related to Wettability	150
5.3.6 Influence of Drop Size and Temperature	151
5.3.7 Contact Angle and Work of Adhesion	153
5.3.8 Influence of substrate thickness on the contact angle	155
5.3.9 Inside the Carbon Nanotube.....	155
5.4 Simulation of the wetting of molten NaNO ₃ -KNO ₃ mixtures with and without α- SiO ₂ on MgO.....	158
Chapter 6 Conclusions and Future Plans.....	162
6.1 Conclusions.....	162
6.2 Future Plans.....	168
References.....	169
Appendix A: Code for Simulations.....	1
A.1 LAMMPS Simulations code	1
A.1.1 Crystal cell data for NaNO ₃	1
A.1.2 Obtain equilibrated molten structure from crystal cell, example for NaNO ₃ at 593K	2

A.1.3 Density Calculation.....	5
A.1.4 Radial Distribution	5
A.1.5 Thermal conductivity calculation:.....	6
A.1.6 Viscosity calculation:	7
A.1.7 Specific heat capacity calculation:.....	8
A.1.8 Obtain Amorphous Silica Bulk from randomly generated topology and check RDF	9
A.2 MATLAB Contact angle calculation program	12
Appendix B: Sample Preparation and Equipment	21

LIST OF FIGURES

Figure 1.1 Trends and forecasts of global energy consumption. (Adapted from Zou et al. ²).....	1
Figure 1.2 Overview of a CSP plant	4
Figure 2.1 Nanoparticle agglomeration and subsequent sedimentation.....	15
Figure 2.2 Different corrosion mechanisms of molten salts on metallic alloys.(Adapted from Walczak et al. ³³)	19
Figure 2.3 Contact angle of the liquid studies on the two almost identical metal glass alloy surfaces. Bottom: Roughness of the two surfaces. The most wetting surface (LM1) shows the highest corrosion ⁵⁵	22
Figure 2.4 Nanoscale formulation of process of molten salt composite materials, with ceramic matrix (left) and graphite (right). ⁵⁶	24

Figure 2.5 Images of molten salt composites without (a) and with (b) ceramic material. The leakage in the presence of a graphite matrix versus only MgO is evident ⁵⁶	26
Figure 2.6 Schematic illustrates of microstructure development of CPCMs for (a) NaLiCO ₃ based and (b) Na ₂ CO ₃ based composites ⁶²	27
Figure 2.7 Effect of sintering temperature on the initial CA of molten NaLiCO ₃ on MgO (Adapted from ⁷⁰).....	31
Figure 2.8 Molecular simulation of contact angle. Spherical (left) and cylindrical (right) geometries are the most commonly used.....	33
Figure 2.9 Effect of droplet size on droplet shape. Modelled by first-principle dynamics based on Young's equation ⁸³	35
Figure 2.10 Effect of droplet size on the calculated contact angle. Equilibrated trajectories of droplets with different sizes from molecular dynamic simulations (adapted from ⁷⁹).....	36
Figure 2.11 Simulation trajectory snapshots denoting the existence of clustered ions and vacuum cavities at the vapor molten salt interface. (Adapted from ¹⁰⁵)	41
Figure 2.12 Sodium sulfate melting on the spherical nanoscale calcium oxide substrate at different temperatures ¹¹¹	44
Figure 2.13 2-D mass density profiles of sessile nanofluid nanodroplets with different solid liquid interactions. Top left being the most lyophilic and bottom right the most lyophobic ¹¹²	46
Figure 2.14 a) Diagrammatic drawing of the initial configuration of the simulation system: a cylinder nanofluid droplet laden with well-dispersed nanoparticles is placed on the solid substrate. ϕ denotes the nanoparticle volume fraction. b) MD snapshot of the nanofluid ¹¹³	47
Figure 3.1 Preparation process for the formulation of molten salt nanofluids.....	53

Figure 3.2 The ADE Phase Shift MicroXAM Interferometer used for roughness measurements	55
Figure 3.3 The KRUSS HT Contact Angle apparatus	56
Figure 3.4 The Anton Paar MRC 502	57
Figure 4.1 CA measurements of SS (Solar Salt) with 0 wt.%, 0.5 wt.%, 1.0 wt.%, 1.5 wt.% and 2.5 wt.% of SiO ₂ on an Al ₂ O ₃ substrate.	80
Figure 4.2 CA snapshots of solar salt with 0 wt.%, 1.0 wt.% and 2.5 wt.% of SiO ₂ on an Al ₂ O ₃ substrate at 250 °C, 310 °C and 350 °C.	81
Figure 4.3 CA measurements of NaNO ₃ and KNO ₃ with 0 wt.% and 1.0 wt.% of SiO ₂ on an Al ₂ O ₃ substrate.	82
Figure 4.4 Dynamic viscosity data at 100 s ⁻¹ for sodium nitrate (A), potassium nitrate (B), Solar Salt (C) and their nanofluids compositions. Viscosity vs contact angle data for Solar Salt and Solar Salt nanofluid (D).....	83
Figure 4.5 The phase diagram for the NaNO ₃ -KNO ₃ system ¹³¹ showing solar salt composition (36%mol KNO ₃).....	85
Figure 4.6 Heat flow versus temperature for a) Solar Salt 0 and 5.0% w.t SiO ₂ , b) NaNO ₃ 0 and 5.0% w.t SiO ₂ , c) KNO ₃ 0 and 5.0% w.t SiO ₂	87
Figure 4.7 XRD data of Solar salt with 5.0% α-SiO ₂ NPs after melting at 390 °C for 24h. (Hu et al. ¹³⁵)	89
Figure 4.8 NaNO ₃ (top) and KNO ₃ (bottom) with 5.0 wt.% α-SiO ₂ NPs.....	91
Figure 4.9 a) Density of Solar Salt + 1.0% wt. SiO ₂ pellets compressed at different rates b) CA of Solar Salt and Solar Salt + 1.0% w.t SiO ₂ with pellets compressed at 20 and 120MPa.....	92
Figure 4.10 Contact Angle of solar salt on Alumina and Fused Quartz	93
Figure 4.11 Contact Angle of Solar Salt. Dependence on surface type.	95

Figure 4.12 Photographs of SS347 corrosion results left column: a) carbonate salts and b) SS347 samples after 600h corrosion test at 600 °C and SS310 right column: a) carbonate salts and b) SS310 samples after 600h corrosion test at 600 °C.....	97
Figure 4.13 Contact angle of carbonate salt on SS310 and SS347 at 410oC a) just after melting and b) evolving with time	98
Figure 4.14 Schematic representation of corrosion process for a) SS310 and b) graphitized SS310 in molten carbonate salt	99
Figure 4.15 Schematic representation of corrosion process for a) SS347 and b) graphitized SS347 in molten carbonate salt	100
Figure 4.16 CA of (left to right) LiNO ₃ , NaNO ₃ and KNO ₃ at 340 °C	103
Figure 4.17 CA of molten NaNO ₃ - KNO ₃ . Dependence on molar ratios	105
Figure 4.18 Contact Angle versus Temperature of Solar Salt doped with Nanospheres (10-15nm), Flakes (150µm) and Microspheres (500µm)	107
Figure 4.19 Viscosity vs Temperature of Solar Salt doped with 0.5 wt.% of 3 different type of graphite particles. (Adapted from Palacios et al. ²⁸)	108
Figure 4.20 Solar Salt + graphite pellet before (left) and after (right) melting and quenching. Bottom row displays movement of nanoparticles in boiling water nanofluid ¹³⁹	110
Figure 5.1 Equilibration process for the formulation of molten NaNO ₃	115
Figure 5.2. Radial Distribution function of NaNO ₃ and KNO ₃ , comparison between Buckingham, Lennard-Jones potentials and XRD experimental data from Adya et al. ⁹⁷	119
Figure 5.3. Density of Solar Salt (60% NaNO ₃ -40% KNO ₃), comparison with experimental data ¹²⁸	121

Figure 5.4. Thermal Conductivity of Solar Salt (60% NaNO ₃ -40% KNO ₃), comparison with experimental data ¹⁵²⁻¹⁵⁷	122
Figure 5.5. Viscosity of Solar Salt (60% NaNO ₃ -40% KNO ₃), comparison with experimental data ¹⁵⁸	123
Figure 5.6. Surface Tension of Solar Salt (60% NaNO ₃ -40% KNO ₃), comparison with experimental data ¹⁵¹	123
Figure 5.7. Diffusion Coefficient of Solar Salt (60% NaNO ₃ -40% KNO ₃), comparison with experimental data ¹⁵⁰	124
Figure 5.8 Fitting of energy curves between Morse and Lennard-Jones potentials.	125
Figure 5.9 Radial Distribution function of amorphous SiO ₂ , comparison between Morse (red) and Lennard-Jones (blue) potentials.	128
Figure 5.10 Si-O bond length distribution in amorphous SiO ₂ , comparison between Morse (red) and Lennard-Jones (blue) potentials.	129
Figure 5.11 Si-O and O-Si coordination number distributions in amorphous SiO ₂ , comparison between Morse (blue) and Lennard-Jones (orange) potentials.....	130
Figure 5.12 O-Si-O and Si-O-Si angular distribution in amorphous SiO ₂ , comparison between Morse (blue) and Lennard-Jones (orange) potentials.	130
Figure 5.13 Molten solar salt (right) placed on top of an amorphous SiO ₂ block (left).	134
Figure 5.14 Molten solar salt (right) placed on top of an amorphous SiO ₂ block (left). Experimental density from Janz et al (1981) ¹⁵⁸	135
Figure 5.15 Self-diffusivity coefficients of molten salt calculated in each region. Units are in cm ² /s x 10 ⁻⁵	136

Figure 5.16 Left: Sodium and potassium interactions with silica (Si-Na, Si-K). Right: Sodium and potassium interactions with oxygen in silica (Osi-Na, Osi-K).....	137
Figure 5.17 Schematic description of the texture rough surface formed with square pillars. The left and image depict the top and side view of the surface respectively. W_p is the width and h_p the height of the pillar. S_p is the distance between pillars.....	142
Figure 5.18 Molten salt placed on the MgO substrate (top row) and on graphite (bottom row): screenshots at the beginning (left column) and at the end of the simulation (right column).	144
Figure 5.19 Effect of drop diameter on surface tension of molten NaNO_3 (right) and molten KNO_3 (left).	147
Figure 5.20 Contact angle of molten NaNO_3 on Graphite (left) and $\text{MgO} \{1\ 0\ 0\}$ (right).	149
Figure 5.21 Density, viscosity and surface tension of NaNO_3 (left column) and KNO_3 (right column), comparison with experimental data ¹⁵¹	151
Figure 5.22 Contact angle versus drop radius of curvature R for NaNO_3 on $\text{MgO} \{1\ 0\ 0\}$	152
Figure 5.23 Contact angle of NaNO_3 (left) and KNO_3 (right) on MgO and graphite. Comparison with experimental data.	154
Figure 5.24 Work of adhesion, comparison with experimental data	155
Figure 5.25 Evolution of contact angle with different substrate thickness.	155
Figure 5.26 Density of molten NaNO_3 inside the CNT, for different diameters.....	158
Figure 5.27 Contact Angle versus Temperature of Solar Salt and Solar Salt doped with silica Nanoparticles	159
Figure 5.28 Contact angle evolution with temperature of Solar Salt with (top) and without (bottom) silica NPs. Left column 520K, middle 575K and right 625K.	160

List of Tables

Table 3.1 Specifications of the graphite particles used in this work.	51
Table 3.3 Chemical composition of the stainless-steel surfaces used in the corrosion studies.....	54
Table 4.1 CA measurements of NaNO ₃ on MgO (1 1 0)	102
Table 4.2 CA measurements of LiNO ₃ on MgO (1 1 0)	103
Table 4.3 CA measurements of KNO ₃ on MgO (1 1 0).....	103
Table 4.4 Atomic properties of NaNO ₃ , LiNO ₃ and KNO ₃	104
Table 5.1. Lennard-Jones Parameters of NaNO ₃ and KNO ₃	113
Table 5.2. NaNO ₃ -KNO ₃ Simulated Systems	114
Table 5.3. Comparison between experimental measurements and calculated values for NaNO ₃ , KNO ₃ and their mixtures for various properties ^{128,149–152}	120
Table 5.4. Proposed Lennard-Jones Parameters for Amorphous SiO ₂	126
Table 5.5 Comparison of calculated density and thermal expansion coefficient of Amorphous SiO ₂ , with Lennard-Jones and Morse potential, with experimental data ¹⁶⁸	131
Table 5.6 Calculated Contact Angle values for NaNO ₃ and KNO ₃ in CNT of different diameters. The last column represents graphene.	157

LIST OF ABBREVIATIONS

Abbreviation	Definition
CSP	Concentrated solar power
TES	Thermal energy storage
MSNF	Molten salt nanofluid
NF	Nanofluid
NP	Nanoparticle
CA	Contact angle
SS	Solar salt
PCM	Phase change material
L-J	Lennard-Jones
RDF	Radial Distribution Function
ADF	Angular Distribution Function
MD	Molecular dynamics
XRD	X-ray diffraction
SEM	Scanning Electron Microscopy
DSC	Differential Scanning Calorimetry
NVE	Microcanonical ensemble
NVT	Canonical ensemble
NPT	Isobaric ensemble
NPH	Isenthalpic isobaric ensemble
PPPM	Particle-Particle Particle-Mesh

LIST OF PUBLICATIONS

A. Anagnostopoulos, A. Alexiadis, Y. Ding (2020). "Simplified Force Field for Molecular Dynamics Simulations of Amorphous SiO₂ for Solar Applications". International Journal of Thermal Sciences, (Re-Submitted, Under Review, 20/05/2020).

Y. Grosu, A. Anagnostopoulos, M. H. Navarro, Y. Ding, A. Faik (2020). "Inhibiting hot corrosion of molten Li₂CO₃-Na₂CO₃-K₂CO₃ salt through graphitization of construction materials for concentrated solar power". Solar Energy Materials and Solar Cells, **2020**, 215, 110650.

A. Anagnostopoulos, A. Alexiadis, Y. Ding. "Wettability of NaNO₃ and KNO₃ on MgO and Carbon Surfaces – Understanding the Substrate and the Length Scale Effects". The Journal of Physical Chemistry C, **2020**, 124 (15), 8140-8152.

A. Anagnostopoulos, A. Palacios, H. Navarro, Y. Ding. "Effect of SiO₂ nanoparticle addition on the wetting and rheological properties of solar salt". Solar Energy Materials and Solar Cells, **2020**, 210, 110483

A. Anagnostopoulos, A. Palacios, H. Navarro, S. Fereres, Y. Ding (2019). "Influence of measurement techniques on molten salt surface wetting characterization", ICNF 2019: 1st International Conference on Nanofluids/European Symposium on Nanofluids, 2019, 25-28 June, Castellon de La Plana, Spain (ISBN 978-84-685-3917-1).

A. Anagnostopoulos, U. Nithiyantham, H. Navarro, Y. Grosu, S. Fereres, A. Faik, Y. Ding (2019). "Effect of Preparation Method on the Wettability of Molten Salt Nanofluids", ICNF 2019: 1st International Conference on Nanofluids / European Symposium on Nanofluids, 2019, 25-28 Jun, Castellon de La Plana, Spain (ISBN 978-84-685-3917-1).

Anagnostopoulos A., Alexiadis, Y. Ding. "Molecular Dynamics Simulation of Solar Salt (NaNO₃-KNO₃) mixtures", Solar Energy Materials and Solar Cells, **2019**, 200, 109897.

A. Anagnostopoulos, A. Palacios, N. Navarrete, M. Navarro, L. Hernandez, Y. Ding (2018). "Effect of Temperature on the Internal Structure of Solar Salt-SiO₂", SOLARPACES 2018: International Conference on Concentrating Solar Power and Chemical Energy Systems, 2018, 1 - 5 October 2018, Casablanca, Morocco (AiP Conference Proceedings).

Chapter 1 INTRODUCTION

As the worldwide population increases so does worldwide energy consumption. It is speculated, that the required energy will increase, from 24 PWh/yr in 2020 to 30 in 2030 and 60 in 2050, with currently only 40% of the required energy being produced using renewable means and almost 45% of global energy generation coming from fossil fuel sources, which leads to the generation of greenhouse gases ^{1,2}. Utilization of renewable technologies is the safest and cleanest way to counter the growing environmental crisis. The largest source of renewable energy is the sun.

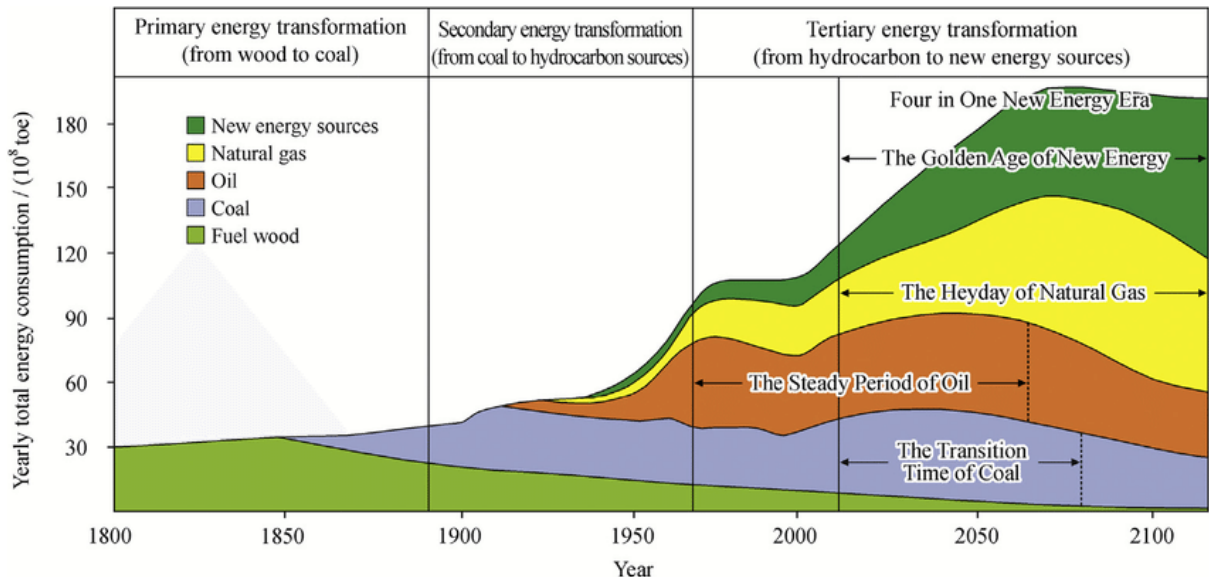


Figure 1.1 Trends and forecasts of global energy consumption. (Adapted from Zou et al.²)

Two major technologies have been adopted, one is Solar PV for shortwave region of solar radiation and the other is solar thermal for the long part of the spectra. Due to the intermittent nature of solar radiation and the unpredictable demands of energy from the grid thermal energy storage (TES) is mandatory to meet the fluctuating energy demand ³. Batteries suffer from storage capacity issues⁴ thus making solar thermal storage the best candidate for solar energy capture and storage at an industrial scale and for longer timeframes. In terms of TES there are low temperature applications, which make use of thermal heat (< 100 °C) using solar ponds and solar collectors and medium to high temperature thermal heat with the use of concentrators and solar towers ⁵. The latter ones are called concentrated solar power (CSP) plants and are the most common industrial developments involving solar energy.

TES is achieved using economical and effective thermal storage materials. These materials are classified based on the way that they store heat into chemical, sensible and latent heat and on their temperature range in low, medium, high and very high temperature materials ⁶.

This work is based on phase change materials (PCMs). In these there is a transition from solid to liquid state and hence the type of storage is called latent heat storage, as the critical factor for their performance is the heat, they release during phase change. The common point of all these materials is good energy density and an isothermal phase change process. They are categorized in organic and inorganic PCMs. Organic PCMs involves mostly types of paraffin and thermal oils as well as fatty acids. Inorganic ones involve the use of salts and alloys. Organic materials are used for applications

below 200 °C (low and medium temperature range), while inorganic ones are used in temperatures ranging from 200 to 1500 °C (high and very high temperature range). This work is focused on the latter category and particularly molten salts. Different PCMs have different characteristics and thus issues: inorganic metallic materials have a high thermal conductivity but on the other hand are expensive and suffer from corrosion issues; inorganic hydrates, despite demonstrating the best phase-change properties suffer from supercooling and phase segregation due to their ease of absorbing water; Furthermore, almost all organic PCMs are flammable and a large number of those release toxic substances; molten salts can be highly corrosive even for highly resistant alloys (i.e. Inconel) depending on their compositions ; organic PCMs, inorganic hydrates, and molten salts suffer from poor heat transfer characteristics.

A very promising category of inorganic PCMs for the CSP industry are salts. These salts when elevated to higher temperatures are called molten salts. The main distinct advantage of molten salts is their high temperature melting point and their large operating range. Most materials either melt at lower temperatures or are difficult to handle in higher temperatures due to high vapor pressure. Salts are preferred due to their very stable structure, their low cost, high specific heat capacity, high density, non-flammability and finally low vapor pressure ⁶. Low pressure is an important property, as it does not require the construction of expensive pressurized storage tanks for proper operational conditions. Molten salts can be used in CSP plants both as heat transfer fluids and as energy storage materials. As energy storage materials they can be used both in Sensible and Latent heat energy storage.



Figure 1.2 Overview of a CSP plant

Sensible heat storage works by altering the temperature of the storage medium. The storage capacity mainly depends on the density and specific heat capacity of the material as well as its stability in a wide temperature range. It is the most commonly applied in industrial scale applications.⁶

Latent heat storage is the second largest in terms of storage density. It presents an energy density at least 5 times higher than sensible heat storage⁷. In this method the heat is stored via means of phase change (e.g. solid-liquid, gas-liquid). The material absorbs the solar energy in the form of heat and melts (phase changes). During phase change large amounts of heat are absorbed at a constant temperature point. This is highly advantageous as the temperature is maintained and thus heat losses are reduced. The heat is then released when necessary, which leads to re-solidification of the material. Due to their energy efficient behavior and stable temperature, energy accumulation and extraction can be conducted in a constant manner. This type of

storage can be applied in a wide-temperature range using materials with different melting points and is mostly focused on medium to high temperature storage. As in sensible heat storage a determining factor for the good performance of the material is its specific heat capacity.

The biggest drawback of molten salts are their poor thermal properties. Research on potential methods to enhance their thermal properties is ongoing. In the last decades several have been established. These include among others, the addition of metallic fins ⁸, the use of integral heat pipes ⁹, the use of special type of foams ¹⁰, the dispersion of highly thermally conductive materials ¹¹, and the encapsulation of PCMs ¹². Most of these techniques though are unsuitable for molten salts. Salts are highly corrosive especially in molten states and therefore the addition of foams and fins and pipes is impossible due to their long-term degradation. Dispersion or encapsulation of highly thermally conductive nanoparticles (NPs) usually in the form of silica and graphite is possible, but currently several issues remained unsolved. The most important issues of molten salt nanofluids (MSNFs) and encapsulated PCMs are the long-term instability due to particle sedimentation, the pressure drop and required high required pumping power due to the suspension of solid particles in the liquid, the added corrosion and their scalability ¹³.

Among the various issues the most critical issues MSNFs is their long-term instability. Due to their high surface energy NPs tend to agglomerate and form larger microstructures that lead to particle sedimentations. Keeping the NPs dispersed in a fluid for a long time (i.e. months) is a difficult challenge. In the case of room temperature

liquids several techniques to prevent agglomeration exist. The most common one is the addition of surfactants ¹⁴. However, most surfactants are organic based materials and cannot be used in high temperature scenarios. The available ones have a very high cost and are still limited to temperatures below 200 °C. Another common method is ultrasonic vibration. This technique, however, is difficult to scale up to an industrial scale. Research on agglomeration prevention is also focused on the control of pH ¹⁵, though current theories correlating the electrostatic stabilization of molten salts to their long-term stability are still at an early stage.

Furthermore, due to their anomalous structural changes, results of the reported thermal property enhancement and particularly specific heat capacity is still controversial. The mechanisms which govern the interaction between the NPs and the molten salt are still not fully understood ¹³. Some authors report increases, while others report a decrease in the thermal properties ¹¹. Furthermore, the molten salt nanofluids (MSNFs) typically display shear-thinning behavior, unlike the molten salts which are purely Newtonian, but in cases Newtonian behavior has also been reported¹⁶. Additionally, no study on the contact angle and surface tension of molten salt nanofluids has been to this date conducted, which could potentially lead to more insight into their behavior. CA and surface tension can provide insight to the performance of the MSNFs in terms of heat transfer, corrosion, and pumping power.

The second biggest drawback of molten salts is their corrosivity. All the structural materials of a CSP plant are constantly exposed to severe operating conditions. These involve very high operation temperatures as well as steep temperature gradients,

which lead to alternating mechanical stress, due to rapid expansion-contraction cycles. During the peak of any day a steady high irradiation leads to a constant thermal stress. While, during dusk night times rapid temperature drops lead to transitions from very high to low temperatures. This also secondarily occurs during energy production cycles. These high energy environments accompanied with rapid changes in liquid-flow synergistically affect the corrosion levels in CSP plants.

In terms of corrosion, despite their so far smooth operation, CSP plants have room for improvement. The materials of choice are employed up to now. Future materials require extended verification to correctly account for any substantial change in design and operating conditions. Corrosion of materials exposed to molten salts is associated with high maintenance costs and can some time even lead to plant failure. Identifying a method to prevent corrosion in CSP plants is crucial, especially for next generation CSP plants that aim to use chloride salts, that have shown corrosion rates of millimeters even in resistant alloys¹⁷.

A new promising method for the prevention of corrosion is spray-graphitization. This has been shown to prevent/reduce corrosion in nitrate salts¹⁸. However, studies on carbonate salts have not yet been conducted.

Wettability has been shown to be related to corrosion. For this reason, in this work the wettability of molten salts on graphitized surfaces is also examined and a link with the corrosion of the sprayed alloy surface is deduced, in order to provide a better

understanding on the corrosion behavior between molten carbonate salts and structural materials used in CSP plants.

For TES, aside from molten salts an alternative promising technology with the required benchmark thermal properties and a stable structure are composite phase change materials. Ceramic grains are mixed with the salt powder and then sintered to produce the final composite. The resulting materials have been shown to have a stable structure and a larger energy storage density compared to the base salt. Furthermore, addition of a certain volume of ceramic grains leads to a stable non-leaking structure, even in the presence of NPs, countering to an extent the incompatibility issue between NPs and molten salts. Furthermore, the presence of the ceramic material results in an improvement in thermal properties ¹⁹. Good wettability behavior between molten salts and ceramic materials has been identified to be an important factor for the final structure of these sintered mixtures. However, there is still a lack of data regarding the wetting behavior of molten salts with respect to the ceramics used in composite material formulation.

In summary, molten salts are used both as heat transfer fluids and energy storage materials. As energy storage materials they are also used in the form of composites. Wetting behavior of MSNFs remains to this date unexplored. In terms of composite TES materials, the wettability is suggested to have an effect on the final structure of the sintered material. In terms of corrosion it has been linked to corrosion rates. To this end the objective of this work is the study on the wetting behavior of molten salts and MSNFs on ceramic and metallic surfaces.

To study the wettability the contact angle (CA) is measured for both molten salts and MSNFs. The effect of temperature, surface type, surface roughness, molar composition, atmosphere, NP geometry and concentration are all investigated.

Furthermore, to improve the understanding of the wetting behavior of molten salts, molecular dynamics simulations are also conducted. To this end novel force field parameters for molten NaNO_3 , KNO_3 and amorphous SiO_2 are generated capable of accurately simulations cross-term interactions in the salt-ceramic interfaces. These are then used in combined simulations to study the wetting behavior of molten salts on ceramic and carbon surfaces in the atomic level.

Based on the above the thesis structure is as follows

- Chapter 1 Literature Review: focused on the stability of MSNFS, the interplay of wettability in corrosion, wettability measurements of molten salt and modelling techniques for contact angle of liquids and liquid-nanoparticle systems.
- Chapter 2 Materials and Methods: The experimental and computational methods practiced in this work are presented and outlined.
- Chapter 3 Experimental Results: Contact angle studies on various salts and with various conditions are presented.
- Chapter 4 Molecular Dynamics: Computational studies on the wettability of molten salt nanofluids are presented.
- Chapter 5 Conclusions and Future work: A summary of the work done and suggestions of future research.

Chapter 2 LITERATURE REVIEW

2.1 Molten salt nanofluids: Controversies

2.1.1 Controversies in property measurements

Solar power is a highly important technology, due to the sun being the most readily available renewable energy source. The most common industrial applications of solar power are CSP plants. Molten salts are the most frequently used materials primarily as energy storage solutions and secondarily as heat transfer fluids. The most commonly used molten salt is the so called Solar Salt (SS), which is a mixture of 60% NaNO_3 and 40% KNO_3 . Their main advantages are their large temperature operating range and thermal stability. Secondarily they have a low cost, are non-flammable, readily available and with a low vapor pressure. Their most important drawback is their poor thermal properties. For this reason, metal oxide NPs are suspended in the molten salt ²⁰. The first discovery of such functionality of NPs in molten salts was by Shin and Banerjee. In their work they used 62%-38% Li_2CO_3 - K_2CO_3 with 1.0 wt.% silica NPs. They measured the specific heat capacity and identified an increase of more than 100% compared to the base value. Further to their initial observations the researchers standardized the formulation process of MSNFs. This remarkable enhancement of the

specific heat capacity led to the creation of a large network of investigators who have been subsequently studying MSNFs in aspects ranging from industrial cost of application to identification of the principal mechanism behind the observed enhancement. However, despite this initially observed enhancement, results from subsequent studies were controversial.

In terms of heat capacity Cabedo et al.²¹ measured an increase of 31.1% at 0.5% wt. of NPs, but most studies measured a maximal specific heat capacity at 1% NPs using the same type of particles and a several degrees lower (Chieruzzi et al.¹¹). Furthermore, in another study Milozzi , observed no variation of the specific heat capacity with the addition of 1% or 3% NPs²², while another work by Jung and co-workers saw a further increase of 13% from 1% to 2% NPs, using the same type of particles ²³. The effect of the type and the geometry of the NP on the resulting specific heat capacity is also not clear. A Study by Jo B et al.²³, identified that an increase in the mean NP diameter lead to higher measured values for the specific heat capacity. Contrary to those findings Riazi et al.²⁴, observed maximum highest specific heat capacity in the case of the smallest NP diameter and presented completely opposite trends, showing a decrease in the specific heat capacity as the diameter of the NPs was increased.

Thermal conductivity measurements produced similar results. The study of Shin et al.²⁵ found a 36% increase in the thermal conductivity with the addition of silica NPs in a Li₂CO₃-K₂CO₃ eutectic. In another study on the same salts no significant increase in the thermal conductivity with the addition of 1% Al₂O₃ NPs was observed²⁶.

Finally, in the case of the viscosity in one study a maximum increase of 130% in the viscosity of the base salt at the presence of 5% carbon nanotubes is observed²⁷. In another study by Palacios et al the viscosity of SS was measured with and without carbon particles. When doped with nano sized graphite particles an increase of 900% was observed²⁸. But Lasfargues et al²⁹, observed the opposite effect. They attributed their observations to the fact that high shear rates involved in rheological measurements can cause the NP clusters to break and the smaller clusters to dissolve in the liquid. This leads to a homogenization of the liquid and thus a more Newtonian behavior, which explains the viscosity values to be almost the same as the base fluid.

In all of these studies authors have concluded that the observed differences in heat transfer and rheological properties on the base fluid (molten salt) are due to alterations in the structure of the base material by the addition of the NPs. However, the observed alternations vary from study to study. This is attributed to the different, type, geometry and origin of the materials used in each scenario. What is certain in all cases is that in the nanoscale molecular interactions at the NP salt ion interface are responsible for the change in thermophysical properties²⁶.

2.1.2 Nanoparticle Agglomeration Prevention

Due to their high surface energy NPs tend to agglomerate. When operated as nanofluids the material is always in liquid state. Consequentially, due to Brownian movements the NPs can potentially collide. If the collision energy is high enough then that will lead to an adhesive behavior leading to the formation of nanoclusters. These clusters have higher probability of colliding with smaller surrounding particles. The

result is agglomerated structures that typically reach micrometer range sizes. This increase in their volume and thus weight leads to sedimentation and thus high heterogeneity, which has been shown to diminish any heat transfer enhancements. Conclusively, the most important challenge in nanofluids today is to maintain their high surface to volume ratio for long times (i.e. months). The agglomeration rate of nanometer sized particles is typically modelled (in non-dynamic conditions) by the Stokes law, which takes into account the liquid-particle density difference the viscosity of the medium and the diameter of the particles. Therefore, salt NP combinations are based on these parameters³⁰. The most common agglomeration prevention strategies are:

- Surfactant addition, which have shown to completely prevent particle agglomeration, but also limiting heat transfer enhancement. These additives, however, are mostly organic based or very expensive at high temperatures thus limiting their application at an industrial scale.
- Surface modification. This technique involves the addition of functionalized chemical groups on the surface of the particle through chemical reactions. Research in this area is wide-spread in biological applications, but due to its early stage and high cost is not yet encouraged for industrial applications of MSNFs²⁶.
- pH Control, involving the stabilization of the electro-kinetic properties of the fluid. The principal theory behind these concepts does not apply to high ionic concentrated liquids such as molten salts.
- Ultrasonication, which involves the de-agglomeration of the MSNFs through soundwaves. This is the principal method used for the laboratory level preparation of MSNFs but is difficult to scale up to an industrial level.

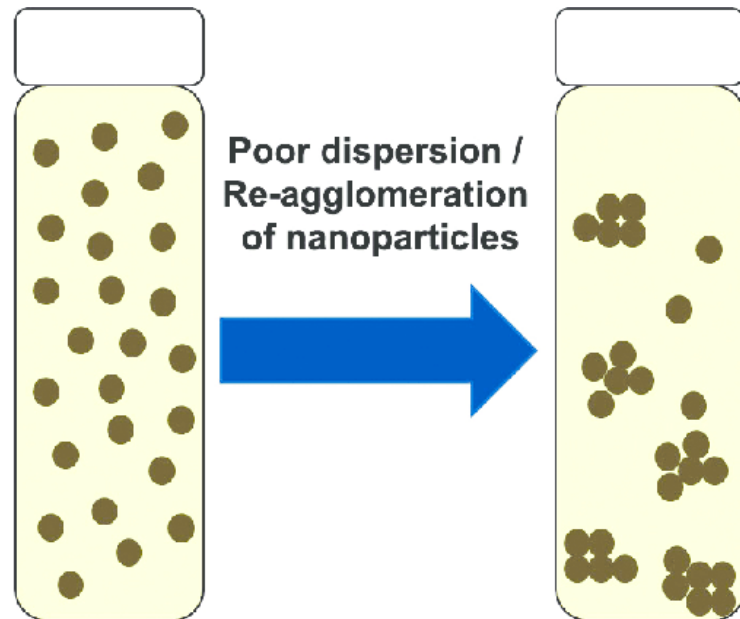


Figure 2.1 Nanoparticle agglomeration and subsequent sedimentation.

2.1.3 Stability Studies

Stability assessment of colloid suspensions is typically conducted through dynamic laser scattering (DLS) measurements. Due to the high operating temperatures of molten salts, DLS measurements are difficult to conduct. Therefore, all studies conducted on the stability of MSNFs work indirectly, by measuring the variation of a property with time, typically the specific heat capacity, being the most critical in terms of performance.

Mondragon et al., investigated the behavior of Solar salt with 0.5 wt.% α -SiO₂ NPs. The MSNF was kept at 500 °C for 12h. The sample was then split in 3 parts and the specific heat capacity was measured for each. The lowest specific heat capacity was

measured at the top part of the container and highest at the bottom¹³. However, even the top part showed a slight enhancement that was within the error of the DSC.

In a study by Andreu-Cabedo et al, SS with 1 wt. % α -SiO₂ was cycled thermally 8 times between 160 and 420 °C. The specific heat capacity of the MSNF was measured each time in the liquid state between 250 and 420 °C. A stable minor enhancement was observed higher than the error of the DSC²¹.

Schuller et al. attained opposite results¹³. They too cycled thermally SS with 1 wt. % α -SiO₂ between 300 and 450 °C for 6h. They observed a gradual decrease in the specific heat capacity with each cycle, with no enhancement observed at the last cycle. They identified that this instability was observed after the sample temperature exceeded 400 °C. An identical study was carried out with alumina NPs. In the latter a stable specific heat capacity was observed throughout the whole temperature range¹³. The study involving the alumina NPs was conducted for a second time with a larger sample size (several grams) and 448 cycles instead of 3. The specific heat capacity was analyzed for samples extracted from the top, middle and bottom of the container. No difference was observed between the 3 sample areas.

A similar study involving a mixture of carbonate salts was conducted by the same authors. In that one 62% - 38% molar ratio Li₂CO₃ – K₂CO₃ was mixed with 1 wt.% alumina NPs. An identical cycling process to the nitrate salts was applied. However, in this case the specific heat capacity of the MSNF was found to decrease. However, the obtained specific heat was still higher than the base value. The researchers identified

high concentrations of NPs on the bottom and wall of the container. A sensitivity study on the effect of NP concentration revealed no further enhancement.

Lasfargues et al studied the stability of SS with 0.1 wt% CuO NPs. They proposed three methods for agglomeration prevention: mechanical stirring, bubbling and forced circulation. The MSNF was kept at 300 C for 800 h. In the base case a reduction in the specific heat capacity was observed at 200h. Out of the three suggested methodologies only mechanical stirring demonstrated a stable value for the specific heat capacity throughout the duration of the experiment. In the other cases a decrease was observed, that led to values identical to the base case or in the case of forced circulation even below that.

The stability test of the SS doped with Al₂O₃ NPs was performed at a larger scale involving kilos of materials and for large number of cycles (up to 448 cycles). At fixed samples intervals the sample was extracted from lower, middle and upper part of the testing tank. The specific heat of the MSNF was found to remain stable through multiple cycles. Furthermore, the value was almost identical for all 3 parts of the testing tank. It was thus deduced that in this particular mixture sedimentation did not occur.

In another study from Somani the effect of turbidity on the stability of NaNO₃ with different type of NPs was investigated. In all cases a higher temperature was correlated with a higher agglomeration rate, which was attributed to the higher collision rates of particles due to their increased kinetic energy. Studies with identical NP types and concentrations on NaCl-KCl mixtures showed that the viscosity of the medium plays a

far more important role than initial NP size. In the case of the chlorides the viscosity is significantly lower and thus the settling rate higher. Finally, raising the temperature of the molten NaNO_3 leads to a lower density and viscosity as well as higher particle sedimentation rates.

Conclusively, the stability of MSNFs is ambiguous and depends on several factors. However, all studies conclude that in the first couple of hours the MSNF appears to be stable. This is roughly the time duration of a CA measurement.

2.2 The Effect of wettability on corrosion

Corrosion caused by salts is a critical issue in the CSP industry. It depends on several factors most principally the chemical composition of the material, the chemistry of the liquid that induces the corrosion and the surface properties of the material. Chemical reactions in the surface of the material lead to its degradation. Compatibility between the molten salt and the materials used in CSP plants are mandatory for the prevention of this issue³¹. Previous research has linked the compatibility between the operating molten salt and the construction materials in CSP plants that come in contact with it. A better compatibility between the two has shown to decrease the total cost of electricity production³² and secondarily increase the safety of the standards of the plant.

Corrosion can vary in forms. It is defined as any form of degradation of the stainless steel/metallic alloy surface through thermodynamic reactions. In CSP plants the highest degree of corrosion is observed in the molten salt storage tanks, where the salt is maintained for long duration (thousands of hours). Practically all types of corrosion

have the same principle, but each different type can lead to different type of defects and reaction kinetics, which can then lead to different corrosion rates.

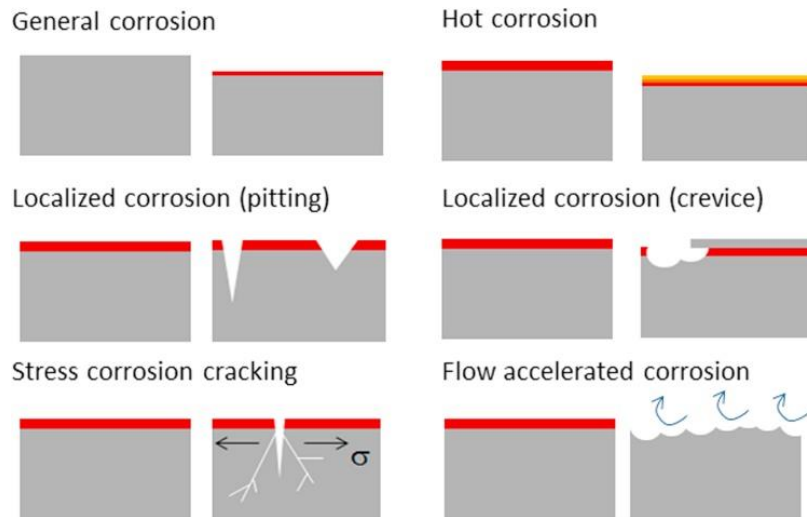


Figure 2.2 Different corrosion mechanisms of molten salts on metallic alloys.(Adapted from Walczak et al. ³³)

Due to the SS being the most commonly used material in CSP plants most corrosion studies focus on the interaction of metals and metal alloys with nitrate salts. Studies conducted by Fernandez et al, involved the comparison of HitecXL and Solar Salt. They found that the first showed significantly less corrosion on two different types of stainless steel as well as an alloy. Thus, the effect of the composition of the material on the corrosion rate was established also for the case of molten salts. Several more works have been conducted on stainless steel involving HITEC³⁴, tenary³⁵ and KNO₃-NaNO₂-NaNO₃ quaternary³⁶ nitrate salts and various others with SS^{37,38}. Recently a potential solution to the corrosion was provided by Cabanas et al, who studied the effect of molten nitrate triple eutectic salts in normal and nitrogen atmosphere on carbon steel (A516 Gr70). Although they initially observed corrosive behavior of the salt on the surface, they noted that the corrosion rate was slowly passivated with time.

They attribute this to the formation of oxide layers on the steel surface that passivated the corrosion. They suggest that the corrosion kinetics could potentially be minimized through this process, after long exposure times³⁹. Despite ongoing research molten nitrate salts concern operating CSP plants. Next generation CSP plants are aimed to work at even higher temperatures; thus the molten nitrate salts are to be replaced with molten carbonates and chlorides.

This is unfortunate as chloride salts are those with the lowest cost/ton and thus the most attractive option, but the added cost related with the corrosion damage they cause is a problematic issue. In a work by Dorchen et al, the authors compared the corrosion effect of SS containing various levels of chloride impurities⁴⁰. In the same work an analysis of the reaction kinetics involved in the corrosion of stainless steels by molten salts showed that chlorides have a determining effect on corrosion. A review of the corrosion mechanisms of chloride salts on steel and alloy surfaces has been recently conducted by Ding et al.⁴¹. They arrive to conclusions similar to those of nitrate salts. The atmosphere and impurities of the salt have a significant effect on corrosion rates. They, also, report that operating a plant in an inert gas atmosphere can inhibit corrosion. Additionally, proper purification of the salt (e.g. through stepwise heating) can lead to a significant reduction in the observed corrosion rates. Additionally, they find that even nickel-based alloys such as the Hastelloy 625 that prove to be corrosion resistant to nitrate and carbonate salts do not display the same behavior when in contact with molten chlorides. Finally, they suggest an expensive, high precision set of electrochemical techniques that can be used to monitor corrosion rates.

Carbonate salts are the 2nd option for use in high temperature next generation CSP plants (i.e. >560 °C, temperatures where nitrate salts decompose). Their drawback is their higher cost compared to chlorides, but in terms of corrosion they display a more favorable behavior. Nevertheless, corrosion has been reported in several studies. In a work by Fernandez et al the corrosion effect of molten ternary carbonate mixture on several Al containing alloys was reported⁴². Similar results were obtained also in the cases of austenitic steel⁴³. Corrosive behavior of $\text{Li}_2\text{CO}_3\text{-K}_2\text{CO}_3$ on iron-chromium alloys are reported by Takeuchi et al.⁴⁴. Frangini et made similar observations for 310 and 316L stainless steels⁴⁵. A review outlining the mechanisms of corrosion of carbonate salts is provided by Liu et al and leads to similar observations in all 3 categories of salts⁴⁶.

Recent research has identified several methods to inhibit or prevent the corrosion caused by molten salts. Notable prevention methods involve the use of Al-slurry coating⁴⁷ and $\text{ZrO}_2\text{-Y}_2\text{O}_3$ ⁴⁸ coating for solar salt and Ni20Cr⁴⁹ and MCrAlX⁵⁰ coatings for molten chlorides. Another pathway involves the addition of Mg in chloride salts⁵¹, which led to a reduction in corrosion rates. Similar reports were made by Frangini and Loreti in the case of $\text{Li}_2\text{CO}_3\text{-Na}_2\text{CO}_3$ through addition of Mg and/or Ca at concentrations of 1.5 wt.%⁵². Another pathway to prevent corrosion is through spray-graphitization. Grosu et al has shown that his method can lead to complete corrosion prevention on carbon steel A516.Gr70 by HitecXL¹⁸. In a subsequent study by Piquot et al, the authors demonstrated corrosion prevention of HitecXL doped with SiO_2 nanoparticles on A516.Gr70⁵³. Finally, Gonzalez et al demonstrated that spraying a carbon steel surface with graphite can lead to corrosion prevention by Solar Salt⁵⁴.

However, aside from the chemical aspect of corrosion, studies on Zr-based alloys have shown a correlation between the wettability of the liquid and the corrosion rate of the material. Wang et al in their work measured the contact angle of a fluid with a pH of 7.4 on two different metallic glass alloys⁵⁵. Furthermore, they examined the surface roughness before and after the corrosion tests as well as the X-Ray Diffraction (XRD) patterns and the X-Ray Photoelectron Spectroscopy (XPS) spectra of the material. The only difference between the two alloys was a slight change (>5%) in the ratios of the elements present in each alloy. They identified a strong correlation between the alloy with the smallest surface energy and thus the smallest CA presented a higher corrosion than the other.

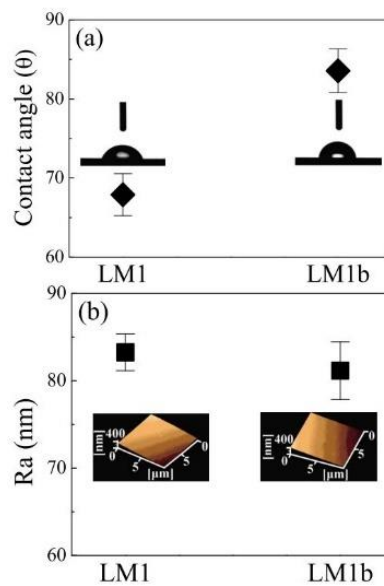


Figure 2.3 Contact angle of the liquid studies on the two almost identical metal glass alloy surfaces. Bottom: Roughness of the two surfaces. The most wetting surface (LM1) shows the highest corrosion⁵⁵.

As discussed above the current solution for prevention of corrosion in molten salts is graphitization. Graphite has known non-wetting properties. For this reason, a study is also presented on the graphitization of SS310 and SS347. The corrosion inhibition on $\text{Li}_2\text{CO}_3\text{-Na}_2\text{CO}_3\text{-K}_2\text{CO}_3$ is examined not only through chemical methods but also through a wettability study, to identify the effect of the wettability of the molten salt on the corrosion of SS310 and SS347.

2.3 The Effect of wettability on composite materials performance

Latent heat-based TES using PCMs is a popular method for intermittent renewable energy storage in the form of thermal energy. The low cost associated with the use of these materials as well as the reasonable energy density has led to an extended use of these materials, particularly molten salts. Nevertheless, as discussed, molten salts present issues mostly due to their corrosive nature, poor thermal properties, and sub-cooling. To counter these issues a novel technology has attracted attention, in the last decade, that of composite phase change materials (CPCMs). In these materials the molten salt, that plays the role of the PCM used for energy storage, is sintered with ceramic particles (typically MgO). This leads to a denser energy structure with improved stability and thermal properties. This can be better visualized in Figure 2.4. Firstly, the ceramic powder with the salt powder are mixed. In this stage voids are formed between the grains of the two materials. Uniaxial compression leads to a reduction of this void as the material is compressed and to a subsequent increase in the density. As the sintering process evolves the salt temperature increases, which leads to a phase transition. The liquid salt, pulls the grains of the ceramic material together with capillary forces, rearranging it and leading to the final composite structure.

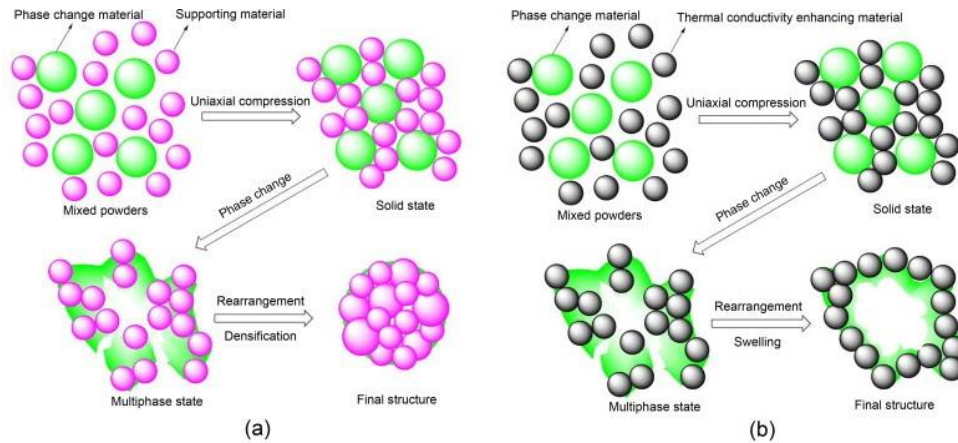


Figure 2.4 Nanoscale formulation of process of molten salt composite materials, with ceramic matrix (left) and graphite (right).⁵⁶

Originally, these composites involved the use of expanded graphite ⁵⁷. Expanded graphite is a form of graphite produced by the exfoliation of graphite disks. Heating of the exfoliated graphite leads to a de-vaporization of each structure with subsequent volume expansion. This forms a material with high surface to volume ratio and good thermal properties ⁵⁸. Similarly, to the process illustrated above originally paraffin⁵⁹ and later molten salt were used to generate composites.

In an attempt to further improve the performance of the stable ceramic-molten salt composites graphite flakes or carbon nanotubes were suspended in the mixture as a thermal enhancer ⁵⁶. These enriched composites, though, above certain concentrations presented leakage issues.

To comprehend the effect of wettability on the structural stability of the CPCMs containing graphite the importance of the wettability in the sintering process must be better outlined. In Figure 2.4 the composite structures without (left) and with (right) graphite particles are shown. As explained above, during the sintering process the

PCM transitions from liquid to solid phase, in the case of the molten salts to a viscous liquid (>5 mPa.s). The movement of the salt is thus governed by solid, liquid and vapor surface tensions and expressed through the Young-Laplace equation of the magnitude of pressure difference necessary for pore imbibition. This equation is in the form of $\Delta P = \frac{2\gamma}{r}$, where γ is in this case the interaction energy between the molten salt and the ceramic surface and r the radius of the pore.

This interaction energy of the liquid salt with the ceramic/carbon material is directly linked to its liquid-solid surface tension, which can be indirectly described by the CA of the molten salt on a solid substrate. Wettability measurements are known to represent the direction of the pressure gradient. Since, in this case the ceramic supporting material has a high interfacial energy, the CA is hypothesized to be small, thus leading to good imbibition in the pores of the solid and good spreading inside the cavities of the ceramic material. Due to the high surface tension of molten salts the capillary forces between the ceramic grains are high. That's why the ceramic grains are pulled together and arrange in energetically favorable positions. In fact, this process has been seen to improve even further the density of the composite material, after progressive heating and cooling cycles. These cycles lead to coarsening of the ceramic matrix and subsequent stronger rearrangement and densification, thus improving its rigidity. Composite structure with good wetting conditions between molten salt and ceramic material have thus been found to lead to minimum leakage even at high salt loadings.

Next consider a composite consisting of salt and graphite (Figure 2.4. (right)). The fabrication process is similar to that of the salt-ceramic composite. In the presence of

graphite, the manufacturing process is similar, but the final outcome is different. As in the case of the ceramic, during the sintering process the molten salt melts and thus pore imbibition is governed mainly by pressure difference. Graphite, however, unlike ceramic materials has a very low interfacial energy⁶⁰. Therefore, presence of graphite flakes in the mixture can lead to less favorable conditions for salt imbibition. This in turn leads to less volume of salt present in the sintered ceramic matrixes, less capillary forces and thus a coarser structure, which is more prone to leakage. It is thus conclusive that composite materials can only contain a small mass ratio of graphite to offset this type of phenomena.

To summarize, poor interfacial energy, which can be described through poor wettability between the interacting materials is in most studies identified as a detrimental parameter to the formulation process, structural stability and performance of the composite⁶¹.

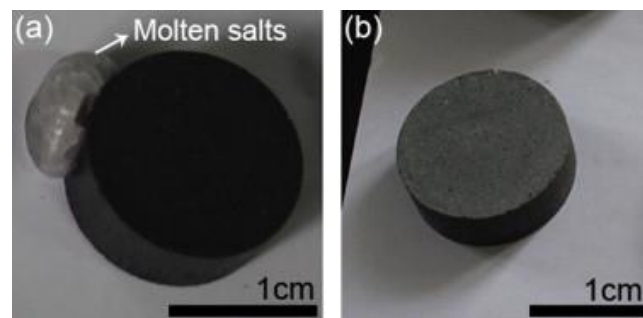


Figure 2.5 Images of molten salt composites without (a) and with (b) ceramic material. The leakage in the presence of a graphite matrix versus only MgO is evident⁵⁶.

The most frequently quoted measurement to characterize the wettability between to materials is the contact angle (CA). Knowledge of the CA is thus important as it dictates

the direction of the pressure gradient, based on its value. A lower CA between the molten salt and the MgO (high interfacial energy ceramic), translates to a higher wettability between the two. A wetting liquid contributes to the densification of the ceramic structure through the form of a capillary forces that pull the grains of the ceramic powder leading to a denser more arranged structure. The high surface tension between the ceramic and the molten salt makes the composite structure denser, while on the other hand the poor wetting properties of the particles as well as the expansion and reduction of the structure due to heat and cooling cycles appear to be creating stabilization problems.

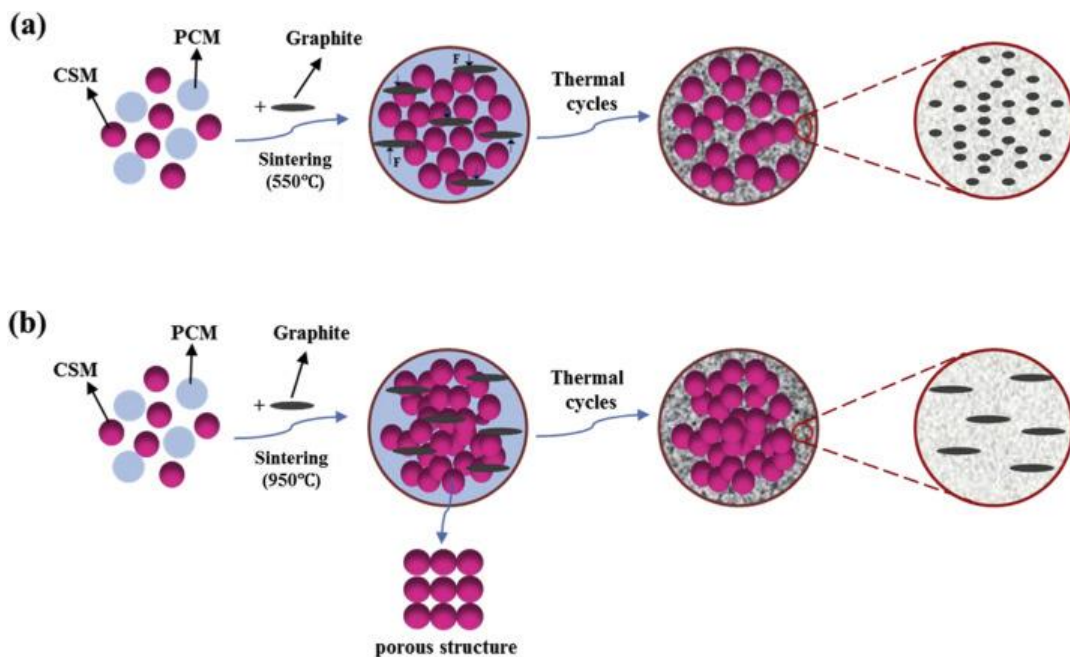


Figure 2.6 Schematic illustrates of microstructure development of CPCMs for (a) NaLiCO₃ based and (b) Na₂CO₃ based composites⁶²

On the other hand, a low wettability leads to air gaps and a larger mean pore diameter in the final product. These structural issues are closely related to the surface energy

and thus indirectly the wetting behavior of the material involved. Optimal selection of materials with favorable wetting conditions leads to maximization of the performance of the final composite structure. CA values of molten nitrate salts on ceramic and carbon surfaces are to this day still not present in the literature.

2.4 Studies on the wetting and surface tension of molten salts

CA studies on molten salts are mostly focused on salts used in nuclear or fuel cell applications. The largest work to date was carried out by Morel in the 1970s measuring the CA of LiCl, NaCl, KCl, LiF and NaBr in the proximity of their melting points⁶³. This is the largest work to date. In his work Morel conducted a highly precise purification method to ensure the best purity conditions. Furthermore, Morel studies the CA of these salts also with respect to time. He identified that the CA of the salts changed with respect to time, but not always in a linear manner. For LiCl an initial decrease was observed minutes after the measurement initialization and a subsequent increase after ~15min. This is probably due to a reaction occurring from the chloride salts on the surface, thus forming a rough ring due to cavitation formation at the triple contact point thus changing the solid-liquid interactions and increasing the CA. Nevertheless, the importance of salt purification, change of CA with time and selection of inert surfaces during molten salt CA measurements can all be concluded from this pioneering work.

A more recent work involving the wettability of chloride salts on graphite and glassy carbon was conducted by Baumli and Kaptay⁶⁴. In their work they studied the CA of pure NaCl, CsCl, RbCl and KCl as well as mixtures of NaCl-CsCl and ternary mixtures of NaCl-KCl-CsCl. The goal of their work was to investigate the activity of CsCl on the

graphite interface, which was identified and hypothesized to lead to the coexistence of $\text{Cs}_3[\text{NaCl}_4]$. They identified a strong dependence on the composition of the salt and the CA. Specifically, RbCl and CsCl proved to be wetting on graphite while NaCl and KCl non-wetting. Furthermore, a linear decrease in the CA was observed with a linear increase in the molar fraction of CsCl in mixtures of NaCl-CsCl. This was the conclusive evidence of the reaction occurring at the interface. Their work is interesting as it suggests the use of CA measurements for observations of possible reactions at the interface. Similar studies have been conducted by more authors on molten chloride salts⁶⁵.

A work on the wettability of molten Li^+ , Na^+ , K^+ and Cs^+ in glassy carbon tube was conducted by Stepanov⁶⁶. The aim of the work was to determine critical factors that affect the wetting of ionic high temperature melts. In order to do that, different compositions were tested. Furthermore, the charge of carbon surface was tuned. The CA was measured by meniscus weight method. The CA Na^+ and Li^+ were found to reduce with an increase in the surface charge. However, in the cases of KCl and CsCl a range of electric potential was identified, in which the CA remained stable⁶⁶. This denotes the importance of surface energy and ionic properties on the CA.

More recent studies involve CA of various molten salts on graphite to identify mechanisms behind the prevention of corrosion in molten salt reactors. Zhoutong et al, conducted a study on the wettability of molten FLiNaK on graphite, to correlate the results with corrosion in nuclear reactors. The effect of pressure and pore diameter of the graphite surface were related to the wettability of the molten salt⁶⁷. They identified that above a certain tensile stress, despite the non-wetting behavior of graphite, molten

salt imbibition in the pores occurs. This leads to a porosity of tension, which increases the diameter of the pores on the surface of graphite and thus gives spaces for larger volume of salt infiltration. Another study of the CA of molten FLiNaK on graphite was done by Lian et al, relating the preparation process of the graphite on the wettability of the salt⁶⁸.

Wyatt and Fisher correlated the CA of the molten carbonate eutectic ($\text{LiCO}_3\text{-NaCO}_3$) to corrosion effects on ruthenium, rhodium, palladium, platinum, silver and gold, materials frequently used in fuel cell applications ⁶⁹.

The only study regarding solar thermal energy storage was conducted by Chuan et al. They investigated the effect of the sintering temperature of MgO, on the wettability of molten NaLiCO_3 ⁷⁰. The sintered surfaces were prepared by compressing powder and then sintering at high temperatures ranging from 500 to 1300 °C. Different sintering temperatures led to different surface texture, which then affected the CA (Fig. 2.7). Different sintering temperatures provided MgO substrates with different structures, allowing their effects on salt penetration and hence wettability and surface energy to be investigated. A scanning electron microscope (SEM) was also used to study the morphology of the MgO prepared surfaces and then relate it to salt imbibition rates.

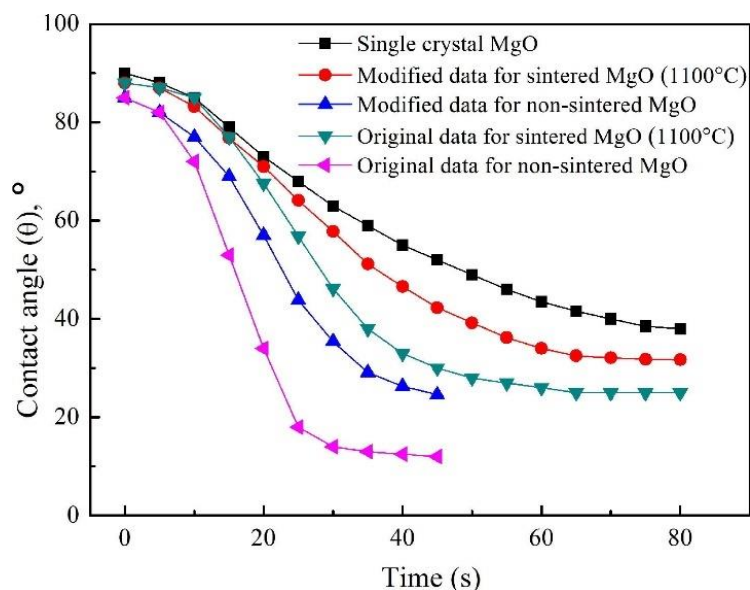


Figure 2.7 Effect of sintering temperature on the initial CA of molten NaLiCO₃ on MgO (Adapted from ⁷⁰)

The wettability in all cases was good independent of sintering temperature. However, the non-sintered case demonstrated considerably higher wettability than the others. This was attributed to larger pores, which give room for salt imbibition. On the other hand the crystalline MgO demonstrated the least wetting profile, as the pore size there is the lowest. Higher sintering temperature led to a less wetting profile and this was linked to the surface energy. This was done through AFM measurements of the adhesion forces of the MgO substrates.

To this date, no research has been conducted on the CA of molten nitrates, the most frequently used molten salts in currently operating CSP plants.

In summary, from the review of existing CA measurements of molten salts on various surfaces the importance of sample purity, sample aging, reaction and surface roughness are identified as crucial to the conduction of correct measurements. The

most preferred method as by previous works is the static contact angle. Finally, the lack of CA data of molten nitrates on ceramic and carbon surfaces is also observed.

2.5 Molecular Simulations of Contact angle of Nanodroplets

2.5.1 Introduction and Recent Advances

Wetting of solid surfaces by fluids is a phenomenon of particular interest in many disciplines, primarily in surface science, materials characterization as well as oil and gas recovery ⁷¹. MD simulations are a promising pathway for prediction of surface wetting. The evolution of computers and emergence of more accurate force fields further enables this route. Aside from prediction of experimental values in difficult or impossible conditions to reproduce, such as surface tension of water in vacuum, MD simulations can also offer insight on liquid-solid interactions, ordering in interfaces and polarization, which can be used to design novel surfaces and membranes that can aid in numerous modern engineering problems (i.e. water-oil separation membranes).

The wettability of a liquid on a solid surface is most commonly assessed through the CA. The static droplet method is the most frequently used experimental method to measure the CA. Despite the difference of several orders of magnitude, from nano to macroscale droplets, CA measurements from MD simulations are considered in general to be a reliable method to obtain information on the wetting behavior of a liquid. The most important issue when going from micro to nano size are factors related to droplet size such as the Tolman length and the line tension effect, which describe the effect of scale on the surface tension and liquid-solid interaction respectively.

Calculating the CA in MD simulation involves the placement of an equilibrated liquid droplet on the solid surface and a subsequent equilibration of the system. The required equilibration time to obtain an accurate value is dependent on several factors, such as the liquid viscosity⁷², the net interaction between the liquid and the surface, the type of thermostat used⁷³ and the system size⁷⁴. Koumoutsakos et al⁷⁵ demonstrated that a stable droplet shape can be obtained after a couple of ns of simulation, while other researchers show that simulations of up to 100ns are necessary⁷⁶. Furthermore, two types of droplets are used spherical or cylindrical. Cylindrical droplets have the advantage of periodicity in 2 dimensions (x or y, and z) and thus in theory show less change in size due to line tension effects⁷⁷. Simulations though have shown that the effect of line tension is present regardless of geometry⁷⁸.

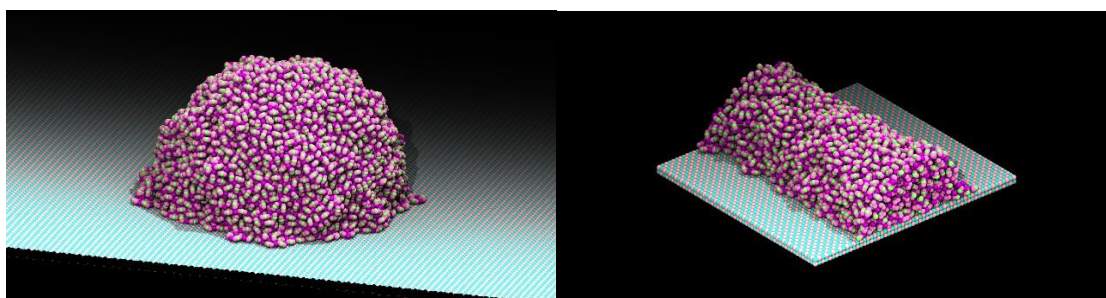


Figure 2.8 Molecular simulation of contact angle. Spherical (left) and cylindrical (right) geometries are the most commonly used.

Calculation of the CA from the equilibrated droplet shape occurs typically in the same manner as in experiments by obtaining the profile of the droplet and calculating the angle between the surface and the tangent at the triple contact line. However, these early algorithms suffer, as all cross-section studies, from an assumption of a uniform cylindrical or spherical droplet shape. In terms of cylindrical geometries that might be less crucial, but original simulations involved mostly spherical droplets, which have

several different faces. Thus, to obtain a reasonable estimate of the CA values of several faces were averaged. Given the large number of faces in a sphere newer algorithms have employed more sophisticated techniques. Santiso et al. developed a novel algorithm based on surface meshing. The CA is calculated locally in every predefined mesh point along the three-phase contact line. The meshing density can be increased to improve accuracy⁷⁹. Khalkhali et al. developed a more robust algorithm based on the convex hull method, which triangulates the droplet, The angles between the vector normal to the solid surface are then calculated and a distribution of θ -values is obtained ⁷⁴. This algorithm is substantially more robust than other state-of-art algorithms and shows less effects in terms of scale⁷⁴. Finally, Ravipati et al. used a droplet density profile algorithm in order to correctly identify the droplet/surface interfaces and estimate the corresponding CA values⁸⁰.

2.5.2 Studies on finite size effects

For the nanoscale droplets that are typical of MD simulations, the forces at the triple contact line are determined not only by the interfacial tensions, but are also influenced by the apparent line tension, τ , which is the excess free energy per unit length of the three-phase contact line. Thus, the CA derived directly from the equilibrated droplet geometry can differ substantially from the actual CA. This is particularly true for spherical droplets. For this reason Young's equation has been modified to account for such line tension size effects ⁷⁷. Indeed several studies have shown dependencies of the calculated CA on droplet size both numerical and experimental ^{81,82}. However, the magnitude of this dependency arising from these length scale effects has not yet been precisely determined; in particular, both the value and the sign of τ , as well as its

dependence on the surface energy or the surface tension of the fluids in question remain poorly understood. Simulations have reported τ -values differing by several orders of magnitude ^{74,77}.

Recent research has identified that the originally proposed modification in Young's equation essentially includes a term, which is coined to be the “apparent” line tension and not the absolute value. This tension can be further decomposed to three contributions, the original mentioned line tension effect, the Tolman contribution to the surface tension and a 3rd contribution called line tension “stiffness. This is described as the “stiffness” of the change in line tension, not expressed through change in the excess free energy, but through change in the CA in given thermodynamic conditions⁷⁸. Calculations have shown that for droplet sizes with radii larger than 2 nm these high order corrections to the contributions can be neglected. Therefore, the line tension, τ , ought to also depend on the contact line radius and Tolman length for relatively small radii⁷³.

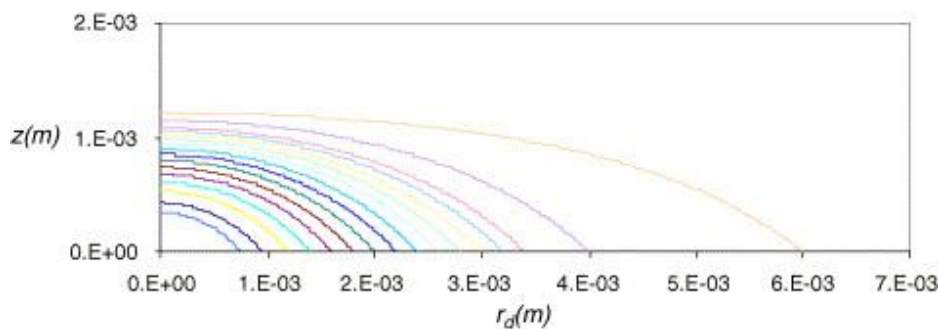


Figure 2.9 Effect of droplet size on droplet shape. Modelled by first-principle dynamics based on Young’s equation⁸³.

Important insights into some of these contributions have been provided by state of art works that investigate how the CA varies with droplet size. Zhang et al.⁷² studied

spherical water droplets on Lennard-Jones (L-J) substrates with varying LJ-water attractions (polarity) and found that the CA had a significantly higher dependence on the “stiffness” for hydrophilic surfaces than for hydrophobic surfaces⁷⁷. In another work Kanduc through MD simulations, calculated the CA of both spherical and cylindrical (essentially infinitely long in one dimension) H₂O droplets on a self-assembled monolayer surface. Likewise, the polarity of the monolayer was adjusted, and the CA was examined for various systems. Similar to other works⁷⁸, the CA was found to depend heavily on droplet size, with a dependence more pronounced for hydrophilic surfaces with higher polarities. Interestingly, though it was noted that although the cylindrical geometries account for one less dimension, when expressing the apparent line tension, they were found in all cases to be dependent on droplet size, but with values slightly lower than the spherical cap droplets.

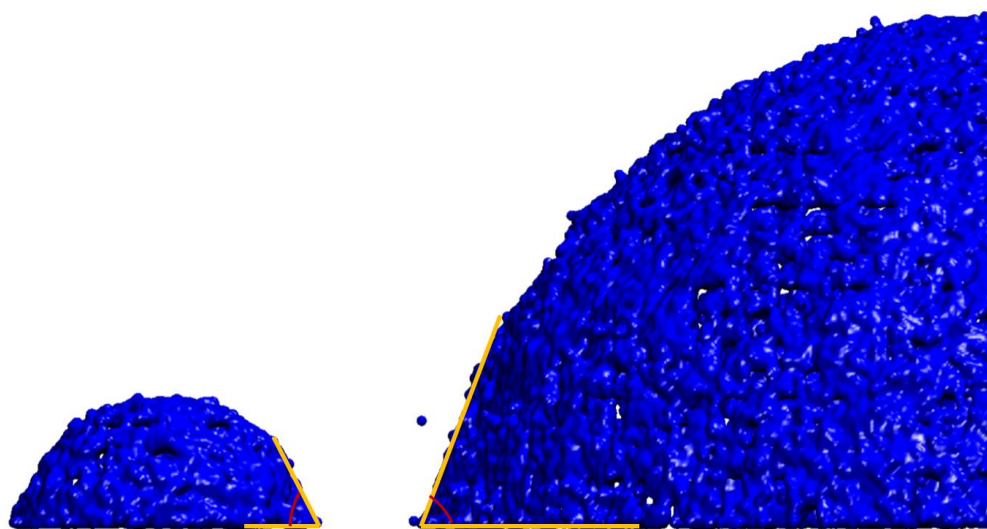


Figure 2.10 Effect of droplet size on the calculated contact angle. Equilibrated trajectories of droplets with different sizes from molecular dynamic simulations (adapted from⁷⁹).

2.5.3 Studies on systematic errors in contact angle calculations

As mentioned earlier calculating the CA through MD simulations is challenging due to the difficulty of extracting the correct droplet shape from the simulation trajectory. A spherical droplet, even for larger sizes can have inconsistencies through its faces thus making it difficult to identify the location of the tangent through, which the angle can be identified (Fig. 2.10). Furthermore, the exact profile of the solid-liquid interface is not unambiguously defined but is also dependent on the scaling size effects. Its choice is thus dependent mostly on the definition of the density boundary, which for low density liquids is very challenging. Interestingly, Zhang et al. calculated CA values obtained through different three-phase contact planes and found that despite their initial differences in absolute values, they all converge to the same macroscopic CA upon extrapolating to infinite contact line radius⁸⁴. This can be translated to the fact that the apparent line tension present in Young's equation describes the uncertainty of the CA value due to size effects. Therefore, size effects do not only concern the droplet radii, but also the height and shape of the profile of the different planes. This can be further understood from the fact that the corresponding uncertainty of height of the contact plane is proportional to radius of the droplet in the z axis. This effect is expected, and its corresponding uncertainty is more pronounced in smaller sized droplets. Moreover, for simulated droplets of a given size, this uncertainty is more pronounced for hydrophobic surfaces, since they are supported on smaller radii. In the case of cylindrical droplets, such estimations of the contact line are less arbitrary and suffer from smaller finite size corrections, most likely due to the fact that one dimension is infinitely extended and thus does not suffer from size effects. To completely avoid errors associated with size effects, multiple simulations of varying droplet size should

be conducted and then the values obtained should be extrapolated to infinite lengths (macroscopic) in order to correctly estimate the CA⁸⁵.

2.6 Molecular Simulation of Molten Salts

2.6.1 Structure

MD simulations of molten salts is an ongoing issue, starting in the late 1970s. The first works aimed to validate interatomic parameters of molten chlorides, due to their applications in nuclear energy. Studies were conducted on the structure of molten sodium, potassium and lithium and rubidium chloride⁸⁶⁻⁸⁸. Studies on chloride are ongoing until today⁸⁹. Recently, Ding et al., studied the structure of NaCl and KCl and their mixtures and accurately calculated their properties using RNEMD methods⁹⁰. In a similar work, Bengtson et al. investigated LiCl- KCl mixtures focusing on the changes in local structures and topological distributions⁹¹. Wang et al, computed the transport properties of LiF-BeF-ThF₄ molten salt, using a polarizable force field, and observed that the electrical conductivity increases rapidly from 873K to 1273K, while the opposite was observed in the case of the viscosity^{92,93}. Sun et al., also performed a study on 4 binary chloride systems (LiCl-RbCl, LiCl-CsCl, NaCl-RbCl and NaCl-CsCl). The study examined the impact of LiCl and NaCl on both the structures and the transport properties of RbCl and CsCl. It was observed that the positive ions lead to weaker interactions between the counterions and hence affect the final structure of the mixture⁹⁴. In terms of molten carbonates in another study by Ding et al., a series of calculations regarding local structures and transport properties were performed for binary carbonate mixtures of Na₂CO₃ and K₂CO₃ and in a subsequent publication the effect of the molar compositions on the local structures of the molten carbonate

eutectics was further investigated ^{95,96}. The first MD work on nitrates mixture, to the best of knowledge, was conducted by Adya et al. ⁹⁷. Mixtures of NaNO₃ and NaNO₂, including their eutectic, were examined by means of MD simulations. This study highlights the excellent agreement between the MD calculation and x-ray diffraction measurements. A more recent study on the specific heat capacity and thermal conductivity of molten NaNO₃, including the effect of SiO₂ NPs, was conducted by Qiao et al. ^{98,99}. This study attributes the enhancement of the specific heat capacity to structural changes in the liquid-particle interface, caused by the NPs. Jayaraman et al ¹⁰⁰, calculated the liquid and crystal phases of NaNO₃, LiNO₃ and KNO₃ as well as their viscosities, thermal conductivities and specific heat capacities at 773K. Excellent agreement with experimental values was found for all properties investigated. In a subsequent study ¹⁰¹, the free energy and melting point of the mixtures of the three nitrates, in various concentrations, was also investigated. The behavior of Solar Salt with various concentrations of Al₂O₃ nanoparticles was investigated by Yanwei et al ¹⁰². A set of 'ad hoc' Lennard-Jones parameters was proposed with the purpose of investigating the interaction energy of the NP on the base fluid. The study outlined the increase in coulombic forces in the presence of NPs, as well as its effect on the specific heat capacity. Ni et al, modified the potential of Jayaraman, by changing the intramolecular parameters (bond, angle and improper forces). With this adjustment on the original Buckingham potential, an improved local structure prediction and property calculation was achieved. Furthermore, a mixture of NaNO₃ and KNO₃ was also simulated and the viscosity, thermal conductivity and density were calculated, with good agreement ¹⁰³.

The accuracy of MD calculations depends on the availability of validated interatomic potentials. In the literature, several Lennard-Jones potentials are available for NaNO_3 and KNO_3 in aqueous solutions. These parameters, however, are not designed for molten phases. Buckingham parameters for pure molten NaNO_3 and KNO_3 do exist but are not suitable for mixtures mainly because mixing rules, like the Lorentz-Berthelot rules for the Lennard-Jones potential, are not available for the Buckingham potential. There are, therefore, no available interatomic potentials for the simulation of the solar salt.

2.6.2 Surface Tension and Wettability

The first work on the surface tension of molten salts is conducted by De Gama et. Al¹⁰⁴. In their study the liquid-vapor interface of a molten alkali halide was simulated, and the surface tension was predicted in good agreement with experiments. Density profile was also accounted for to accurately establish the liquid-vapor interface. This was readily done, as early trajectories denoted the existence of clustered ions at the liquid-vapor interface with large vacuum cavities in between (Fig. 2.8). In this model the anion and cation are represented by hard spheres of equal diameter R and opposite charges. An approximation of the free energy of the fluid was achieved using the square gradient approach. The authors experimented also with the diameter of the anions and cation in the molten salt. The surface tension was found to decrease linearly with temperature. They compared their calculated values in terms of accuracy with a previous similar model used for molten KCl , as well as with experimental data for the studied salt. In both cases agreement was satisfactory (<34% deviation).

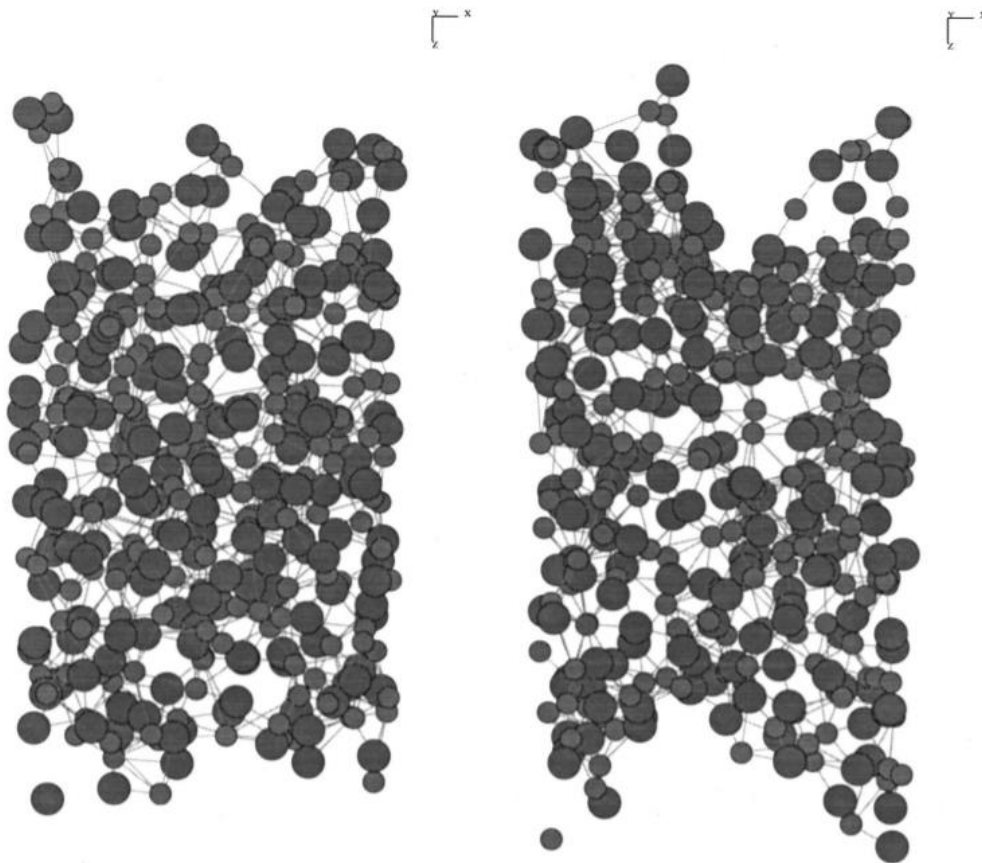


Figure 2.11 Simulation trajectory snapshots denoting the existence of clustered ions and vacuum cavities at the vapor molten salt interface. (Adapted from ¹⁰⁵)

Similar work was conducted by Aguado et al on KI¹⁰⁵. The surface tension of the molten salt was calculated through MD simulations. A sensitivity analysis was conducted with respect to the width of the interface, the long-ranged electrostatics computational methods and the boundary conditions of the simulation. Vacuum boundary was deemed mandatory for the correct equilibration of the liquid vapor interface, due to the correct dispersion of the long-range electrostatics. On the contrary in periodic conditions along the z axis the calculated surface tension was found to decrease significantly. Finally, an increase in the interfacial width led to a decrease of the calculated surface tension, showing some degree of dependency to the system size.

This was investigated furthermore in a second work by the authors ¹⁰⁶. They identified that in systems larger than 1000 molecules finite size effects were observed due to the way van der Waals liquids are predicted in basic capillary wave theory. Further analysis conducted on the scaling effects on the interface, found that the local structure appeared to be clustered due to capillary waves. Changes in the computation algorithm involved in the calculation of the long-range electrostatics were able to eliminate these effects. This led to a very good agreement between experimental and calculated values. These suggested changes to the electrostatic meshing and calculations are included in the LAMMPS software used in this work.

In their final work the structure and surface tension of the liquid–vapor interface of molten LiCl and KCl, as well as mixtures of the two, in different concentrations were examined ¹⁰⁷ through MD simulations and using a slab geometry (electrostatic corrections). A dependency of surface tension on the composition and temperature of the liquid was conducted and found to be in good agreement with experimental data. Interfacial structure analysis showed asymmetry and discontinuities in the liquid-vapor interfaces. These were noted to be more apparent in LiCl rich solutions than in KCl suggesting that the ion size and thus polarization interactions play a role in the correct equilibration of the interface. These were then shown to be less significant at larger system sizes. Additionally, they suggest that very long simulations in the range of nanoseconds, with small timesteps in the range of picoseconds, are required to obtain a correctly equilibrated liquid-vapor interface. As a rule of thumb for all the systems studied, they note that the local ion coordination number reduces to 50% of its bulk value only when the ion density has been reduced to less than 5% of its bulk value.

Several MD studies have addressed the wetting behavior of salts on surfaces. However, these works on their entirety are focused on the simulation of ionic liquids and not molten salts. Burt et al, for instance, investigated the effect of the droplet size and the interatomic potential on the CA of 1-ethyl-3-methylimidazolium tetrafluoroborate on graphene ¹⁰⁸. Guan et al. studied the CA of droplets of 1-ethyl-3-methylimidazolium ionic liquids on a silicon surface ¹⁰⁹. They examined the drop size effect and found it to significantly change the liquid-substrate net interaction, the final CA and the orientation of the atoms on the surface. Malali and Foroutan examined the wetting behavior of 1-methyl-3-butylimidazolium and fluorophosphate on titanium dioxide (1 1 0) surface¹¹⁰. They found that on the surface of the TiO₂ a cation layer is created, leading to an anion-rich layer on top of it. A critical point to be made is that all the above mentioned works focus on the investigation of the solid liquid interface and do not go into the process of validating the predicted CA values, to examine if the force field used in each case can accurately predict the CA accounting for length and size scale effects.

The only study of the wetting behavior of molten salts was conducted by Qicheng et al. ¹¹¹. They employed MD simulations to investigate the wettability of molten sodium sulfate salt on nanoscale calcium oxide surfaces at high temperature in order to better comprehend the micro-mechanisms effect on the molten salt with higher goal of promoting the performance of thermochemical energy storage. They report the molten sodium sulfate to be wetting the calcium oxide at lower temperatures (i.e. 500K). Increasing the temperature led to an increase in the spreading rate of the molten salt

and a lower CA value. Furthermore, through RDF and diffusion coefficient studies they identified that the molten salt activated the ions at the oxide surface and caused weak fluidization of the surface at temperatures way below its melting point. Finally, they conducted wetting studies on a spherical surface and identified that at higher temperatures complete coverage of the calcium oxide sphere envelopes. The formation of this molten salt layer led to prevention of the sintering of the calcium oxide.

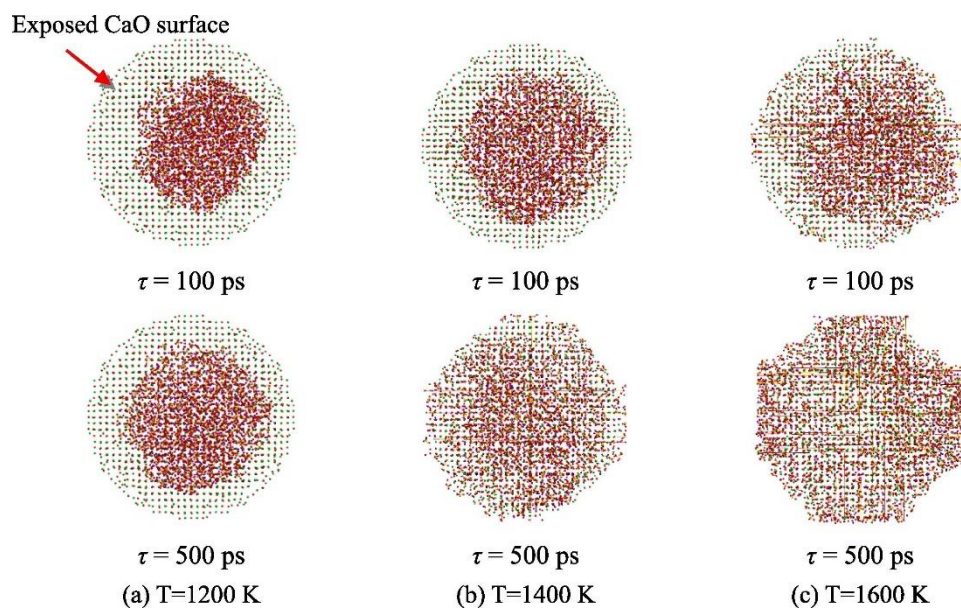


Figure 2.12 Sodium sulfate melting on the spherical nanoscale calcium oxide substrate at different temperatures¹¹¹.

2.7 Molecular Simulation of wetting of Nanofluids

Unfortunately, no MD studies have been conducted on the wetting of MSNFs. Since, MSNFs are a relatively young field of research the wettability has not been yet investigated. Generally, MD simulations of wetting of nanofluids is limited to very few works.

A work was conducted by Qiang et al ¹¹² involving liquid argon with copper NPs. Several NPs (diameter of 1nm) were evenly distributed in the solution. The principal objective of the authors was to evaluate the effect of NP concentration and thus the subsequent change in the surface energy on the wetting and subsequent evaporation of the liquid. To better interpret the interactions in the solid liquid interface, the liquid solid interaction was tuned from extra lyophobic to extra lyophilic. Variations were observed. In the lyophilic scenario a further increase in the surface energy coefficient contributed to the wetting and evaporation process, while the opposite was true for a lyophobic interaction. In terms of NP concentration, the solid- liquid interaction was found to play a critical role. In the lyophilic scenario the CA was further reduced with an increase in NP concentration. However, the contribution to the evaporation rate was negative. In cases of neutral or lyophobic interactions, changing the NP concentration had no effect on the calculated CA, but contributed positively to the evaporation process. The magnitude of enhancement is found to decrease with increase NP concentration. Additionally, the onset locations of the evaporation were different for each scenario. For lyophilic interactions the evaporation first appeared near the three-phase line and was reduced towards the center of the drop's surface. In the lyophobic cases the opposite trend was observed. Evaporation begins from the top of the droplet.

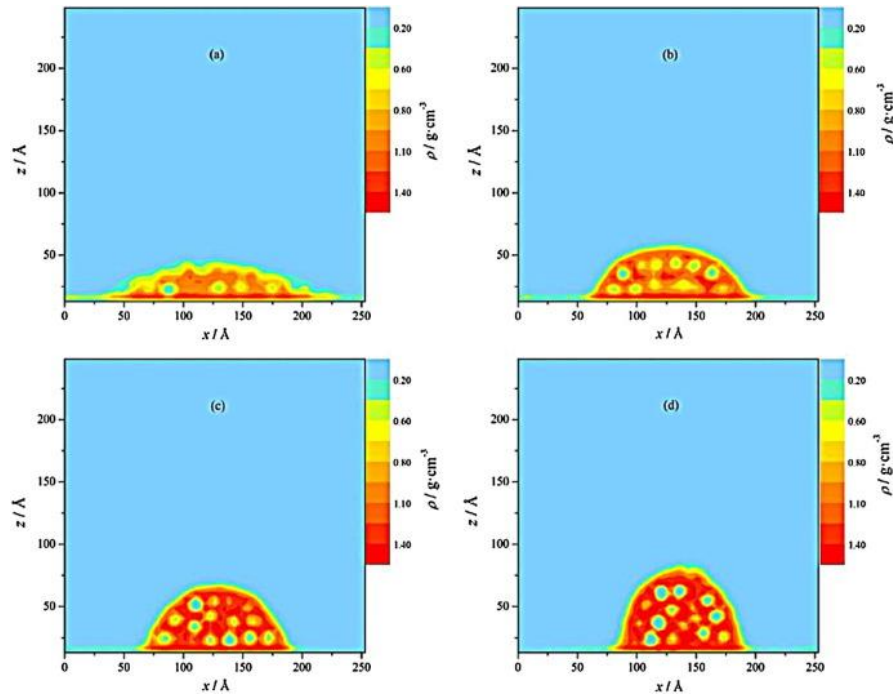


Figure 2.13 2-D mass density profiles of sessile nanofluid nanodroplets with different solid liquid interactions. Top left being the most lyophilic and bottom right the most lyophobic¹¹².

In another work by Wang et al ¹¹³ the behavior of NP doped droplet on a L-J substrate is investigated. The interaction forces are tuned, thus affecting the spreading behavior of the droplets on the solid substrate. Additionally, the effect on the wettability, and subsequent to the boiling, NP deposition on the solid surface is also evaluated. An enhancement mechanism caused by the NP deposition on the boiling heat transfer is observed. In four different interaction scenarios, the wetting behavior of a nanosized droplet with and without NPs was analyzed. The droplet with NPs showed in all cases a smaller CA (improved wettability). To further strengthen these results, the rapid boiling behaviors of a fluid with and without NPs were simulated. Through this model the mechanism of behind boiling of nanofluids was investigated. A faster boiling rate was observed in the presence of NPs. This was assessed by calculating the density distribution of the water molecules and observing locations where they have

transitioned to gas phase. The NPs deposited on the surface resulted were noted to increase the density on the solid-liquid interfaces, thus facilitating higher heat transfer, which translated to an environment more favorable for boiling.

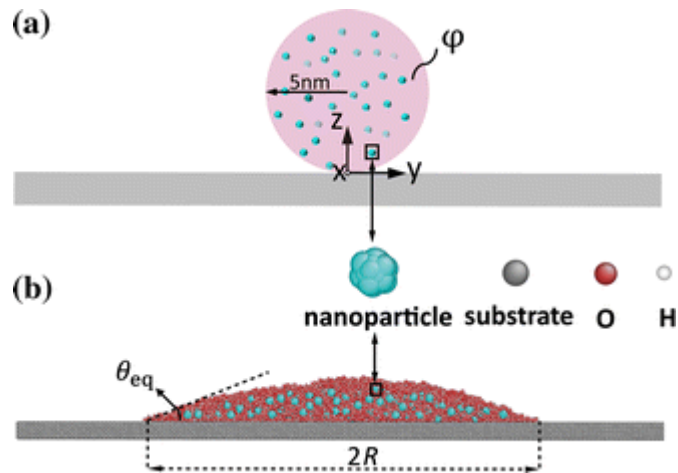


Figure 2.14 a) Diagrammatic drawing of the initial configuration of the simulation system: a cylinder nanofluid droplet laden with well-dispersed nanoparticles is placed on the solid substrate. ϕ denotes the nanoparticle volume fraction. b) MD snapshot of the nanofluid¹¹³.

In another work by Taheri et al, the effects of surface wettability and NP concentration on boiling of ferrofluids were investigated with the application of a tuned magnetic field. In this work liquid Ar was considered as the base fluid and was modeled through a L-J force field. Two different NPs were considered; one hydrophilic and one hydrophobic. Preliminary CA studies on these surfaces calculated an angle of 40.5° for the hydrophilic and 130.6° for the hydrophobic surface. Subsequently, a single NP was added in the center of mass of the liquid to investigate its effect on bubble formation during wetting on a uniformly heated solid surface. Strong relationship between the NP presence and vapor rate formation, nucleation and wettability were established. Compared to the base case the existence of a hydrophilic magnetic particle led to a

smaller boiling film created in the solid-liquid interface. On the other hand, the existence of a vapor layer in the interface was more pronounced in the case of a hydrophobic material. Additionally, the authors altered the magnetic momentum of the added NPs. A relationship was established between momentum change and evaporation rate, with a stronger magnetic force leading to a lower evaporation rate.

2.8 Summary

This section summarized the literature surrounding the research on the wettability of molten salts. The wettability is found to interplay in the corrosion and composite material formulation, both issues concerning the performance of CSP plants. The best way to assess the wettability of a material is the CA. However, the CA data for molten nitrate salts have to our knowledge not been produced previously. Furthermore, wettability of molten salt nanofluids is an issue that aside from this work remains still uninvestigated.

On the modelling side a state-of-art review of modelling nanodroplets is conducted and a lack of optimal pathways to eliminate scaling and length size effects from nano-wetting simulations is identified. Regarding the surface tension, ion size and polarization effects are identified as critical to the correct simulation. Wettability of molten salts and particularly molten nitrate salts on solid substrates is found to be lacking.

This PhD thesis will therefore concentrate on studying the effect of NPs on the wettability of the molten salt and subsequently its stability. This will be done firstly experimentally and subsequently using MD simulations, which can provide further insight into the solid-liquid interface of both the NPs with the salt and the MSNF with various surfaces.

Chapter 3 MATERIALS AND METHODS

In this section the materials and experimental methods used in this work are described in detail. Furthermore, the principles of MD simulations are discussed in detail, as well as the computational routines employed to calculate the various material structural and transport properties.

3.1 Materials used in Experiments

In this work the wettability of molten salts is investigated. The salts most frequently used in TES are nitrate and carbonate salts. As discussed, they are all enhanced with NPs to improve their thermal properties. Therefore, in this work a selection of nitrate salts and NPs are used.

The salts used in this work are LiNO_3 , NaNO_3 and KNO_3 . Secondary studies are also conducted on mixtures of Li_2CO_3 - Na_2CO_3 - K_2CO_3 . The vendor is Sigma-Aldrich and the purity of all samples are 99.0%. No further purification process is conducted on any salts. The NPs with percentage weight ratio varying as 0.5, 1.0, 1.5, 2, 5 and 10 wt. %. Amorphous SiO_2 is chosen to be a suitable candidate for establishing a stable MSNF,

due to its density being very close to that of molten nitrate salts. The silica particles were obtained from US Research Nanomaterials, Inc. and have the following characteristics:

- Purity: 99.5%
- Average Particle Size: 15-20nm
- True Density: 2.2 g/cm³
- Morphology: nearly spherical

Further to the silica particles carbon particles were also used in this work. Similarly, to the amorphous silica the bulk density is close to that of the salt. These varied in diameter and morphology with aim to study the effect of these issues on the wettability. They were also obtained from US Research Nanomaterials, Inc. Their properties are listed in Table 3.1. Silica is known to be hydrophilic, while carbon surfaces have the opposite effect. For this reason, this combination is thought to lead to some insight of how salt-nanoparticle wettability can interplay in the stability of the MSNF.

Table 3.1 Specifications of the graphite particles used in this work.

	Graphite Flakes	Graphite Nanosphere	Graphite Microsphere
Diameter	150µm	50nm	500µm
Purity	99.5%	99.5%	99.5%
True Density	2.266 g/cm ³	2.266 g/cm ³	2.266 g/cm ³
Morphology	Rhomboid	Spherical	Spherical

The CA is tested on various surfaces to check the wettability. These varied in terms of roughness and type. These can be found in the table at the start of the next page:

Table 3.2 Surface types used in this work and their respective roughness.

Surface Type	Roughness (μm)
MgO (1 0 0)	0.67
MgO (1 1 0)	0.54
Al ₂ O ₃ (polycrystalline)	0.346
SiO ₂ monocrystalline (1 0 0)	0.254
Fused Quartz (polycrystalline)	-
SS304 (polished)	0.432
SS327 (polished)	0.385
SS414	1780
Silica Carbide	0.343
Graphite	1380

3.2 Sample Preparation

For the preparation of the molten salts a melting process is followed. In both cases the samples are mixed and then dried in the oven for 12h at 120 °C to remove any excess moisture. The Solar Salt is prepared by mixing 60% NaNO₃ with 40% KNO₃ and the ternary carbonate by mixing 34.5% K₂CO₃ - 33.4% Na₂CO₃ - 32.1% Li₂CO₃ (weight concentrations). Subsequently, the nitrate salts are melted at 390 °C for 24h and the ternary carbonate salt for 12h at 600 °C in order for the samples to reach homogeneity. The molten salt mixtures are prepared using the method reported by Madathil et. al.¹¹⁴.

The mixing method for the molten salt-based nanomaterials used in this study is shown in Figure 3.1. The respective salt and NPs are first weighed on an analytical balance with 0.1 μg precision (Mettler Toledo, model XP6U). The nanoparticles are then

dispersed in distilled water and mixed using an ultra-sonication bath (model Fisher scientific, CL334) for 15 minutes. Subsequently, the respective salt is added to the mixed solution and the mixture is further sonicated for another 15min. Naturally, the amount of distilled water is analogous to the solubility of the salt in each case. The solution is then placed in the oven where it is dried overnight at 130 °C. The powder is then extracted and milled resulting in the salt-nanomaterial. This sequence is taken from Sidik et al. and is called the triple step method¹⁵. Images showing the preparation process can be found in appendix B.

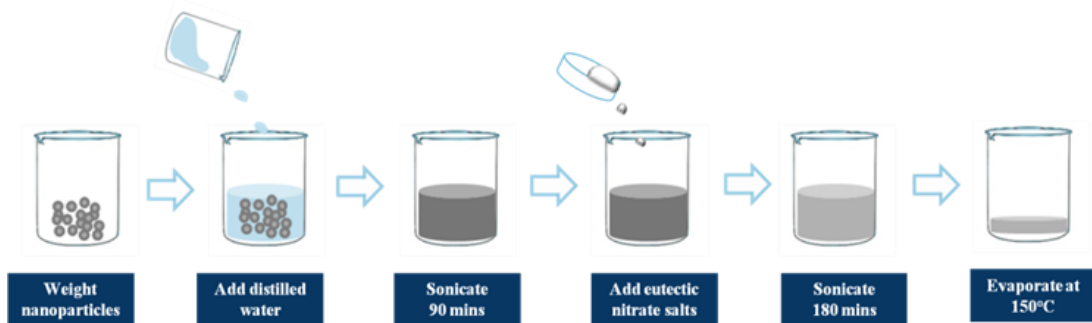


Figure 3.1 Preparation process for the formulation of molten salt nanofluids.

Regarding the corrosion tests involved in this work SS310 and SS347 are used. Their chemical composition is described in Table 3.3. Before the corrosion tests, pieces of 20mm x 20mm x 3mm of materials are polished successively with 240 and 2500 SiC sandpaper, followed by cleaning in an ultrasonic bath for 20 minutes. Graphitization of the surfaces is conducted by coating with Graphite 33 spray obtained from Kontakt Chemie according to the procedure described elsewhere¹⁸. In this case, the mass of graphite in the system is very low, suggested by manufacturer to be $\sim 5 \cdot 10^{-3} \text{ g/cm}^2$. This corresponds to about 0.08wt% of graphite in the salt. In order to check the

corrosion inhibition effects of graphitization, non-coated pieces of stainless steel are used as a reference sample.

Table 3.2 Chemical composition of the stainless-steel surfaces used in the corrosion studies

	Fe	Ni	Cr	Mn	Si	P	C	S	Nb	Ta
Stainless steel 347	Balance	10.7	18.3	2.0	0.75	0.045	0.08	0.03	0.41	0.21
Stainless steel 310	Balance	19.1	24.9	1.81	0.64	0.03	0.05	0.01	-	-

3.3 Experimental Methods

3.3.1 Contact Angle (CA)

CA measurement inconsistencies are subject to several factors ¹¹⁶. Most notable factors are the surface roughness, drop dimension and heterogeneity. Samples of 0.1g are weighted using a $\pm 0.1\mu\text{g}$ scale (Meter Toledo). They are then milled and after compressed at 120MPa for 3min in a 4mm compression dye. In this way drop dimension and heterogeneity related effects are minimized. This compressions load is found to yield pellets with density close to that of the bulk (i.e. <10% difference). Higher compression loadings are not found to improve the resulting pore volume. Various substrates are selected for the measurement of the CA, which are listed in section 3.1. All substrate dimensions are 30mmx30mmx10mm, which is the sample holder area of the CA apparatus. All substrates are cleaned in an ultrasonic bath first with ethanol and then with distilled water, for 30 min cycles in each case, followed by high pressure air drying. In the case of the graphite the substrate is left overnight in the furnace at 250 °C to ensure complete evaporation of any trapped water. The roughness of the

substrates is tested in an ADE Phase Shift MicroXAM interferometer. The measured roughness values of the substrates used can be found in Table 3.2.

To control the effect of roughness, measurements are performed before and after every test. Roughness is found to be stable in the non-reactive cases (i.e. substrates). In the cases of metals such as stainless steel or carbon steel the roughness appears to increase, possibly due to oxidization and corrosion. These surfaces are therefore used for only one measurement and are then discarded.



Figure 3.2 The ADE Phase Shift MicroXAM Interferometer used for roughness measurements

Experiments are conducted on a KRUSS DSA 100M high temperature CA apparatus. The CA is determined using the KRUSS Drop Shape Analysis software. This involves a contour recognition of a grey-scale image, followed by a geometrical fitting of the drop shape on the contour grid. Conic section method is applied to determine the CA, being the recommended technique by the manufacturer for the 10-100° range. The circle method is also tested for angles in the 10-80° range and the tangent method in

angles $>80^\circ$ to ensure result consistency. In order to obtain confident results a series of 5 measurements are conducted, the results of which are averaged. Statistical deviations from average are also assessed. The KRUSS Drop Shape Analysis software states its statistical error at 0.1° although research has shown that actual error measurement is $\pm 2^\circ$. The image is obtained from a Stingray F-046 camera. The image resolution is 640×480 .

CA measurements are conducted either in air, argon or medium vacuum (25 to 10^{-3} torr). In the case of the helium a purging cycle is conducted at room temperature. The air is removed using the vacuum pump after which helium is introduced. This cycle is repeated 6 times to ensure no air is present in the chamber. Subsequently the pressure of the helium is set at 1.05 atm to ensure no air enters the chamber after the purging sequence is concluded

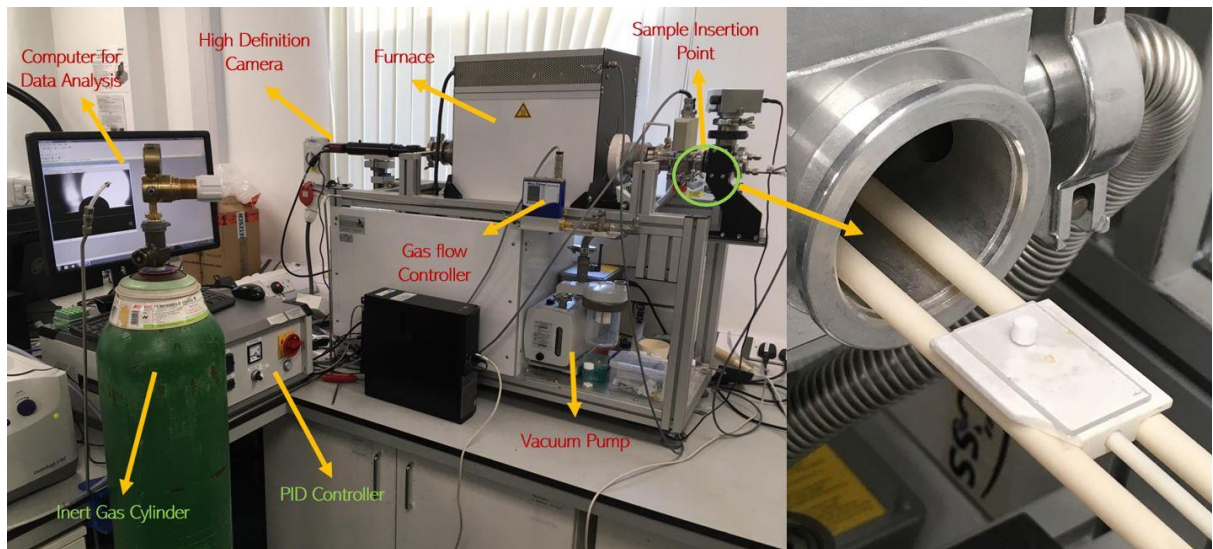


Figure 3.3 The KRUSS HT Contact Angle apparatus

3.3.2 Rheometer

A rotational rheometer (MCR 502, Anton Paar) and a parallel plate (35mm) are used to measure the viscosity of the base fluids and nanofluids over a shear rate from 10 s^{-1} to 250 s^{-1} . The viscosity is determined in an interval of $25 \text{ }^{\circ}\text{C}$ right after the melting point of each material: $225 \text{ }^{\circ}\text{C}$ for Solar Salt, $310 \text{ }^{\circ}\text{C}$ for sodium nitrate and $335 \text{ }^{\circ}\text{C}$ for potassium nitrate. A total of 34 points are collected in each temperature step following a logarithmic data acquisition ramp. A sample mass of 1.8 g is used in each measurement. The measurements are conducted under air flow rate of 1 L/min and each formulation is repeated 4 times (one of the most deviated value is discarded). The error of the equipment according to the manufacturer is $\pm 5\%$.

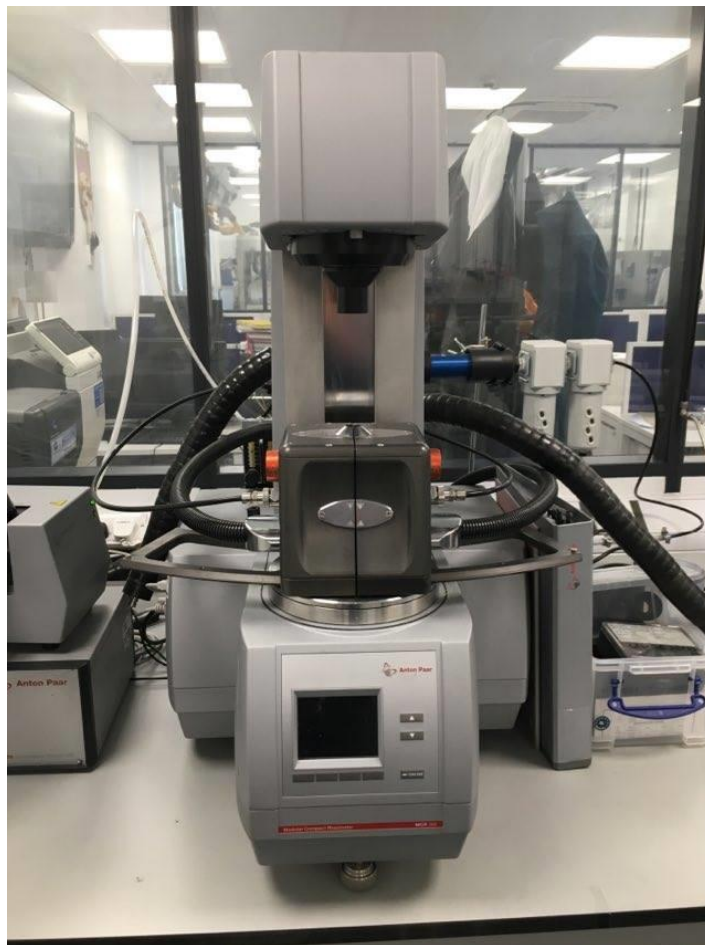


Figure 3.4 The Anton Paar MCR 502

3.3.3 Differential Scanning Calorimetry (DSC)

In this method a series of thermophysical properties such as melting point, latent heat and specific heat capacity of the molten liquid can be obtained. During a test, a sample and a reference are tested simultaneously while the temperature of sample and reference are increased at the same rate throughout the experiment. It detects the difference in heat flow to the sample and a reference as a function against temperature or time to monitor the thermal properties of the sample. The reference is an empty container while the sample is held in an identical one.

3.3.4 X-ray Diffraction (XRD)

This technique was used to analyze the chemical compound and crystal structure of the sample. Arrays of atoms scatter X-ray waves through the atoms electrons to produce secondary spherical waves emanating from the electron. By measuring the array of spherical waves, the arrangement of the atom array will be detected. In an X-ray measurement, an X-ray beam strikes the surface of a crystal to produce scattered beams. The strengths and angles of the scattered beams are recorded as the crystal is gradually rotated. By analyzing the signals of reacted beams, the mean chemical bond lengths and angles can be determined. Bruker D8 Discover X-ray diffractometer was used with a LYNXEYE-XE detector using CuK α 1 radiation ($\lambda = 1.5418 \text{ \AA}$) and Bragg-Brenato $\theta:2\theta$ geometry. The data collection was carried out at room temperature, between 10° and 80° with a step of 0.02° and dwell time of 1.2 sec per step. In all cases the EVA software provided by Bruker is used to determine the compositional changes in the studied materials.



Figure 3.5 The Bruker XRD (left) and high temperature stage (right)

3.4 Molecular Simulations

Molecular dynamics (MD) is a computer simulation method based on Newtonian classical mechanics. The interaction and motion between microscopic particles in a multibody system composed of nuclei and electrons is simulated by a computer. The physics of each nucleus are modeled according to Newton's 3rd law, with the forces described with an empirical potential field formed by all other nuclei and electrons. Through this process the trajectories of the particles in the system are obtained, and local structural and macroscopic properties can then be calculated through statistical mechanics methods.

MD simulations are a very effective computational method that has been widely used in many disciplines to obtain information regarding the behavior of atoms in the

nanoscale, where experimental measurements are difficult costly or impossible to perform. Thermal energy can be stored in materials because of their internal energy based on the electronic structure of the basic particles like atoms, molecules, clusters or just the “unit cell”. The knowledge of the thermodynamic properties and the dynamical behavior of all the materials involved in a process is the basis for the design of a storage device. In the developing process of a heat storage device experiments play a dominant role because in the prototype stage a physical system has to be built to acquire measurement data for a fine tuning of the pilot and end-market product. In this development process numerical modelling plays the role of reducing the number of time consuming and cost intensive experiments. In later stages models can help to understand and optimize the material behavior and the dynamic behavior of compact TES systems and components based on Phase Change Materials (PCM's) and Thermo Chemical Materials. Ultimately, these molecular models could help to find ways to optimize the materials in combination with their system level applications. In the past decade, the MD simulations have seen a remarkable increase. From 10000 number of manuscripts submitted in 2005 containing work in MD, in 2020 the number is well above 40000 ¹¹⁷.

3.4.1 Theory

3.4.1.1 Law of classical mechanics

As a deterministic method, molecular dynamics is used to calculate the equilibrium and transfer properties of particles in a multibody system. Particles in the system comply with Newton's classical laws of mechanics:

$$F_i(t) = m_i a_i(t) \quad (3.1)$$

in the formula, F is the force exerted on the particle, m is the mass of the particle, and a is the acceleration of the particle. The force F on particle i can be directly used as the first derivative of the potential function with respect to the coordinate, i.e.

$$F_i(t) = -\frac{\partial U}{\partial r_i} \quad (3.2)$$

in the formula, U is a potential function. Therefore, for each particle:

$$m_i \frac{\partial v_i}{\partial t} = F = -\frac{\partial U}{\partial r_i} + \dots \quad (3.3)$$

where v is the velocity vector and m is the particle mass.

3.4.1.2 Basic principle and calculation flow

In the motion system of N molecules or atoms, the energy of the system is the sum of the kinetic energy and potential energy of all molecules or atoms in the system. Generally, the potential energy consists of two parts: the non-bonded van der Waals interaction between molecules or atoms and the internal potential of the molecule¹¹⁸:

$$U = U_{VDW} + U_{int} \quad (3.4)$$

The van der Waals interaction can be approximated as the sum of the van der Waals interactions among all the atoms in the system:

$$U_{VDW} = u_{12} + u_{13} + \dots + u_{1n} + u_{23} + u_{24} + \dots + u_{2n} = \sum_{i=1}^{n-1} \sum_{j=i+1}^n u_{ij}(r_{ij}) \quad (3.5)$$

where, r is the distance between atom i and atom j . According to classical mechanics, the force exerted by any atom i in the system is the gradient of potential energy:

$$\mathbf{F}_i = -\nabla_i U = -\left(\mathbf{i} \frac{\partial}{\partial x_i} + \mathbf{j} \frac{\partial}{\partial y_i} + \mathbf{k} \frac{\partial}{\partial z_i}\right) U \quad (3.6)$$

The acceleration of an i atom can be then obtained from Newton's law:

$$\mathbf{a}_i = \frac{\mathbf{F}_i}{m_i} \quad (3.7)$$

in the formula, F is the force exerted on the particle, m is the mass of the particle, and a is the acceleration of the particle.

Integrating Newton's law of motion equation with time can predict the velocity and position of i atom after the passage of time t .

$$\frac{d^2}{dt^2} \mathbf{r}_i = \frac{d}{dt} \mathbf{v}_i = \mathbf{a}_i \quad (3.8)$$

$$\mathbf{v}_i = \mathbf{v}_i^0 + \mathbf{a}_i t \quad (3.9)$$

$$\mathbf{r}_i = \mathbf{r}_i^0 + \mathbf{v}_i^0 t + \frac{1}{2} \mathbf{a}_i t^2 \quad (3.10)$$

where, r and v respectively represent the position and velocity of the particle, and superscript "0" represents the initial state value for each integration.

The calculation process of molecular dynamics is summarized as follows: first, according to the positions of each molecule in the system, the potential energy of each atom is calculated by equation (3.8), then through equation (3.9) the force and acceleration of each atom is computed, and then with equation (3.10) the position and velocity of each atom after the Δt time is obtained. These steps are repeated for each Δt , where Δt the timestep of the simulation. After repeated cycles, desired parameters such as position, velocity, and acceleration of atoms in the system at different times scales can be obtained.

3.4.1.3 Potential Function

The potential function describes the interaction between atoms in an MD simulation. In physics and engineering this is commonly referred to as the interatomic potential. It is essentially the core of a every MD study. The accurate selection of a potential function is crucial to the accuracy of molecular dynamics calculation results. Potential functions have different forms for different systems, different substances in difference phases and for different simulation purposes. Most commonly used classical potential functions are described below.

3.4.1.4 The pair potential

In the early stages of MD simulations, the pair potential model was most frequently used. The pair potential does not only provide a satisfactory description of the behavior of various inorganic compounds, but it does so through the interaction of only two atoms, in a pairwise manner. When calculating the interaction forces between the

two particles, the rest of the particles are not considered. The most common pair potentials are as follows:

(1) Lennard-Jones(L-J) potential

$$U_{ij}(r) = \frac{A_{ij}}{r^n} - \frac{B_{ij}}{r^6} \quad (3.11)$$

Generally, if n is between 9 and 15, the first fraction in the interaction corresponds to the polarization effect, which is assigned a value based on the perturbation theory of quantum mechanics. The coefficients A and B are constants determined by the lattice structure and the sublimation enthalpy (transitional enthalpy) of the material. Typically, for gas and liquid molecules, the above equation can be rewritten as:

$$U_{ij}(r) = 4\epsilon_{ij} \left[\left(\frac{\sigma_{ij}}{r} \right)^{12} - \left(\frac{\sigma_{ij}}{r} \right)^6 \right] \quad (3.12)$$

where ϵ , a parameter indicating the strength of a force; and σ , a parameter indicating the size of the atom.

The L-J potential function expresses the effect of the van der Waals force between the molecules. The potential is the sum of the repulsion energy and the absorbing energy. The attractive (absorbing) energy is assumed to decay and is thus subtracted in the form of the inverse of the sixth power, while the repulsion decays even more rapidly and thus is described with the twelfth power. When the distance between two atoms is less than σ , the net force is repulsive. When it is larger than σ , it is characterized as

attractive. At σ the atoms are at the bottom of the potential well ϵ and the attractive and repulsive forces between them are balanced. The parameters of the L-J potential function can be derived from experimental data of various physical properties, for solids most frequently through the lattice structure. This equation can also be used to describe the body centered cubic transition group of metals, such as chromium, molybdenum, tungsten, etc. At the same time, for many molecular crystals, due to the influence of hydrogen bonds, corrections need to be made when describing the interaction force between them.

(2) Born - Mayer potential

The Born-Mayer potential is mainly used in simulations of ionic crystals. It is assumed that there are long-range coulomb forces and short-range repulsive forces between ions, so the potential is:

$$U_{ij}(r_{ij}) = \frac{1}{2} \frac{Z_i Z_j}{r_{ij}} + \phi(r_{ij}) \quad (3.13)$$

where, the first term is the long-range coulomb potential, Z is the charge number of the ion, and r is the distance between the ions.

The second term is the short-range repulsion potential, which can be written as:

$$\phi(r_{ij}) = A_{ij} \exp\left(-\frac{r_{ij}}{\rho}\right) - \frac{C}{r_{ij}^n} \quad (3.14)$$

in the formula, A , ρ and C are determined typically by experimental value fitting.

The above is commonly known as Buckingham pair potential.

(3) Morse potential

$$U_{ij}(r_{ij}) = A \left[\ell^{-2\alpha(r_{ij}-r_0)} - 2\ell^{-\alpha(r_{ij}-r_0)} \right] \quad (3.15)$$

Where, α is the nuclear spacing (distance between two atoms or bond length); r_0 is the equilibrium bond length; A is the depth of the pseudo-potential well of the Morse potential, and the zero point of potential energy can be selected as required, the potential energy of the system when the distance between two cores approaches infinity can be set to zero. The parameter α controls the "width" of the potential.

3.4.1.5 Ensemble

The Ensemble is a concept of statistical mechanics. The framework of statistical mechanics is based on three basic assumptions ¹¹⁸. (1) Certain macroscopic states correspond to a large number of microscopic states, which appear at a certain probability. (2) The macroscopic mechanical quantity is the statistical average of the corresponding microscopic quantity of each microscopic state; (3) The probability of each microstate in the isolated system appears equally. An ensemble is essentially a collection of all possible systems which have different microscopic states but have an identical macroscopic or thermodynamic state.

Based on this theory, Gibbs developed a complete and universal theory of equilibrium statistical mechanics in 1902¹¹⁹. The core was to put forward the concept and theory of ensemble. The Ensemble is a huge system composed of almost identical systems with exactly the same composition, nature, size and shape. It is a collection of a large number of systems, in which each system is in a certain microscopic state of motion independently.

Molecular dynamics simulation must be carried out under certain ensemble. The main ensembles include microcanonical ensemble (NVE), canonical ensemble (NVT), isothermal isobaric ensemble (NPT) and isenthalpic isobaric ensemble (NPH).

3.4.1.6 The Numerical Algorithm

In molecular dynamics Newton's equations of motion for a multi-particle system are solved by finite difference method, numerically. This is a computationally expensive process, as the force acting on the atom is required to be calculated. An optimized calculation method to obtain the value of the atomic force is critical.

3.4.1.7 Boundary Conditions

In MD simulations, the requirement to encompass a number of statistics in a number of molecules must be met to more accurately reflect the macroscopic properties of a system. In principle, the more molecules, the better. But given the speed and computational limitation of computers, the number of simulated molecules is unlikely to be large enough. Therefore, reducing the influence of the finite number of molecules on the simulation results is very important. Theoretically speaking, the motion state of molecules in the system satisfies the ergodic principle of each state, so the deficiency

of space and number of molecules can be made up by extending the statistical time. The scale effect caused by the insufficient number of molecules can also be compensated by selecting appropriate boundary conditions. In MD simulations, the selection of boundary conditions needs to satisfy two aspects. First, in order to reduce the amount of computation, the simulated element should be as small as possible, and the simulated simulation geometry should be large enough to exclude any possible dynamic disturbance that may affect the results. Secondly, physical coupling problems such as volume change, strain compatibility and environmental stress balance should be addressed. There are two three type of boundary conditions most commonly used in simulations. The first one is a periodic condition. In this case atoms interact across the boundary and when arriving at the edge of the box they can exit and re-enter on the other end retaining their velocity. The second type of boundary is fixed. In fixed boundaries atoms are deleted when crossing the edge of the box. The third boundary style is shrink-wrapped. In this case when atoms reach the edge of the box, the respective edge is extended to encompass them. In practice most simulations use periodic boundary conditions. When dealing with some specific problems like flow in nano-channels fixed boundaries can be used. Shrink-wrapped boundaries are used primarily in deformation problems.

3.4.2 Extracting Variables

After calculating the motion trajectories of atoms in the simulation system, the macroscopic and structural characteristics of the system can be obtained. The basic method is through the equilibration of the system, which involves averaging of long-time statistics. For non-equilibrium states, it is a series of short time statistics.

In molecular dynamics, the structural analysis of the simulated configuration is very important. For example, when studying the melting or solidification of a metal, it is necessary to analyze its structural changes in time. For structural analysis, radial distribution function, static structure factor, local crystal sequence analysis (using common neighbor analysis, or pair analysis) and coordination number are commonly used. Finally, the calculation and prediction of macroscopic properties is possible through MD simulations. In the case of TES this refers to primarily the transport properties of the material and secondarily to more application specific properties like the surface tension or the thermal expansion coefficient of a material, like an encapsulated PCM.

Computational methodologies to extract local structural and transport properties of a material are described below.

3.4.2.1 Radial Distribution Function (RDF)

Radial distribution function is the most frequently quoted method to describe the local structure of a system, particularly for liquids. It is an indicator of the degree of disorder/order of the structure. The radial distribution function $g(r)$ is the probability of finding another atom at a distance of r ,

$$g(r) = \frac{n(r)}{4\pi r^2 \rho_0 \delta r} \quad (3.16)$$

Where, $n(r)$ is the number of particles in the shell with radius r to $r+\Delta r$; ρ_0 is the particle density of the crystal.

The radial distribution function can be understood as the ratio of the regional density to the average density of the simulated system. When the value of r is small, the atom is very close to the reference molecule, and the density of the region is different from the average density. When the value is large, it is far away from the reference molecule. Long distance r usually translates to a regional density equal to the average density of the system, and a radial distribution function value close to 1.

3.4.2.2 Static Structure Factor (SSF)

Static structure factor is one of the physical quantities to judge the disorder of structure.

Its expression is:

$$S(K) = \frac{1}{N} \left| \sum_{j=1}^N \exp(iK \cdot r_j) \right| \quad (3.17)$$

N is the total number of atoms, K is the inverted lattice vector, and r_j is the position vector of atoms. The static structure factor is 1 for an ideal crystal and 0 for an ideal fluid.

3.4.2.3 Coordination Number (CN)

The coordination number is the number of atoms in the first nearest neighbor of an atom. It shows the density of the atoms around the atom. To some extent, the number of coordination number can also reflect the density of the region around the atom. It is often used as an auxiliary means of structural analysis in some analyses. Its definition is:

$$n=4\pi\rho_i\int g_{ij}(r)r^2 dr \quad (3.18)$$

Where, the upper and lower limits of the integral are determined by the radial distribution function.

3.4.2.4 Angular Distribution Function (ADF)

Similar to the radial distribution function, but for angles the angular distribution function (ADF) is a secondary structural property used to assess the structure of a system. The ADF is built around the fact that every combination of three atoms forms a triangle with three bond angles. Therefore, the job of the ADF is to step through every combination of three atoms in a given system, determine the bond angles, and add those bond angles to a bin counter which represents some appropriate increment of 180 degrees of arc (such as one degree). After all bond angles are determined, each bin can be divided by the total number of bond angles so that each bin represents the probability that the bond angle between any three atoms will fall within that given increment of arc. This property is important when validating the structure of a material in simulations, where no intramolecular (i.e. bonds, angles etc.) constraints are used or in cases where the evolution of the structure under pressure or temperature is to be studied.

3.4.2.5 Diffusion Coefficient

Diffusion is the process whereby an initially nonuniform concentration profile (e.g., an ink drop in water) is smoothed in the absence of flow (no stirring). Diffusion is caused by the molecular motion of the particles in the fluid. In molecular dynamics simulation,

the diffusion coefficient D can be calculated by two methods, namely Einstein method and Green-kubo method. The Einstein method obtains the diffusion coefficient by finding the slope of mean azimuth shift,

$$D_i = \frac{1}{6} \lim_{t \rightarrow \infty} \frac{d}{dt} |r_i(t) - r_i(0)|^2 \quad (3.19)$$

The green-kubo method uses the integral of velocity autocorrelation function VACF to obtain the diffusion coefficient, namely:

$$D_i = \frac{k_B T}{m} \int_0^\infty v_{ACF}(T) dt \quad (3.20)$$

Where, D_i represents the diffusion coefficient of particle i , k_B the Boltzmann constant, m the particle mass, $r_i(t)$ and $r_i(0)$ represent the position vector of particle i at time t and time 0 respectively.

Such a relation between a transport coefficient and an integral over a time-correlation function is called a Green-Kubo relation. This relation is used to calculate other transport properties such as the viscosity and the thermal conductivity.

Attention should be given in cases where boundaries of the simulations are periodic. Studies have shown that hydrodynamic interactions in a simulation with periodic boundary conditions lead to changes in the diffusion coefficient due to finite size effects¹²⁰. Theoretical studies have calculated that in a cubic periodic box simulation,

the value of the self-diffusion in an infinite liquid can be obtained using the following formula:

$$D = D_{PBC} + 2.837 \frac{k_B T}{6\pi\eta L} \quad (3.21)$$

where D_{PBC} is the self-diffusion coefficient obtained from the simulation, k_B is the Boltzmann constant, T is the temperature, and η is the viscosity of the liquid and L the length of the side of a cubic simulation box.

3.4.2.6 Thermal Conductivity

The thermal conductivity is calculated as the time integral of the heat auto correlation function J in a given direction by means of

$$k = \frac{1}{3Vk_B T} \int_0^\infty \langle J(0)J(t) \rangle dt \quad (3.22)$$

where V is the volume, k_B the Boltzmann constant, T the temperature and $\langle \dots \rangle$ the ensemble averaging. J is the vector denoting the heat flux and is defined as

$$J = \sum_i e_i v_i + \sum_i \sum_{j \neq i} (F_{ij} v_i) r_{ij} \quad (3.23)$$

where e_i is the total energy, v_i the velocity of particle i , and F_{ij} the force on atom i exerted by neighbor atom j .

For the calculation of the thermal conductivity, the system should be equilibrated in the NVT ensemble at the desired temperature. After the system has reached equilibration, heat flux vector values are averaged for extended time in order to calculate the value of the thermal conductivity.

The Green-Kubo formalism is the most straightforward method to obtain the value of a transport property in a system. Alternative methods are related to the Muller-Plathe formalism and involve non-equilibrium dynamics.

3.4.2.7 Viscosity

Shear viscosity is calculated similarly to the thermal conductivity using an analogous Green-Kubo formalism involving the stress tensor in place of the heat flux vector:

$$\eta = \frac{V}{k_B T} \int_0^{\infty} \langle P_{xy}(0) P_{xy}(t) \rangle dt \quad (3.24)$$

where, V is the volume of the system, k_B the Boltzmann constant, T the temperature, and P_{xy} are the off-diagonal components of the stress tensor.

For the calculation of the viscosity, the system is first equilibrated in the NVE ensemble in the presence of a Langevin barostat. After equilibration, the barostat is turned off and stress tensor values are averaged for a long time in order to calculate the shear viscosity.

3.4.2.8 Specific Heat Capacity

The quantity of heat required to raise the temperature of a substance by 1 °C is defined as heat capacity; Specifically, for 1 g of a substance, it is called specific heat capacity or specific heat. (The adjective specific means "per unit mass"). In MD simulations the specific heat capacity is obtained from the fluctuations in the total energy of the system. Attention must be given to distinguish between properly defined mechanical quantities such as the energy or Hamiltonian \mathcal{H} , the kinetic temperature T or the instantaneous pressure \mathcal{P} , and thermodynamic concepts such as T and P , which can only be described as ensemble averages or as parameters defining an ensemble. Fluctuations are readily computed in the canonical ensemble. As just mentioned, the specific heat is given by the fluctuations in the energy:

$$C_v = \frac{\langle \delta E^2 \rangle_{NVT}}{k_B T^2} \quad (3.25)$$

where

$$\langle \delta E^2 \rangle = \langle E^2 \rangle - \langle E \rangle^2 \quad (3.26)$$

where E the total energy of the system, k_B the Boltzmann constant, T the temperature of the system.

Another method to obtain the specific heat capacity is directly from the definition of the property.

$$C_p = \left(\frac{\partial H}{\partial T} \right)_{NPT} = \frac{\Delta H}{\Delta T} \Leftrightarrow \Delta T = C_p \Delta H \quad (3.27)$$

Where H the enthalpy of the system.

From the above formula, it is clear that the specific heat capacity at constant pressure can be obtained from the slope of the plot of the temperature versus the enthalpy. This plot can be obtained by running two separate simulations at two different temperatures and then obtaining the equilibrated value of the enthalpy. Naturally a higher number of points can provide a more satisfactory accuracy.

3.4.2.9 Thermal Expansion Coefficient and Isothermal Compressibility

The coefficient of linear thermal expansion is a material property that is indicative of the extent to which a material expands upon heating. Different substances expand by different amounts. In a molecular level this translates to the change in volume of a material at different temperatures. It is defined by the following formula:

$$\alpha_V = V^{-1} \left(\frac{\partial V}{\partial T} \right) = \frac{1}{V} \left(\frac{\Delta V}{\Delta T} \right)_{NPT} \quad (3.28)$$

where V the initial volume of the system and ΔV and ΔT the deviations in volume and temperature respectively. The P subscript denoted a constant pressure ensemble.

In a similar sequence to the specific heat capacity the equilibrated volume of the system is obtained at different temperature points. From the slope of the plot of temperature versus volume the thermal expansion coefficient can be obtained.

In thermodynamics and fluid mechanics, compressibility (also known as the coefficient of compressibility or isothermal compressibility) is a measure of the relative volume change of a fluid or solid as a response to a pressure (or mean stress) change. Is it obtained from the following formula:

$$\beta_T = -V^{-1} \left(\frac{\partial V}{\partial P} \right) = -\frac{1}{V} \left(\frac{\Delta V}{\Delta P} \right)_{NVT} \quad (3.29)$$

where V the initial volume of the system and ΔV and ΔT the deviations in volume and temperature respectively. The P subscript denoted a constant pressure ensemble.

The compressibility can be obtained in an analogous method to the specific heat capacity and thermal expansion coefficient. However, due to the high fluctuations of pressure in MD simulations longer equilibration times are necessary to obtain the final value.

3.4.2.10 Surface Tension

Surface tension is calculated using the center of mass definition otherwise known as the Kirkwood-Buff formulation. The z dimension of the equilibrated simulation box is doubled, to avoid issues related to periodicity. Then the system is equilibrated in the

NVT followed by a sampling for in the NVE ensemble during which the pressure tensor data is averaged calculated. The surface tension is obtained by:

$$\gamma = \frac{1}{2}L_z \langle P_{zz} - \frac{1}{2}(P_{xx} + P_{yy}) \rangle \quad (3.30)$$

where, L_z is the total length of atoms in the z direction and $P_{xx,yy,zz}$ are the diagonal elements of the pressure tensor.

3.4.2.11 Software used

LAMMPS¹²¹ is the most widely used software for studies on inorganic molecules. It is composed of a classical molecular dynamics code and is mainly used in the calculation and simulation of physical materials. It can simulate and calculate the ensemble of particles, solids and gases. It can simulate the behavior of a group of atoms, polymers and other organic compounds, metallic and inorganic compounds, as well as granular and coarse-grained system. LAMMPS can handle systems that range from a few particles to millions or even hundreds of millions of particles. To formulate the initial topology of a system and visualize the trajectory results VMD (Visual Molecular Dynamics)¹²² is used.

Chapter 4 EXPERIMENTAL RESULTS

In this section the CA of various molten salts on various surfaces and under various atmospheric conditions is investigated. Furthermore, the addition of nanosuspensions of different size geometry and concentration is also examined.

4.1 Effect of Nanoparticle addition on the Wetting and Rheological Properties of Solar Salt-SiO₂

As discussed in chapter 2, the addition of NPs enhances the thermal properties of the salts, but also affects their wetting and rheological behavior. This influences the handling and operational costs of CSP plants. The essential properties describing the wetting and rheology of a material are its CA and viscosity, respectively. For this reason, in this section a series of measurements are presented on the CA and viscosity of the Solar Salt and its individual component salts with various concentrations of amorphous SiO₂ NPs.

4.1.1 Contact Angle Results

A series of CA measurements of SS with 0 wt.%, 0.5 wt.%, 1.0 wt.%, 1.5 wt.% and 2.5 wt.% amorphous SiO₂ on an Al₂O₃ substrate are performed. In the case of the base salt the CA is linearly reduced with respect to temperature increase, up to complete wetting at 390°C. This is an expected behavior and in agreement with the literature⁶³. In Figure 4.1 it can be seen that the addition of a very small amount of NPs has a significant effect on the wetting process. Specifically, instead of a linear reduction with temperature, a plateau is observed in the value of the CA, which remains stable at 118±8.0° up to a temperature of 300 °C, where a steep reduction is observed. A higher load of NPs shifts this effect to elevated temperatures, up to 320 °C in the case of a 2.5 wt. % loading.

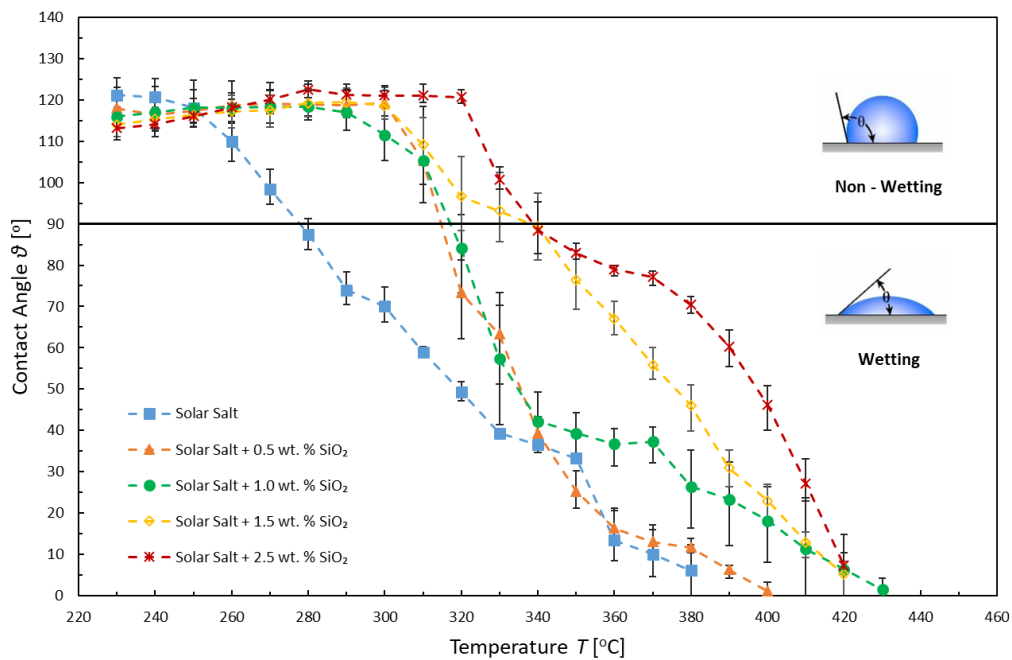


Figure 4.1 CA measurements of SS (Solar Salt) with 0 wt.%, 0.5 wt.%, 1.0 wt.%, 1.5 wt.% and 2.5 wt.% of SiO₂ on an Al₂O₃ substrate.

A liquid is considered to have high wettability when the $CA < 90^\circ$, if the $CA > 90^\circ$ then its wettability is characterized as low. Addition of NPs shifts the point of transition from high to low wettability to elevated temperatures. Without NPs the SS transitions from low to high wettability at 290°C . By adding NPs the transition point is shifted to 300°C and at higher loadings at 350°C . This can be better understood from the images presented in Figure 4.2. In the 1st row the CA of the molten salt at 250°C is in all higher than 90° (poor wettability). However, at 310°C the CA of the base and the 1 wt.% SiO_2 case is reduced to values lower than 90° . The 2.5 wt.% loading, though, is still not wetting the surface. At 350°C all 3 materials have transitioned to a high wettability condition, spreading over the Al_2O_3 substrate. In other words, at sufficiently high temperatures ($T > 350^\circ\text{C}$), these differences in wetting behavior are reduced and all the NP suspensions tested have a linearly decreasing contact angle with temperature regardless of the NP concentration.

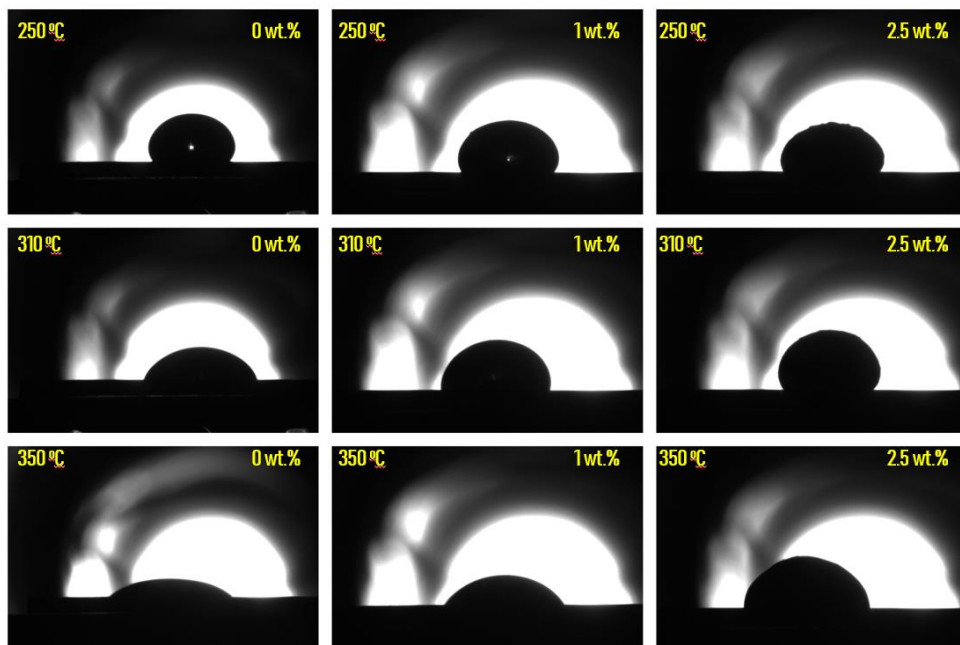


Figure 4.2 CA snapshots of solar salt with 0 wt.%, 1.0 wt.% and 2.5 wt.% of SiO_2 on an Al_2O_3 substrate at 250°C , 310°C and 350°C .

To further investigate the effect NPs on the molten salt, CA studies are also performed on the two salt components of the binary mixture independently. Unlike the case of the SS, no significant difference is observed in the case of the NaNO_3 and KNO_3 , both of which with the addition of 1% NPs retain a trend similar to their base case (Figure 4.3).

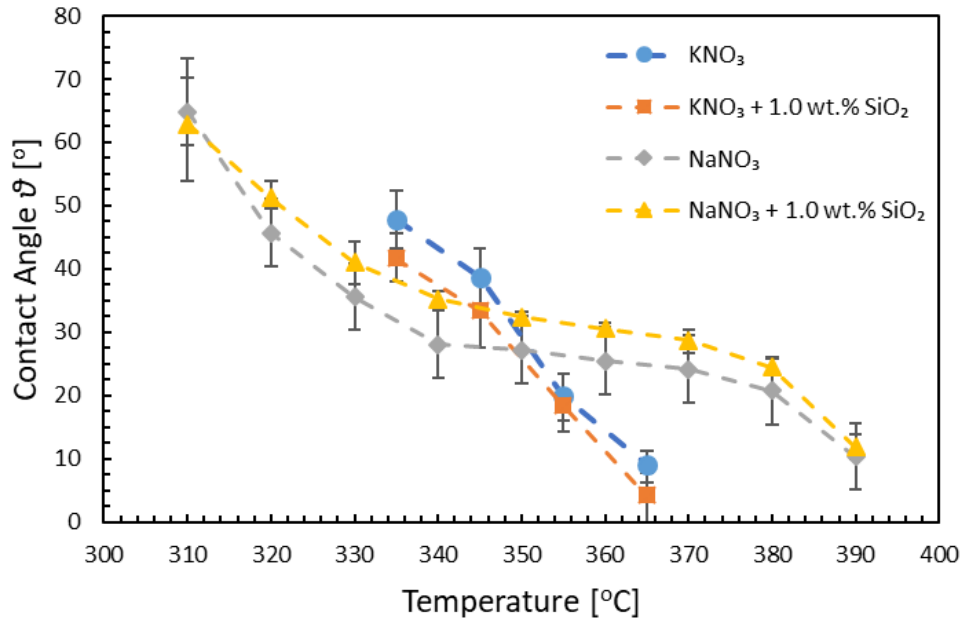


Figure 4.3 CA measurements of NaNO_3 and KNO_3 with 0 wt.% and 1.0 wt.% of SiO_2 on an Al_2O_3 substrate.

4.1.2 Viscosity results

In the search of an explanation for the contact angle data presented above and aiming to provide a better understanding of the effect of NPs, the authors performed viscosity experiments for SS and its two components independently, with and without NPs. The goal is to correlate the anomalous effect observed in the case of the CA with the rheological behavior of the salt in the same temperature range. To that end, the viscosity is acquired in a 25 °C increment in the same temperature range as the CA

measurements. The temperature dependence of the viscosity of solar salt nanofluids has been investigated experimentally at 100 s^{-1} , a shear rate used for pumping in CSP systems. Previous experimental studies have shown that temperature can have a very strong effect on the nanofluids viscosity, which is similar to the trend observed in our results (see Figure 4.4).

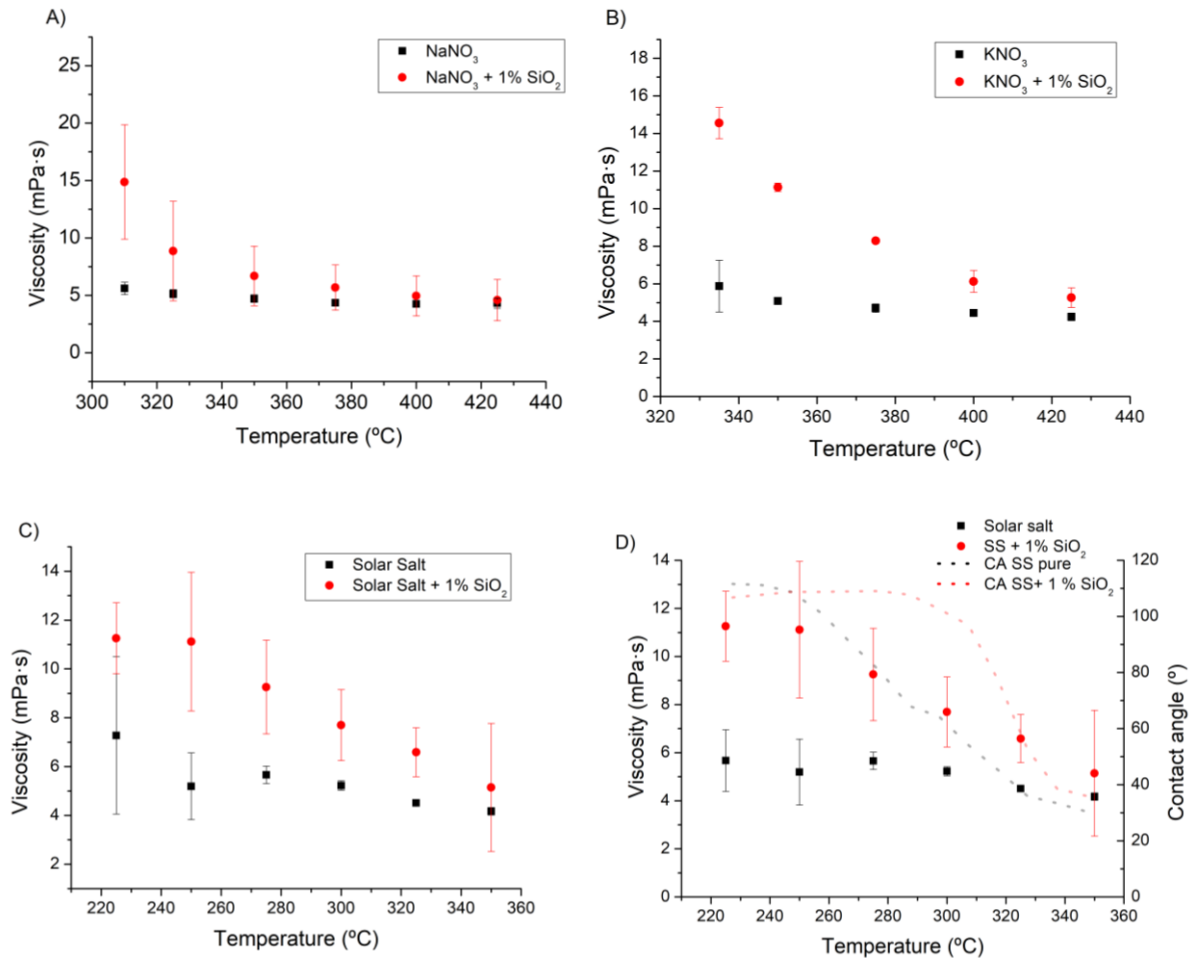


Figure 4.4 Dynamic viscosity data at 100 s^{-1} for sodium nitrate (A), potassium nitrate (B), Solar Salt (C) and their nanofluids compositions. Viscosity vs contact angle data for Solar Salt and Solar Salt nanofluid (D).

As previously reported in the literature ^{20,123,124}, the viscosity of the nanofluids with 1% of silica increases when comparing to the base fluid. The rheological behavior is similar from the viscosity temperature increment perspective, in all the cases. NaNO₃ ^{125,126}

and KNO_3 ^{29,127,128} show similar viscosity around 5 mPa·s at the temperature range analysed. The SS mixture shows a viscosity also near that value (6 mPa·s) which is in good agreement with the literature ^{29,129}.

4.1.3 Discussion

The CA measurements suggest that when NPs are added to the SS, the non-wetting behavior from the semi-solid (“mushy”) region of the salt mixture is extended to higher temperatures than expected, increasing with particle concentrations. In other words, the salt mixture with NPs is behaving like a solid-liquid mixture for higher temperatures than anticipated. When the individual salt components were tested with and without NPs (Figure 4.2), this behavior was not observed; suggesting it is related to the binary salt mixture itself and not to the particularities of NaNO_3 or KNO_3 .

The SS composition is an off-eutectic system consisting of NaNO_3 and KNO_3 (60 wt. % or 64% mol of NaNO_3). Eutectic systems are homogenous mixtures of substances that melt at a specific temperature lower than the melting point of each of the individual components¹³⁰. However, off-eutectic systems melt over a temperature range, identified as the “mushy region”, in which liquid and solid phases coexist. This region is dependent on the temperature and composition of the mixture. In the NaNO_3 - KNO_3 system, 49 %mol of NaNO_3 corresponds to the eutectic point and melts at 223 °C. However, the SS starts melting at approximately 223 °C and is not fully liquid until somewhere around 240-260 °C, depending on the phase diagram reference (Figure 4.5). As the material reaches its melting point, the lattice structure of one of its components, typically the one with the lowest melting point (in our case NaNO_3 with a melting point of 308 °C) will start to phase change into a liquid (see Figure 4.5). For

the system to completely phase transition into a liquid, the lattice of the second component (KNO_3) is required to phase change. For that more energy is required.

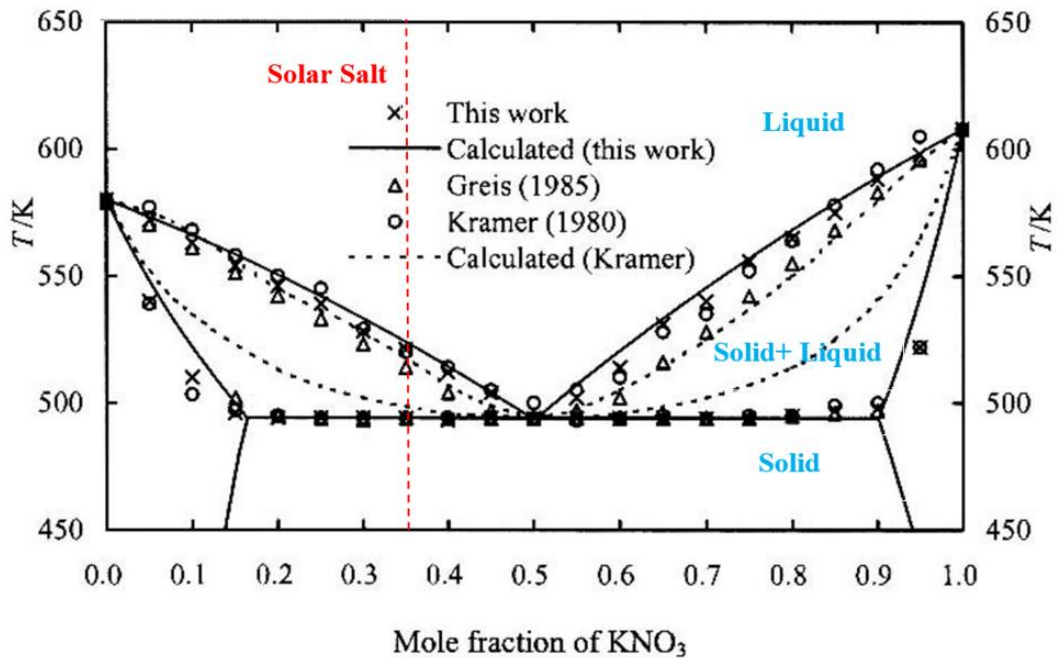


Figure 4.5 The phase diagram for the NaNO_3 - KNO_3 system ¹³¹ showing solar salt composition (36%mol KNO_3).

This is further verified in the case of the NaNO_3 - KNO_3 mixture. Previous studies have concluded, that when the ionic radius between the two materials constituting a eutectic are larger than roughly 15%, a phase separation is likely to occur during the melting process. In case of this mixture the ion radius of Na^+ and K^+ are 95 and 133pm respectively. Therefore, during phase separation the NaNO_3 , with the lowest melting point, phase changes, while the KNO_3 initially retains its lattice structure and subsequently phase changes as well, at higher temperature levels.

Zhang et al, conducted XRD studies to determine the crystalline phases of the NaNO_3 - KNO_3 mixture at its melting point ¹³¹. They observed that while in a solid mixture one

would expect only two clear distinct lattice structures, those of the two independent components. However, during the melting process several crystalline structures are identified. This is due to the fact that in NaNO₃-rich parts of the mixture, the larger potassium ions alter the lattice structure of the base crystal and prevent its phase transition. The same is true for the KNO₃-rich solutions. In the NaNO₃-rich case the structure was expanded, while for the KNO₃-rich the opposite occurred.

The fact that crystalline structures of one component exist within the other and a phase transition region exists is also verified in this study by differential scanning calorimetry (DSC). In Figure 4.6a, a DSC curve of the SS with a very slow heating rate (5 °C /min) is observed. The melting of the solar salt onsets at 219 °C, with the endset at 241 °C, which as expected proves that complete phase transition does not occur at the melting point, but gradually in a temperature range of 22 °C. In this range, solid and liquid phases coexist.

Furthermore, previous studies have shown that addition of NPs has shown to affect the phase transition of the molten salt, the onset, endset and melting point of which, are all shifted ¹³². DSC measurements conducted on solar salt (Figure 4.6) show that in the presence of 5.0 wt.% SiO₂ the phase transition curve is wider, compared to the base case, with an onset at 201 °C and an endset at 250 °C both shifted further than the base case. On the contrary addition of 5.0 wt.% SiO₂ in the individual component salts, does not produce the same effect. Both the base and 5.0 wt.% silica cases show the same phase transition behavior. It can be seen that increase of the NP concentration also affects the phase transition of the SS. The double peaks that are visible in the base case, due to difference in ionic radius between Na⁺ and K⁺ as

explained above, are more pronounced with increasing NP concentration. Naturally, the phase transition is heat dependent, but the point of the DSC measurements is to compare the behavior of the mixture and individual components with and without the presence of silica.

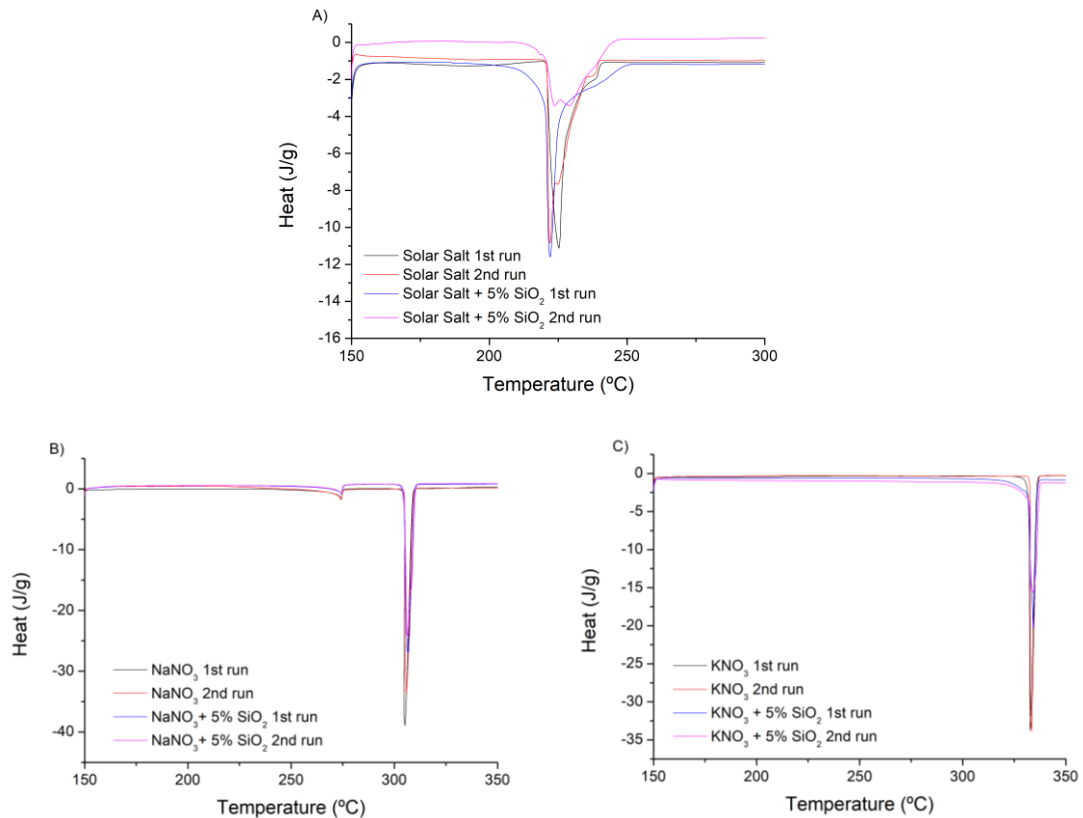


Figure 4.6 Heat flow versus temperature for a) Solar Salt 0 and 5.0% w.t SiO₂, b) NaNO₃ 0 and 5.0% w.t SiO₂, c) KNO₃ 0 and 5.0% w.t SiO₂.

DSC measurements are in agreement with the viscosity results. The later show a steep reduction in the measured values around 250 °C, when the salt mixture without NPs is expected to be fully liquid. Measurements below this temperature are expected to be in the “mushy region” and therefore correspond to solid-liquid mixtures. Looking at the contact angle measurements in Figure 4.1, results suggest that the mushy region

measurements for neat solar salt (no NPs) for temperatures below 250°C correspond to a plateau in CA. When nanoparticles are added, this plateau seems to be extended to higher temperatures, up to 300-320°C depending on the NP concentration.

Since, the nanofluid phase transition can be extended from 240 up to 250 °C with the addition of large concentrations of NPs, the observed trend in the viscosity can be attributed to the existence of an extended mushy region, inside the molten liquid, due to the addition of the NPs. Further research is required to better understand this extended mushy region into higher temperatures. A possible explanation could be that NP are locally segregating the salt components, veering towards NaNO₃-rich regions which would stay solid for a wider and higher temperature range.

Another suggested reason behind the change in the CA might be related to previous reports of reaction between the molten NaNO₃ and silica at 300 °C¹³³. In their work Wei et al¹³³, calculated the thermodynamic reactions between Na/KNO₃ and SiO₂ and identified a solubility of Na⁺ in SiO₂ from 300 °C. They related this to NO_x emissions that were measured from molten eutectic salt heated from 300 to 600°C in a silica boat. However, they could not identify the formation of sodium silicate, the product of the reaction that was suggested to occur. This was attributed to the low time the salt was present in molten state as well as the existence of this layer being lower than the threshold of accuracy of the XRD. In a more recent study by Liu et al¹³⁴ a reaction between the molten nitrate eutectic and SiO₂ NPs was reported by XRD (Figure 4.7). The authors reported the existence of a sodium silicate peak at 21°, which was related to the reaction between molten sodium nitrate and silica.

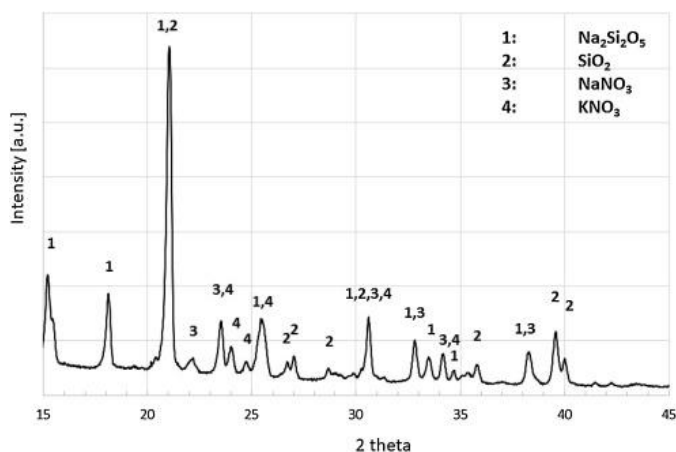


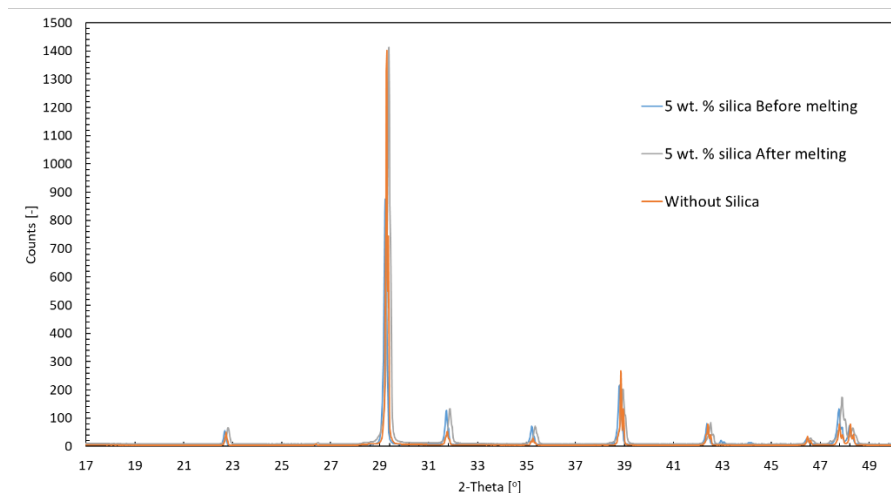
Figure 4.7 XRD data of Solar salt with 5.0% α -SiO₂ NPs after melting at 390 °C for 24h. (Hu et al. ¹³⁵)

To identify if this reaction is occurring the NaNO₃ and KNO₃ with 5.0 wt.% α -SiO₂ NPs are melted for 16h at 390 °C in borosilicate non-reacting beakers. The samples are then tested in the XRD with a step of 0.2 and acquisition time of 1.2 sec. The structure before and after melting as well as the structure without the presence of NPs is compared. No sodium silicate peak is present at 21° in either of the two salts. Furthermore, there is no significant difference in the structure of the salt is observed before and after melting. Finally, no significant difference is also observed between the base case and in the presence of NPs at room temperature. It can thus be concluded that no reaction is occurring between the molten nitrate salt and the amorphous silica, at least in a time frame of 16h and thus the experimental duration of the CA measurements, which as described in section 2.1 is 80min. This is in agreement with the work of Hu et al¹³⁵ in which the work a comparison of the XRD peaks of nanofluid containing solar salt and amorphous silica before and after thermal cycles are presented with minimal differences before and after the cycling process. The peak observed in the study of Liu et al (Figure 4.8), is thus hypothesized to be due to the type of NPs used, which in their case are not mentioned to be crystalline but are

suggested to be, as in this work the NPs are amorphous and thus not visible in the XRD study.

Originally, pellets, for the CA measurements, are compressed at 50MPa (sec. 3.2.1). A sensitivity analysis is conducted on the effect of the compression rate on the evolution of the CA. Measurements are conducted with pellets compressed at 20MPa and 120MPa respectively.

Density measurements show that pellets compressed at lower rates have a larger volume of pores, while the opposite is true for higher compression rates (see Figure 4.9 (a)). Furthermore, pellets containing NPs appear to have a larger number of pores at lower compression rates. Naturally, the bulk density of the mixture cannot be achieved, and all pellets contain a certain volume of pores.



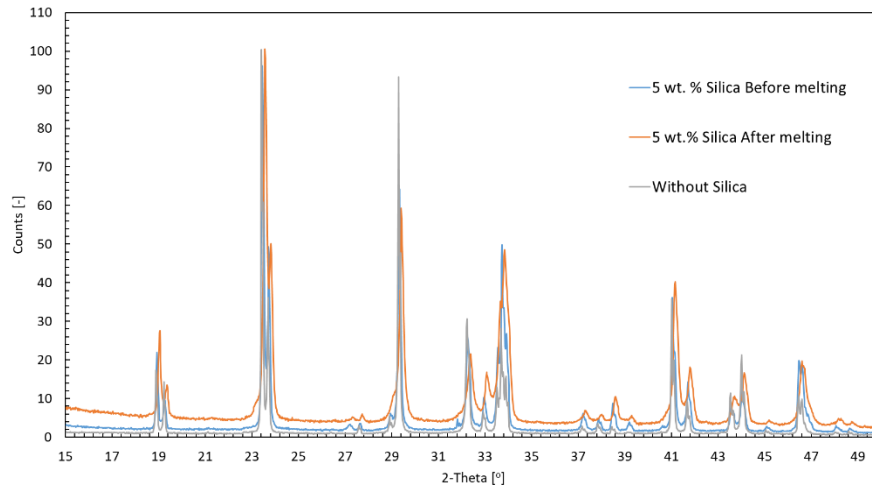


Figure 4.8 NaNO₃ (top) and KNO₃ (bottom) with 5.0 wt.% α -SiO₂ NPs

CA measurements show a significant dependence of the measured value on the compression rate. Pellets compressed at higher pressure rates show a more rapid decrease in the CA both in the base fluid and in the presence of NPs, while the opposite is true for pellets compressed at lower rates (see Figure 4.9b). This confirms that the observed transition in the CA measurements is further prolonged by the existence of pores in the structure of the salt. At higher compression rates it occurs at 280 °C, while at lower ones at 320°C. More pores translate to more air gaps, which prolong the phase transition time of the solar salt. Therefore, in the case of the CA, the delay (or extension) in the transition is found to be closely linked not only to the physics of the phenomena, but also the sample preparation process.

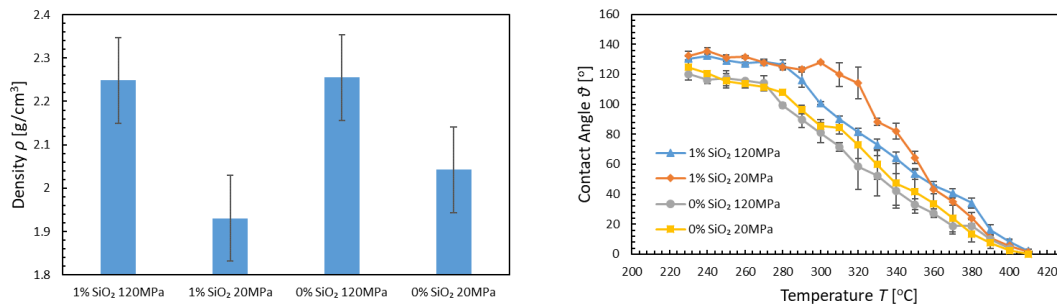


Figure 4.9 a) Density of Solar Salt + 1.0% wt. SiO₂ pellets compressed at different rates b) CA of Solar Salt and Solar Salt + 1.0% w.t SiO₂ with pellets compressed at 20 and 120MPa.

However, the same structural change that can be observed, given the change on the nanofluids wettability, leads to a non-linear drop in the viscosity at high temperatures. The fact that the structure collapses around 300 °C might allow the molecules to liberate from the internal forces that originally increased viscosity when adding NPs into a fluid. In that manner, the salt is more capable of allowing movement and the viscosity decreases reaching values almost similar to the base fluid above 350 °C. This phenomena which might be the reason of the eventual agglomeration and sedimentation of the salt after some cycles in practical applications ¹³⁶.

CA measurements are also conducted on a fused quartz substrate, whose roughness is almost identical to the original Al₂O₃ surface. It is observed that the initial CA on the silica surface is significantly lower than the case of the alumina (Figure 4.10). From wetting theory, it is known that in surfaces with similar roughness and polarity, the one that is more wetted has a higher surface energy ¹³⁷. It can thus be deduced that the surface energy of the fused quartz is higher compared to the alumina. Naturally, liquids with various surface tensions should be further examined to correctly calculate the surface energy through subsequent polynomial fittings ¹³⁸. Furthermore, NPs hydrophilicity has been linked to the motion of particles in a liquid, during

boiling in the case of water, and their subsequent deposition point either on the meniscus or edges of the droplet ¹³⁹. Conclusively the hydrophilicity of the NPs has a potentially strong effect on the force balance on the triple contact line and thus the CA.

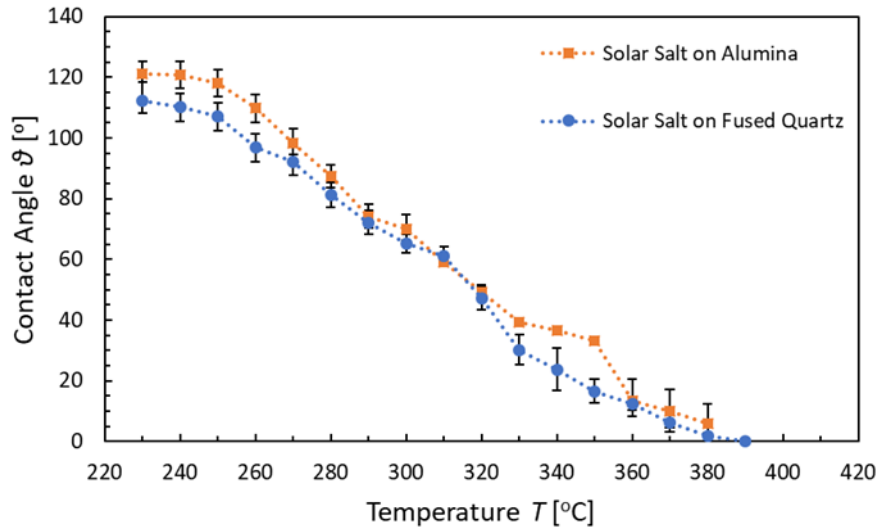


Figure 4.10 Contact Angle of solar salt on Alumina and Fused Quartz

Conclusively, the effect of the NPs on the evolution of the CA measurements is therefore hypothesized to be related to the effect of doping of α -SiO₂ on the force balance at the triple contact line. Future research should be conducted on the rheology and wettability of alumina doped nanofluids to compare the wetting behavior with results from the current study, as well as with other hydrophobic particles, such as graphite in order to create a more established understanding of the interplayed phenomena.

4.2 Effect of Surface Type on the Wetting behavior of Solar Salt

The effect of surface energy on the CA is well-known. Surface energy is the magnitude of inter and intramolecular forces on the surface of a material. It essentially determines

the total force that a surface can exert on a liquid. These forces are dependent on the crystal arrangement at the surface of the solid. Grain size, orientation and defects can increase or decrease the surface energy. Finally, temperature has a negative impact on the surface energy. An increase in temperature leads to an increase in the kinetic energy of the solid atoms. The atoms at the surface of the material vibrate more, thus creating more spacing between them and reducing their respective cohesive forces. As was observed in the previous section the CA between the two polycrystalline surfaces of Al_2O_3 and fused quartz, despite having almost identical roughness, showed a difference in the wetting behavior. As was discussed in the literature review the structure of the composite materials is dependent on the surface energy and thus the wetting behavior between the surface and the salt. To this end the CA of the SS on surfaces that are potential candidates for composite materials is measured (Figure 4.11). These were silica oxide, silica carbide, graphite, stainless steel and MgO.

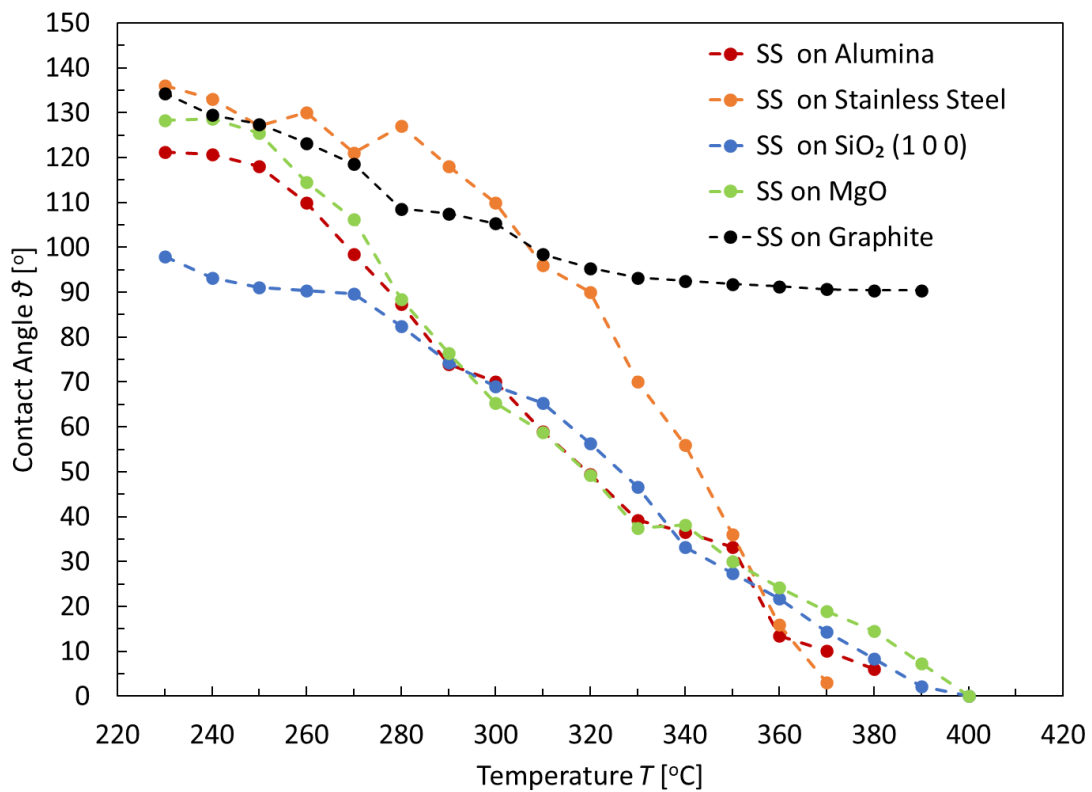


Figure 4.11 Contact Angle of Solar Salt. Dependence on surface type.

It can be seen that the molten salt wets all surfaces after 300 °C apart from graphite. Furthermore, silica carbide appears to be the most favorable material in terms of wettability and graphite the least, which strengthens the correlation between wettability of a material and composite stability as composite materials containing silica carbide present far more stable structures than those containing graphite¹⁴⁰. It should be noted that the particular stainless steel and graphite surfaces, on which the wettability tests were conducted, had far higher roughness than the ceramic mono/polycrystalline surfaces. However, as has been verified in the literature in the case of water, graphite presents hydrophobic behavior independent of roughness. This is also validated in this work through MD simulations (Chapter 5). The CA of the graphite is accurately predicted, and a non-wetting behavior is observed independent of surface roughness. This highly hydrophobic behavior of graphite makes it a good candidate for corrosion

prevention. Based on the findings of Grosu et al.¹⁸ and Piquot et al.⁵³ involving HitecXL salt and corrosion prevention through spray-graphitization, in this work the effect of spray-graphitization on the corrosion induced by molten carbonate salts is investigated. As mentioned in section 2.2 future CSP plants are aimed to operate in temperatures higher than the decomposition points of nitrate salts with carbonate salts being the best candidate in terms of thermophysical properties. For this reason, these salts are selected for the corrosion study.

4.3 Inhibition through graphitization of structural materials from hot corrosion by molten $\text{Li}_2\text{CO}_3\text{-Na}_2\text{CO}_3\text{-K}_2\text{CO}_3$ salt for concentrated solar power

In this section the inhibition of corrosion through the spray-graphitization method in order to improve compatibility of SS310 and SS347 with molten $\text{Li}_2\text{CO}_3\text{-Na}_2\text{CO}_3\text{-K}_2\text{CO}_3$ carbonate salt is investigated. Detailed characterization of the physical aspect of the corrosion process (wettability study) is conducted. For the corrosion test the pieces of SS310 and SS347 are cut as described in section 3.2 and placed in an alumina crucible and then immersed in 5g of salt. A lid is then placed on top of the crucible and the crucible is then placed in the carbolite furnace. These isothermal corrosion tests are carried out for 600h.

4.3.1 Corrosion Inhibition Results

The photographs of the salts as well as samples of SS347 after the corrosion tests are demonstrated in Figure 4.12. One can immediately see a considerable difference, when graphitization was applied. In particular, after the corrosion tests with non-graphitized SS347 the carbonate salt changed its color to green, while after the similar

test with graphitized SS347, the salt remained white with some graphite residues. At the same time, non-graphitized samples of SS347 demonstrated reddish color, in contrast to the graphitized samples, which were dark-grey after the test.

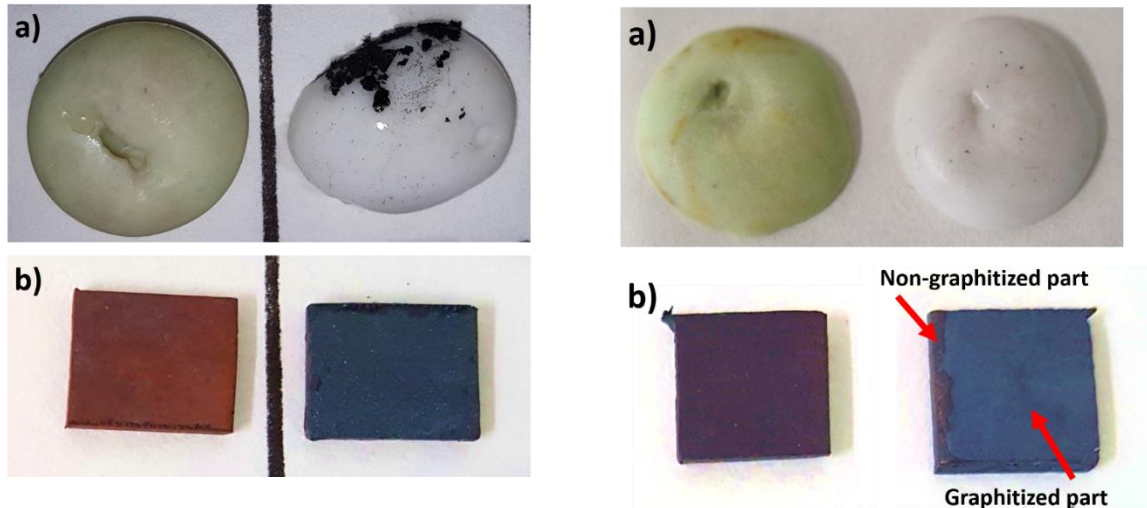


Figure 4.12 Photographs of SS347 corrosion results left column: a) carbonate salts and b) SS347 samples after 600h corrosion test at 600 °C and SS310 right column: a) carbonate salts and b) SS310 samples after 600h corrosion test at 600 °C

4.3.2 Wettability studies on graphitized surfaces

The observations presented above suggest that graphitization inhibits the corrosivity of molten carbonate salt. A wettability analysis is conducted on the ternary molten carbonate salt on both samples with and without graphitization in order to observe whether corrosion prevention is not only chemically, but also physically related and thus can be visualized through the observation of the CA.

Such experiments are useful for two reasons. Firstly, the wettability has profound effect on the corrosion process, namely, if a material is not wetted by the liquid, most likely there will be no corrosion as the interface area would be rather small. This is particularly, important for graphite, known for its low surface energy. Indeed, one can see that graphitized surfaces of both SS310 and SS347 demonstrate strong non-wetting behavior towards molten salt (Figure 4.13a), which is in striking contrast to non-graphitized cases. However, such non-wetting condition is only maintained for limited time (Figure 4.13b), due to decomposition of graphite according to reactions observed explained in Figure 4.14. After decomposition of graphite the salt fully wets the surface of stainless steel similarly to the non-graphitized case, therefore the obtained reduced corrosion rates are due to the chemical mechanism described above rather than to the physical differences in wetting behavior.

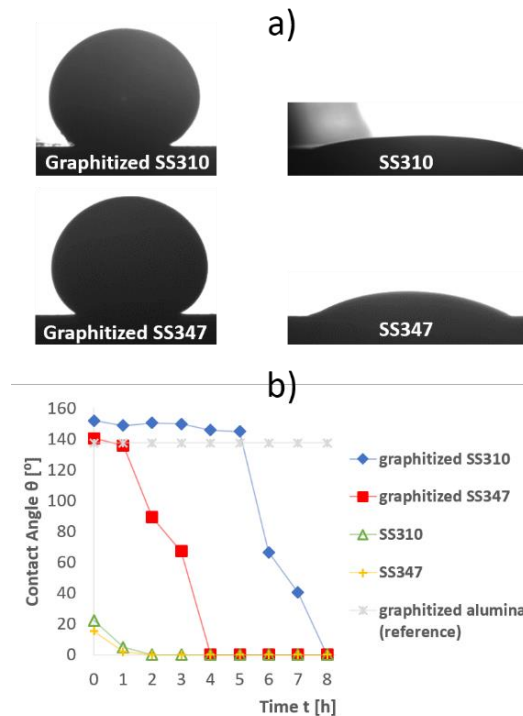


Figure 4.13 Contact angle of carbonate salt on SS310 and SS347 at 410°C a) just after melting and b) evolving with time

To further establish this correlation a wettability study is also conducted on a graphitized alumina surface, which is inert and thus non-reacting to the molten carbonate salt. It can be seen that the CA on the graphitized inert surface (alumina in this case) remained unchanged during the whole experiment, which further suggests that evolution of CA on the surfaces of graphitized SS347 and SS310 is due to chemical reactions described below rather than due to any reaction of the salt with graphite, or any physically induced hydrophobicity due to the non-wetting behavior of graphite. Finally, CA measurements were also conducted on non-graphitized alumina, which resulted in complete wetting behavior of the molten ternary salt.

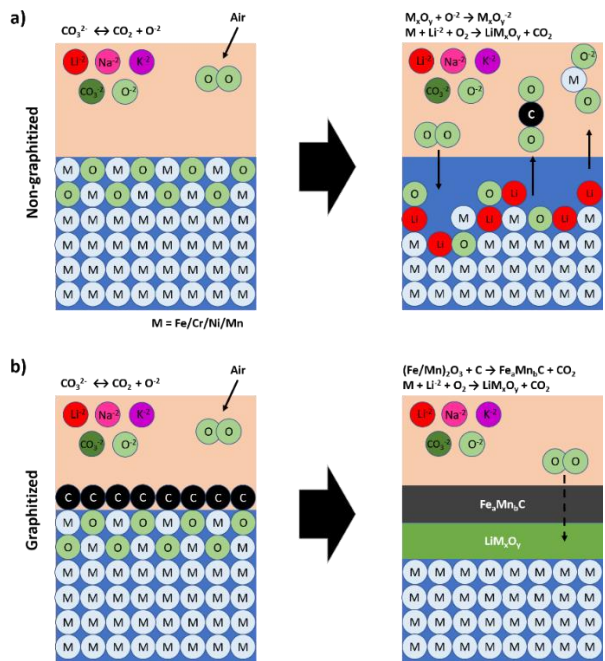


Figure 4.14 Schematic representation of corrosion process for a) SS310 and b) graphitized SS310 in molten carbonate salt

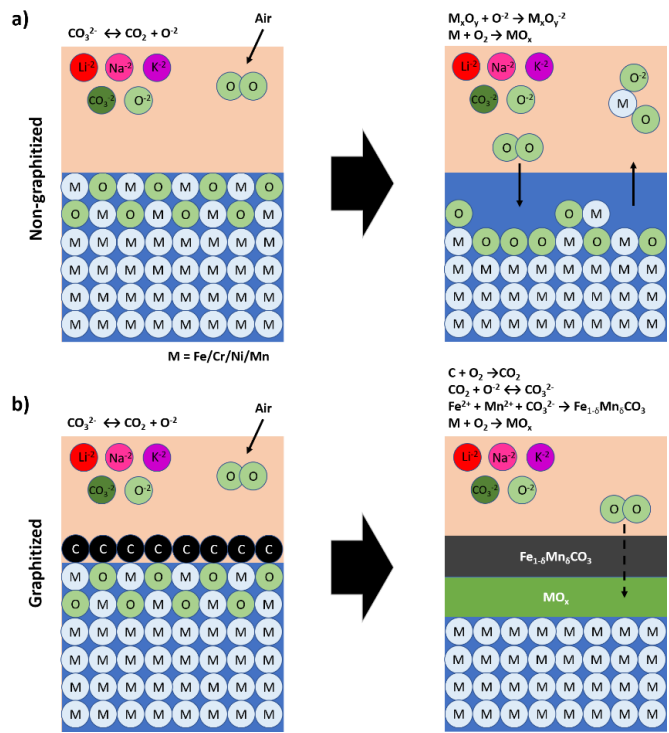


Figure 4.15 Schematic representation of corrosion process for a) SS347 and b) graphitized SS347 in molten carbonate salt

Secondly, since decomposition of graphite is accompanied by the transition to wetting state (Figure 4.13b), the optical observation of such transitions gives useful information about the kinetics of the involved chemical reactions. In particular, one can see that for graphitized SS310 the CA remains constant for around 5 hours, followed by a steep reduction. This is identified to be due to the graphite reacting with iron-manganese oxide to form iron-manganese carbide. These reactions are described in more detail in Grosu et al¹⁴¹. While the reaction is occurring the CA value is maintained, since the molten salt is in contact with unconsumed graphite. However, when the critical amount of graphite is consumed to form the carbide layer, the carbonate salt is in contact with iron-manganese carbide (Figure 4.14), which results in a wetting condition. On the contrary, the graphitized SS347 starts oxidizing from the beginning transforming to

iron-manganese carbonate (Figure 4.15). This is determined by a steady reduction of the CA with time from the beginning of the experiment.

Finally, one can see a noticeable time difference for carbonate (SS347) and carbide (SS310) formation. Namely, it takes 4 hours for SS347, to reach the wetting condition, while this time is doubled for SS310. This can be explained by the difference in Gibbs energy of the involved reactions. In particular, as calculated the Gibbs energy of reaction is found to be close to zero at 600 °C, becoming negative at slightly higher temperature. This strengthens the correlation between wetting conditions and reaction enthalpies. The reaction enthalpies can be found in detail in Grosu et al.¹⁴¹. Base on the above, a preliminary qualitative investigation of these reactions can thus be achieved through observational studies during CA measurements.

In this section further insights into the physiochemical mechanism of corrosion and corrosion inhibition through study of the wettability of graphitized surfaces are obtained. The formation of a carbonate protective layer, rather than carbide one is the principal mechanism behind the corrosion prevention. From the obtained results CA results, it is apparent that the chemical reactions at the liquid-solid interface govern the corrosion inhibition mechanism. However, it is concluded that the reactions occurring can also be visualized qualitatively through CA measurements and thus wettability studies can also have a secondary observational role to help identify candidates for corrosion inhibition.

4.4 CA of NaNO₃, KNO₃ and LiNO₃ on MgO (1 1 0)

In general, the CA and hence the wettability between materials is linked to the van der Waals interactions occurring between the two interacting materials. However, in the case of ionic liquids, such as molten salts, electrostatic interactions are more prevalent. Even in the case of water there is still a lack of knowledge, regarding the effect of the electron geometry on the formulation and bonding at the interface of the two interacting materials. In this section the CA of three very similar materials is measured to identify if their atomic and electrostatic variations (due to different ions) lead to a difference in their wetting behavior. The following tables contain results of CA measurements for NaNO₃, KNO₃ and LiNO₃ on MgO (1 1 0), throughout a common temperature range (Figure 4.16). These 3 salts all have the same base nitrate anion (⁻NO₃) with their only difference being the other single element, Na, K and Li respectively. In order to better identify the role that the ion can play in the wetting process, the CA of the salts is compared in identical wetting conditions. Snapshots from the high definition camera are provided to help visualize the magnitude of difference between the angles of the 3 salts.

Table 4.1 CA measurements of NaNO₃ on MgO (1 1 0)

Temperature (°C)	Angle (°)					Average Angle (°)	Standard Dev. (°)
310	70.15	74.3	67.3	71.5	-	70.81	7
320	65.65	55.78	49.7	56.21	47.8	55.028	17.85
330	56.1	42.3	41.5	45.3	40.3	45.1	15.8
340	46.1	38.16	37.4	41.5	37.7	40.172	8.7



Figure 4.16 CA of (left to right) LiNO_3 , NaNO_3 and KNO_3 at 340 °C

Table 4.2 CA measurements of LiNO_3 on MgO (1 1 0)

Temperature (°C)	Angle (°)				Average Angle (°)	Standard Dev. (°)
260	79.34	78.6	79.70	76.9	78.635	2.8
310	31.58	34.2	-	30.42	32.06	3.78
320	24.5	29.2	-	20.2	24.5	9
330	12.2	14.5	-	14.05	14.025	2.3
340	-	11.2	-	12.32	11.76	1.12

Table 4.3 CA measurements of KNO_3 on MgO (1 1 0)

Temperature (°C)	Angle (°)				Average Angle (°)	Standard Dev. (°)
334	65.15	68.2	70.2	68.3	67.96	5.05
340	-	60.9	63.6	61.7	61.7	2.7

It can be seen that the CA of all 3 materials decreases as the temperature increases. Furthermore, at 330°C KNO_3 , has the largest angle at 67.96°, while LiNO_3 the smallest at 11.76°. The following table contains data related to the atomic properties of the ion of each salt. Additionally, the pattern of the CA is matching with the atomic properties of the 3 materials. The Li possessing the lowest values and K the largest. It can be, thus, concluded that there is a strong correlation between the ionic structure of a material and its wetting behavior. This could be potentially, linked to research suggesting that the specific heat capacity enhancement in MSNFs could be linked to the ion exchange capacity of the ion in the corresponding salt¹⁵.

Table 4.4 Atomic properties of NaNO₃, LiNO₃ and KNO₃

Element	Atomic Weight	Atomic Radius (A)	Ionic Radius (A)
Na	22.99	1.857	0.98
K	39.10	2.312	1.33
Li	6.94	1.519	0.78

Furthermore, the electronic configuration of Li is $1s^2 2s^1$, while the one of Na is $1s^2 2s^2 2p^6 3s^1$ and finally the one of K is $1s^2 2s^2 2p^6 3s^2 3p^6 4s^1$. The electron configuration of Li is by far simpler than K, which translates to a higher capacity for electron exchange. Additionally, the configuration of K⁺ is significantly more complex than that of Na⁺, which further agrees with the correlations deduce from the comparison between the CA of the two materials. From the above observations a strong correlation between the wetting of materials and their atomic and electronic configuration is apparent. Further research is required to identify the role of the composition of salts on the wetting process and other transport phenomena such as their specific heat capacity when doped with NPs.

To this end the effect of the molar composition on the CA of molten salts is investigated. Specifically, the ratio of Na⁺ and K⁺ in NaNO₃ – KNO₃ mixtures is examined to identify if there is an effect on their wetting behavior. CA measurements are conducted with identical heating rates. The results are presented in Figure 4.17. NaNO₃ and KNO₃ are also included in the figure for reference. Molar fractions are varied at 20% intervals.

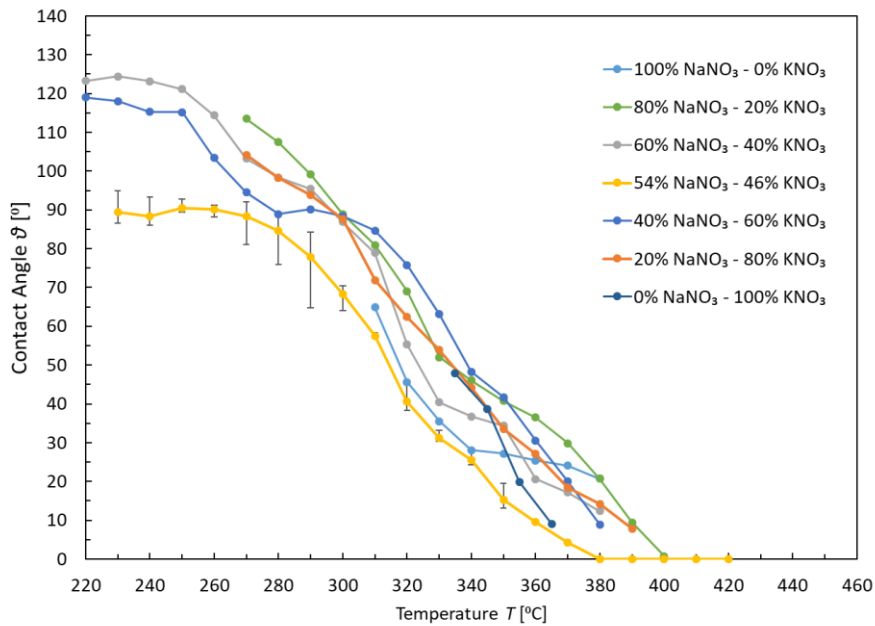


Figure 4.17 CA of molten NaNO₃ - KNO₃. Dependence on molar ratios

No significant difference is observed in the CA between the 4 different molar ratios. All exhibit an almost linear decrease in the CA with an increase in temperature. Comparing ratios with similar melting points (i.e. 20% - 80% and 80% - 20% or 40-60% with 60 – 40% NaNO₃ – KNO₃) K⁺ rich compositions appear to show an initial difference of ~10°, which after few tenths of degrees disappears. This can be correlated with the slope of figure 4.5 presenting the dependence of the melting point on the ratio of KNO₃. The line from 0.0 to 50.0% molar ratio of KNO₃ has a smaller slope than the curve from 50.0 to 100.0%. This translates to a higher energy demand to facilitate phase change. Thus, it can be concluded that the liquid solid transition takes longer to realize. It is important to note that the ideal eutectic doesn't present this behavior and thus the CA appears significantly lower. It would be interesting to see the effect of the addition of silica on each different molar composition, to identify if some molar ratios are inhibited more than others.

4.5 Effect of particle size on the CA of MSNFs. A study on the wettability of graphite doped Solar Salt.

The CA of molten salt with amorphous SiO₂ is investigated in section 4.1. To develop a better understanding of the effect of NP doping on the wetting and rheology of molten salts the behavior of MSNFs with various three different type of carbon particles is examined. The particles are spherical nano particles (15-20nm), micro sized particles (500µm) and graphite flakes (150µm). The MSNFs are produced using the triple step method as described in section 3.2. Three different concentrations are prepared: 0.5, 1.0 and 1.5 wt. %. Unfortunately, concentrations above 0.5 wt. % did not produce a droplet upon melting and where thus omitted from the study. This was due to the very large increases in their viscosity, which at lower temperatures up to the decomposition temperatures of carbon (< 400°C) led to the formation of a composite structure.

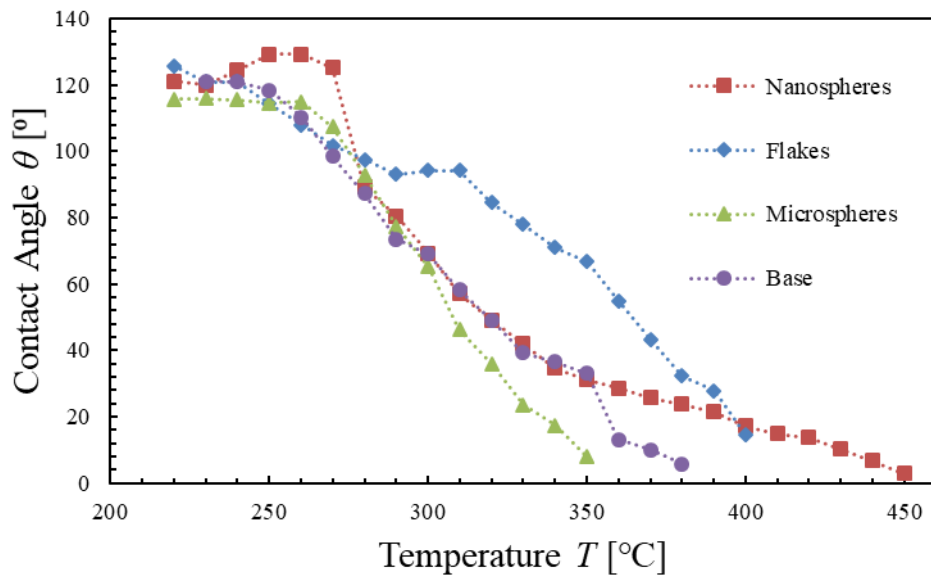


Figure 4.18 Contact Angle versus Temperature of Solar Salt doped with Nanospheres (10-15nm), Flakes (150 μ m) and Microspheres (500 μ m)

As in the case of the silica doped SS, it appears that the addition of a very small amount of particles heavily affects the wetting process. However, the evolution of the CA is different depending on the diameter of the carbon particles. The nano sized particles (NS) display a plateau with an increase in the CA up to 270 °C, after which a transition is observed followed by a wetting behavior identical to that of the base salt until 350 °C. At this point though, instead of completely wetting the surface the CA stabilizes and is slowly reduced up to 450 °C, where a complete wetting is observed, roughly 70 °C above the base case. Flakes (FL) on the other hand, display a non-wetting behavior up until 310 °C, after which the CA is gradually reduced, retaining values on average 30% higher than the base, up until 410 °C where complete wetting is observed. Finally, the micro sized spheres (MM) show marginal differences compared to the base case. Furthermore, after 290 °C the MSNF wets the ceramic surface in a more rapid manner

when compared to the base case, achieving full wetting conditions at 360 °C instead of 380 °C.

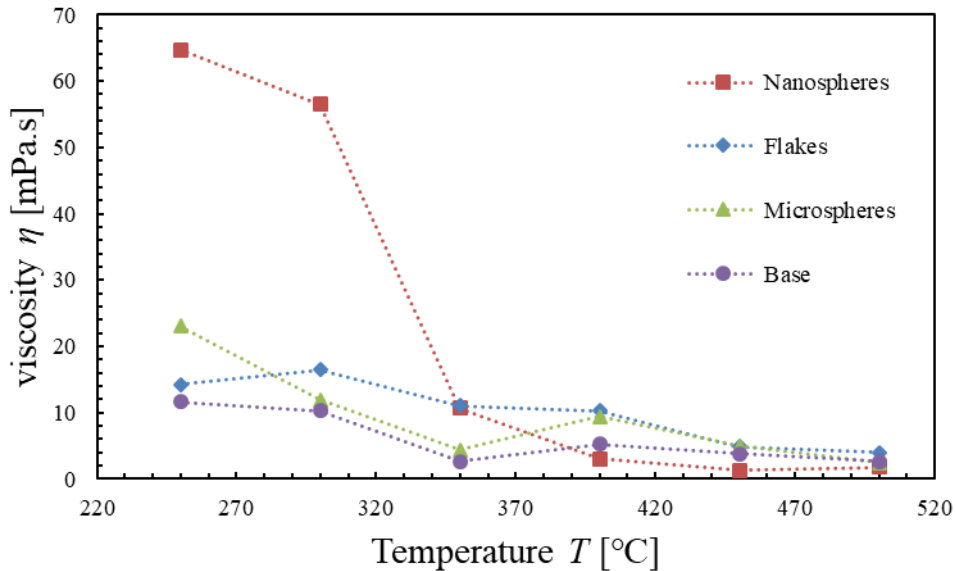


Figure 4.19 Viscosity vs Temperature of Solar Salt doped with 0.5 wt.% of 3 different type of graphite particles. (Adapted from Palacios et al.²⁸)

Looking at the viscosity of the 3 different MSNFs (Figure 4.19), a strong correlation between the two phenomena is evident. The NS doped MSNF displays a huge value roughly 145% that of the base salt, which then reduced to values close to the base salt at 350 °C. On the other hand, the flakes have stable viscosity, always higher than the base case, which is gradually reduced with temperature and coincides with that of the base salt at 450 °C. Finally, the MM has a viscosity higher than that of the base salt at 250 °C, but then coincides with that of the base salt at 300 °C.

These trends strongly agree with the wetting behavior displayed in Figure 4.16. The NS particles show a drastic reduction close to 300 °C, the MM values close to the base after 310 °C and the flakes a gradual reduction with complete wetting at 470 °C. Due to

the difference in the physics of each measurement, complete agreement is impossible. This is discussed in detail in section 4.1.2. Furthermore, unlike the case of the silica the change in the CA values occurs earlier than the viscosity. For example, the NS particles display a reduction, to values below the base, in the viscosity at 350 °C, but the respective CA transition is observed at 280 °C. Additionally, the viscosity of the MM salt is increased at 400 °C, with respect to its value at 350 °C, but instead the salt wets the surface even more than the base case. This difference in wetting behavior is linked to the hydrophilicity/hydrophobicity of the NPs and the subsequent effect that has on the surface tension and thus the CA balance at the triple contact line.

To further demonstrate this idea, quenching tests in liquid nitrogen were conducted. A pellet of SS mixed with micrometer particles was placed on top of a sheet of aluminum foil and melted on a hot plate. The pellet was covered with an insulated glass funnel to minimize any temperature gradients. 10 minutes after the pellet reached 250 °C the aluminum foil was removed and rapidly placed in a bath of liquid nitrogen. The solidified droplet was then cut in half and inspected (Figure 4.20). The segregation of the graphite and its subsequent clustering on the top of the droplet is evident. It can be seen that in the triple contact line minimum amount of graphite is present. This, as explained, has a considerable impact on the balance of the forces that dictate the wetting behavior of the liquid. This experiment was repeated three times with identical results. Due to the contrast in color this is easy to visualize with carbon particles, but conclusions from similar attempts with silica doped SS were impossible to be drawn due to the similarities in color between the salt and the silica NPs (even at low contrast).

Further research is required, using SEM to visualize how particles with different surface energy behave and how can that be linked to the wetting behavior of the MSNFs.

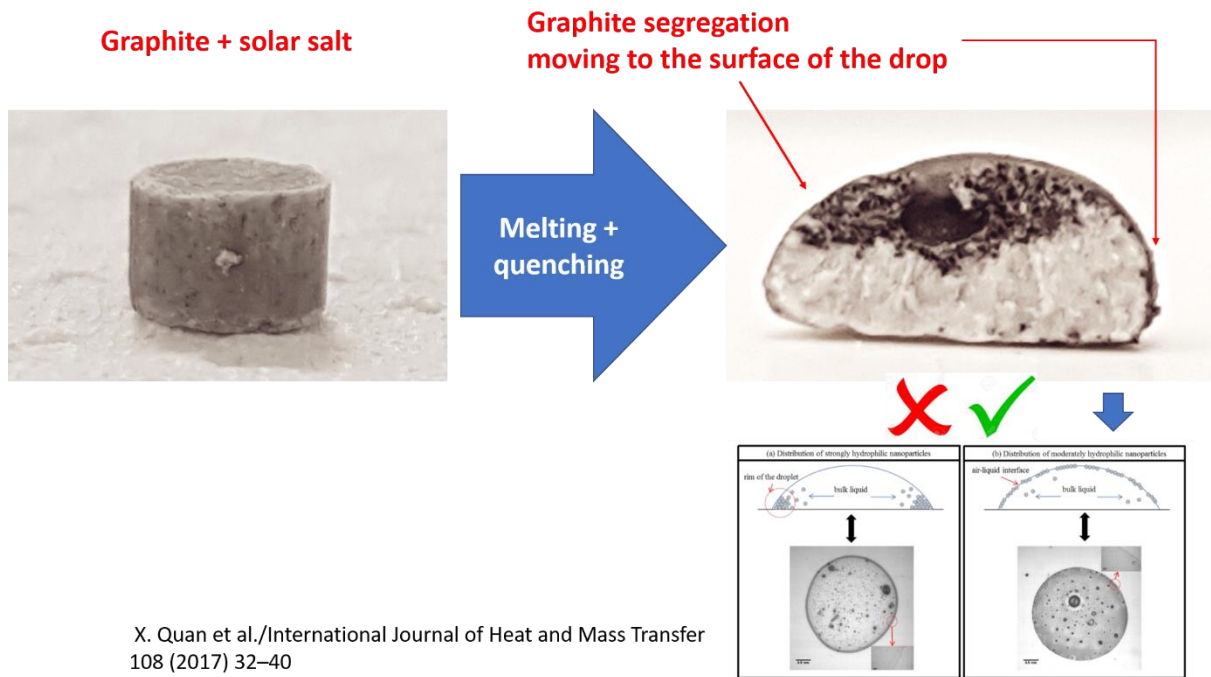


Figure 4.20 Solar Salt + graphite pellet before (left) and after (right) melting and quenching. Bottom row displays movement of nanoparticles in boiling water nanofluid¹³⁹.

Chapter 5 MOLECULAR DYNAMICS SIMULATIONS

In the previous chapter an effect of adding NPs on the wettability of the MSNF is demonstrated. However, experimental measurements were not sufficient to describe it. In this chapter MD simulations are employed to provide an alternative scope on this complex phenomenon. In order to effectively simulate cross-term interactions, that are crucial to model wetting behavior, two set of force field parameters are developed and validated. One for the SS and one for the silica NPs. These are then used to study the interface between SS and NPs. Furthermore, the wetting of a molten salt droplet on a ceramic and carbon surface is also correctly simulated, accounting correctly for the effect of scale. Finally, the wetting behavior of a MSNF is also captured through atomistic simulations.

5.1 Development of Simplified Force Field parameters for the simulation of molten nitrate salt mixtures

5.1.1 Advantages of Lennard-Jones force fields in cross-term interactions

Interatomic potentials are functions used to calculate the potential energy of atoms with respect to their positions. The simplest types of interatomic potentials that are

most commonly used are pair potentials. Pair potentials, essentially describe the potential energy developed between a pair of atoms of same or different type. Molten salts are mostly simulated using Buckingham or Morse type pair potentials.

The first term (Eq. 3.12) is responsible for calculating the long-range electrostatic Coulomb interactions and the second term responsible for the forces mostly governed by van der Waals forces. The term raised on the 12th power depicts the short-range repulsion, while the term raised on the 6th power describes long-range attractions in terms of Van Der Waals and dispersion forces. All interatomic potentials are essentially mathematical approximations derived to fit quantum mechanical data that describe interactions between electron dipoles. The dispersion (6th power term), though has a clear physical resemblance attributed to Pauli's laws of repulsion. However, the 12th power term is entirely theoretical and is used because it gives a satisfying approximation of Pauli's repulsion well with little computational burden. Therefore, a lot of times these potentials may present unrealistic results. For example, in the Buckingham potential (Eq. 3.13) the approximation of Pauli's potential well is given by an exponential term, fitted with the use of two constants A and B. However, when the value of the minimum energy distances approaches zero, the exponential leads to interaction energies diverging to zero, which causes atom overlap. These type of interactions creates issues when dealing with modelling of interfaces.

5.1.2 Lennard-Jones Parameters for simulation of Solar Salt

The optimal values of ϵ and σ for the Lennard-jones potential for the pairs Na-Na, O-O, N-N and K-K are derived by fitting the NaNO₃ and KNO₃ Buckingham potentials of Jayaraman et al. ¹⁰⁰. The fitting was obtained by minimizing the least square error

between the energy-distance curves of the two potentials. However, σ of the K-K pair was slightly modified from the initially obtained value in order to compensate for the under prediction of the density of KNO_3 at the melting point, by the Buckingham potential.

Cross-term interactions are calculated by means of the Lorentz-Berthelot mixing rules.

Table 5.1 shows the newly developed interatomic parameters.

Table 5.1. Lennard-Jones Parameters of NaNO_3 and KNO_3

Element	Q [e]	E [eV]	σ [Å]
Na	1	0.0066373	2.407
K	1	0.004336	3.188
N	0.95	0.004017509	3.431
O	-0.65	0.003469129	3.285

5.1.2.1 Intramolecular potential

The bond, angle and improper dihedral potentials of the nitrate (NO_3) structure are also accounted for. The N-O bond is simulated as a harmonic bond, with a harmonic bond constant of 525.0 ($\text{kcal}\cdot\text{mol}^{-1}\cdot\text{Å}^{-1}$) and an equilibrium bond length of 1.2676 (Å). The O-N-O angle is simulated as a harmonic angle with an angular constant of 105.0 ($\text{kcal}\cdot\text{mol}^{-1}\cdot\text{rad}^{-2}$) and an equilibrium angle of 120° . The improper O-N-O-O is simulated by a harmonic improper dihedral potential with constant 60.0 ($\text{kcal}\cdot\text{mol}^{-1}\cdot\text{rad}^{-2}$) and equilibrium angle of 0.0. The values for the intramolecular parameters are taken from the work of Qiao et al ⁹⁸. For all 3 cases the equation has the following format:

$$E = K(r - r_0)^2 \quad (5.1)$$

where, E is the harmonic potential, K a constant and r_0 the equilibrium bond length in the case of the bond, or the equilibrium angle in the case of the angle, or improper dihedral potential.

Pure molten NaNO_3 , KNO_3 and three mixtures (Table 5.2) were investigated. The mixture 59.66%-40.44% was selected due to it being the most commonly used mixture in the CSP industry; the 50%-50% molar is close to the pure eutectic mixture of the two salts, while the 3rd mixture (40.44- 59.66%) is chosen to test the accuracy of the proposed potential when KNO_3 is the major component of the mixture.

Table 5.2. NaNO_3 - KNO_3 Simulated Systems

NaNO_3 - KNO_3 (%)	Sodium Ions	Potassium Ions	Total Atoms
59.66%- 40.44%	960	384	6720
50%-50%	980	576	7780
40.44%- 59.66%	860	508	6829

For the pure salts, the crystalline structures of NaNO_3 and KNO_3 are taken from Gonschorek et al and Adiwidjaja et al. respectively, and replicated in all dimensions, so that the resulting system consists of 4900 atoms ^{142,143}.

Quenching is applied to the initial cell for equilibration. After a Polak-Ribiere structure minimization ¹⁴⁴, the system is rapidly heated up from 293 to 1300K in 0.3 ns, in the

NVT ensemble with a Nose-Hover thermostat and barostat ¹⁴⁵. Subsequently, it is equilibrated at 1300K for 0.5 ns in the NVT ensemble followed by a slow cool down up to the melting point in the NPT ensemble for 1 ns ¹⁴⁶. The final structure is obtained by further relaxing the system in the NVT ensemble for 0.5ns (Figure 5.1).

The cutoff of the interatomic potential is set at 15Å, with long-term and columbic interactions being computed using Hockney’s Particle-Particle Particle-Mesh (PPPM) method ¹⁴⁷. The equations of motions are solved using the Verlet leap-frog algorithm ¹⁴⁸. In all the simulations, the timestep is 0.0001ps.

For the SS, the previous NaNO₃ and KNO₃ unit cells are replicated in a way to achieve the desired atom molar ratio. To avoid atom overlap, a variable random displacement of all atoms is applied in all 3 dimensions, using a specific routine in LAMMPS called “fix move”. Then a minimization and quenching process as described above is applied to obtain the final structure.

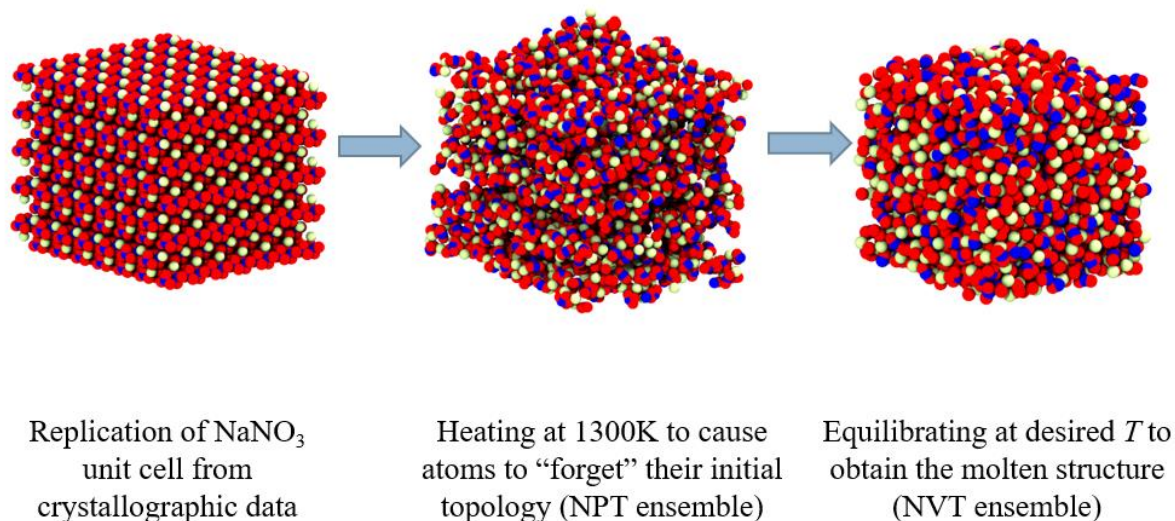


Figure 5.1 Equilibration process for the formulation of molten NaNO₃

To ensure the validity of the potential as well as the entire simulation, the RDF and coordination curves were calculated and hence the structural behavior of the molten salt throughout its entire liquid phase is analyzed. At higher temperature levels, the liquid becomes less dense, thus leading to a more relaxed structure with larger distances between the nitrate molecules, as well as the potassium and sodium atoms.

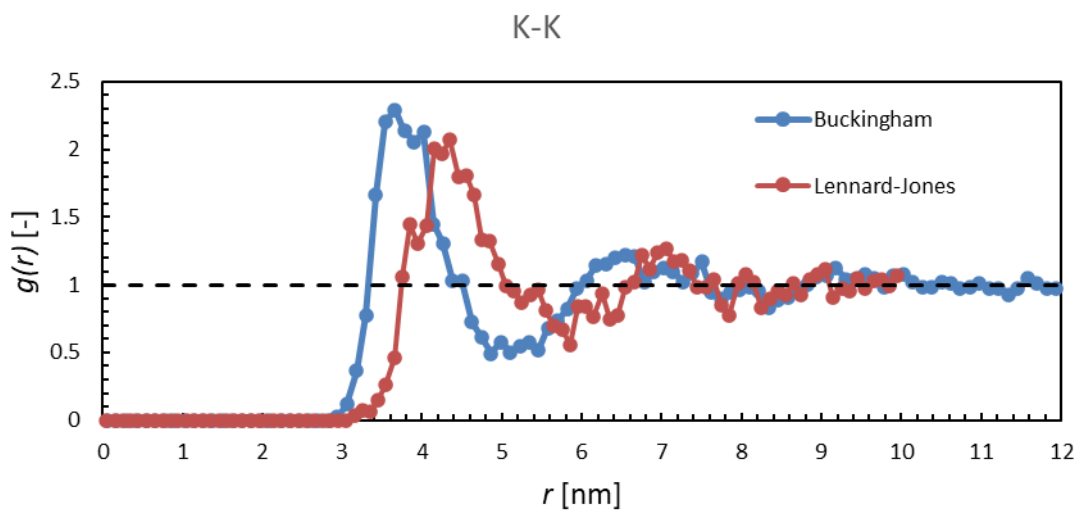
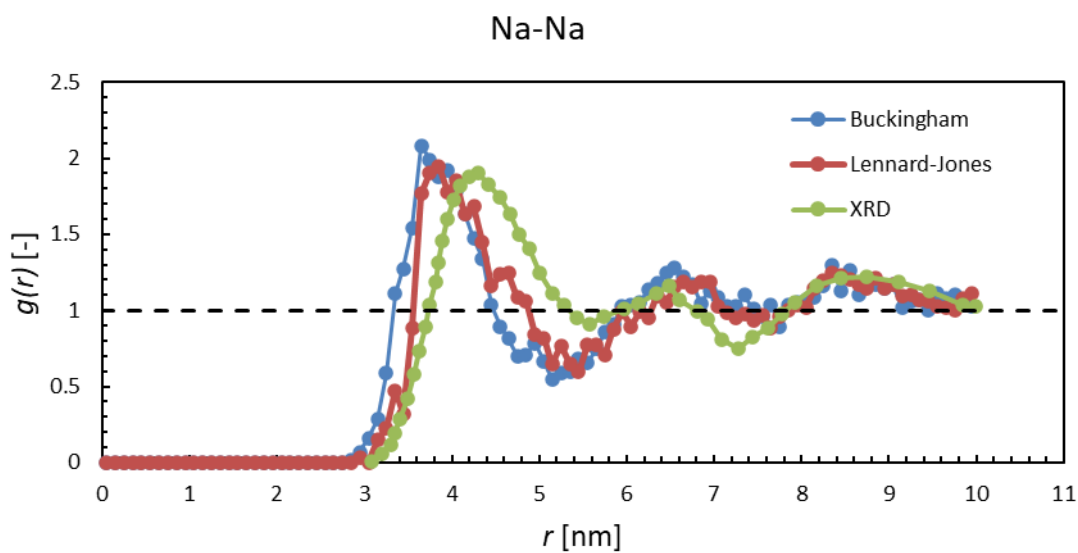
Since, the goal is to validate the nanoscale simulations with the macroscale experimental measurements the transport properties of the molten salt are calculated and compared with experimental measurements provided by group members or found in the literature. The methods used to calculate the properties can be found in section 3.3.2.

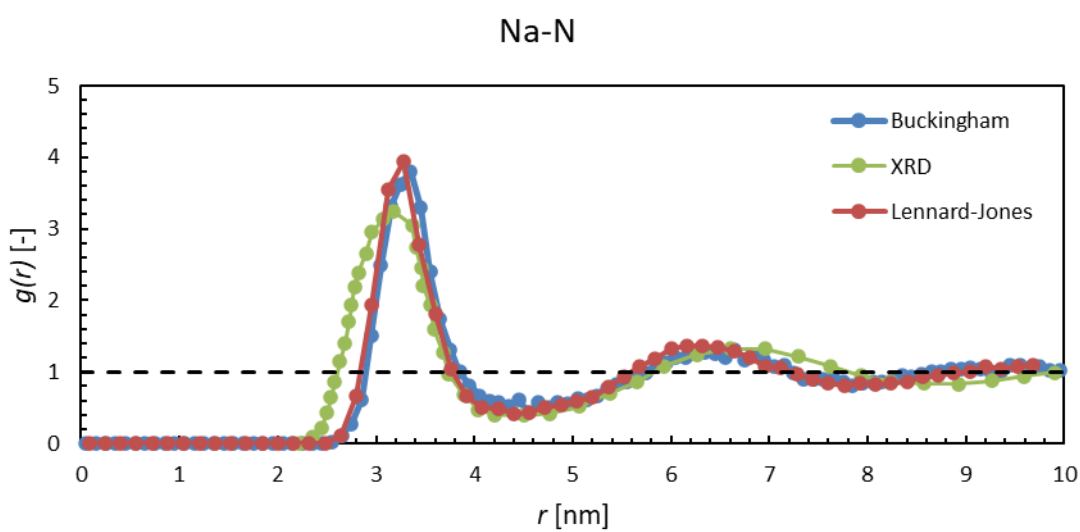
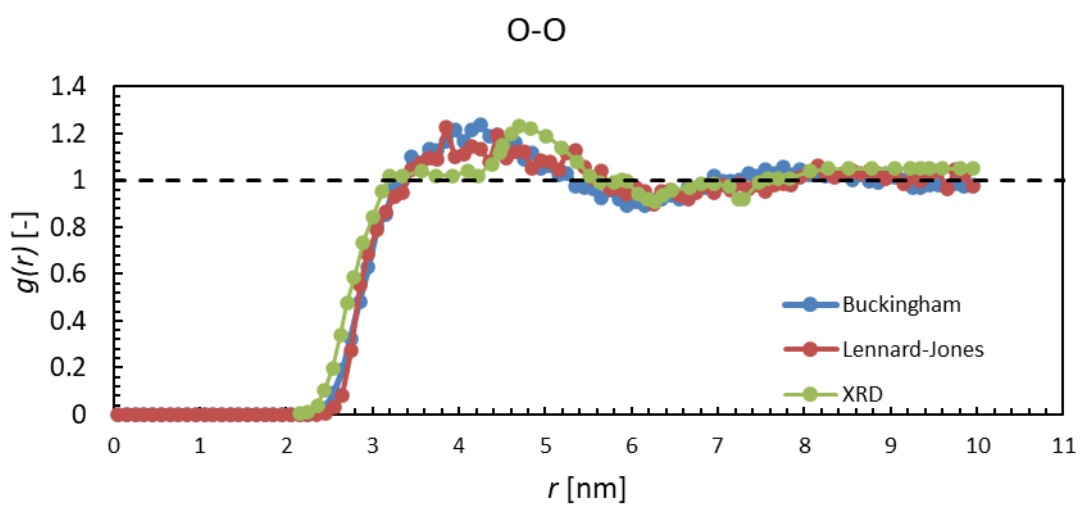
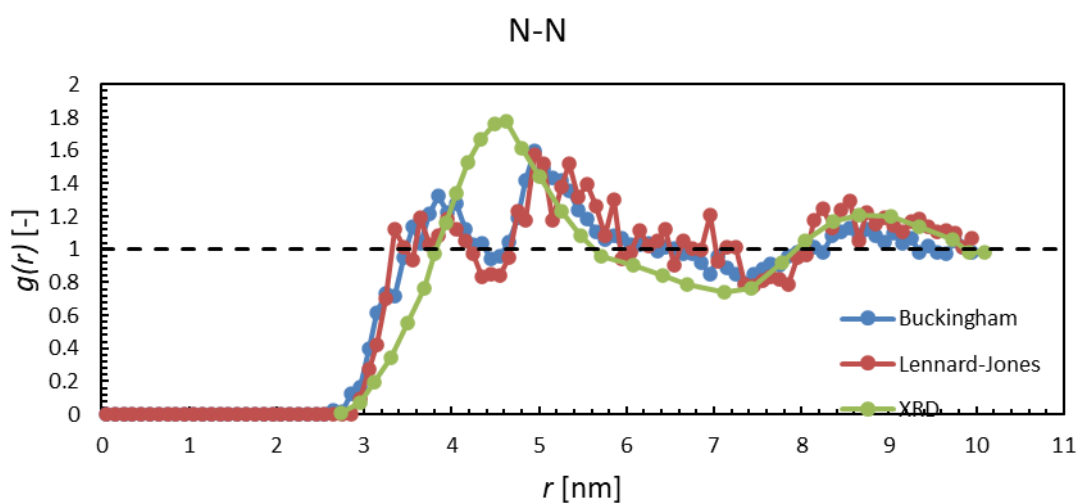
5.1.3 Prediction of the Local-Structures of NaNO_3 and KNO_3

To validate the Lennard-Jones parameters proposed in this study, pure NaNO_3 and KNO_3 salts were simulated with both the Buckingham parameters from Jayaraman et al.¹⁰⁰, and the proposed Lennard-Jones potential.

In the case of the nitrogen and oxygen the distributions are almost identical, which is to be expected as bond, angle and improper forces are present and hold the nitrate structure firm. In the case of the sodium and potassium minor deviations can be seen between the two potentials, especially at the point of the first peak. This is anticipated and is related to the difference in mathematical formulations, between the Buckingham and the Lennard-Jones potentials. Furthermore, The K-K interaction potential, as

explained in section 5.1.3, has been slightly modified to improve the accuracy of the density.





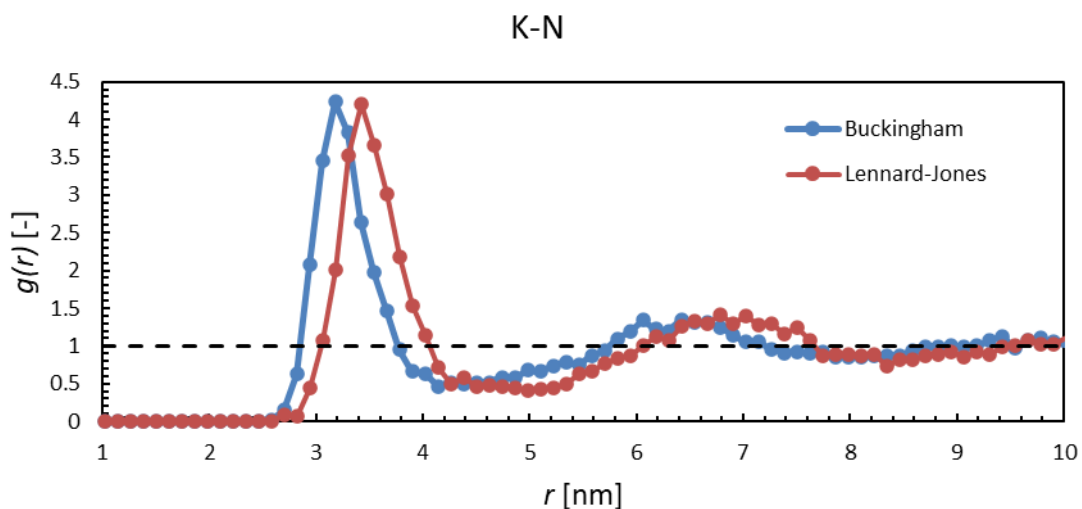


Figure 5.2. Radial Distribution function of NaNO_3 and KNO_3 , comparison between Buckingham, Lennard-Jones potentials and XRD experimental data from Adya et al.⁹⁷.

5.1.4 Prediction of the Transport Properties and Surface Tension of molten nitrate salts

In this section, the Lennard-Jones potential is used to calculate several properties (i.e. viscosity, thermal conductivity, surface tension) of the NaNO_3 , the KNO_3 and their mixtures with different compositions. Results are compared against available experimental data. Results are gathered in Table 5.3. The calculated properties are compared across a range of temperatures that comprises the entire liquid phase, between the melting and the decomposition point, for each mixture. The melting temperatures are considered to be 310 and 335 °C for NaNO_3 and KNO_3 , 250 °C for the 60%-40% and 40%- 60% and 220 °C for the 50%-50% mixture. Decomposition temperatures vary depending on the heating rate and atmospheric conditions. The lowest temperatures under which no decomposition occurs under any conditions are at 400 °C for NaNO_3 and KNO_3 , with the case of the KNO_3 representing a boiling point. In the case of the mixtures it is assumed that decomposition starts at 450 °C.

Table 5.3. Comparison between experimental measurements and calculated values for NaNO₃, KNO₃ and their mixtures for various properties ^{128,149–152}.

Material	NaNO ₃		KNO ₃		60% NaNO ₃ -40% KNO ₃		50% NaNO ₃ -50% KNO ₃		40%NaNO ₃ -60% KNO ₃		
	T_{melt}	T_{dec}	T_{melt}	T_{dec}	T_{melt}	T_{dec}	T_{melt}	T_{dec}	T_{melt}	T_{dec}	
Density ρ (g/cm ³)	Exp	1.93	1.85	1.86	1.79	1.98	1.79	1.93	1.80	1.93	1.81
	Sim	1.93	1.86	1.86	1.80	2.05	1.86	2.02	1.91	2.08	1.94
Viscosity η (mP/s)	Exp	2.94	2.17	2.57	2.07	4.61	1.48	4.72	1.57	-	-
	Sim	3.42	2.47	2.27	1.92	3.87	1.51	3.91	1.79	3.46	1.63
Thermal Conductivity k (W/m·K)	Exp	0.51	0.50	0.41	0.38	0.48	0.53	0.48	0.53	0.46	0.51
	Sim	0.64	0.68	0.58	0.54	0.56	0.44	0.59	0.54	0.71	0.62
Self-Diffusion D (cm ² /s · 10 ⁻⁵)	Exp	3.37	4.93	1.48	2.22	1.36	3.23	-	-	-	-
	Sim	0.893	1.76	0.364	0.823	0.352	1.532	0.124	1.345	0.257	1.834
Surface Tension γ (mN/m)	Exp	119.8	115.5	116.7	107.3	118.9	108.2	120.7	107.1	120.1	106.3
	Sim	135.7	129.4	128.6	122.2	136.3	114.2	133.4	115.2	136.5	119.8

For the individual components the density prediction is excellent. In terms of the mixtures, slight variations in density are attributed to the empirical nature of the cross-term interactions. Viscosity is overestimated. In all cases absolute values are within 12.32% deviation from experimental measurements. Thermal conductivity in all cases is overpredicted and presents an increasing trend. This, as further discussed below, is linked to both the uncertainty of the thermal conductivity and also the way that the property is defined in the molecular level. Diffusion coefficients are highly overpredicted in all cases. However, from the calculated results, the advantage of MD studies can be recognized. Values are obtained in cases where experimental measurements are lacking, providing, if not a perfect prediction, an accurate estimation of the trend. Surface tension values are overappreciated in all cases, but differences from experimental measurements are in no case higher than 14.56%. In general, the

calculated properties provided with the use of the presented interatomic parameters are in good agreement with literature data.

5.1.4.1 Density

The density of the solar salt, throughout its entire liquid phase temperature range can be seen in Figure 5.3. The average difference between computed and measured values is 6.1%. This could be attributed to the cross-term interactions between Na and K, which are based on the mixing rule, that contains some degree of inaccuracy. Naturally at higher temperature levels, kinetic energy causes the molecular structure of the liquid to become more spread and hence the density is reduced.

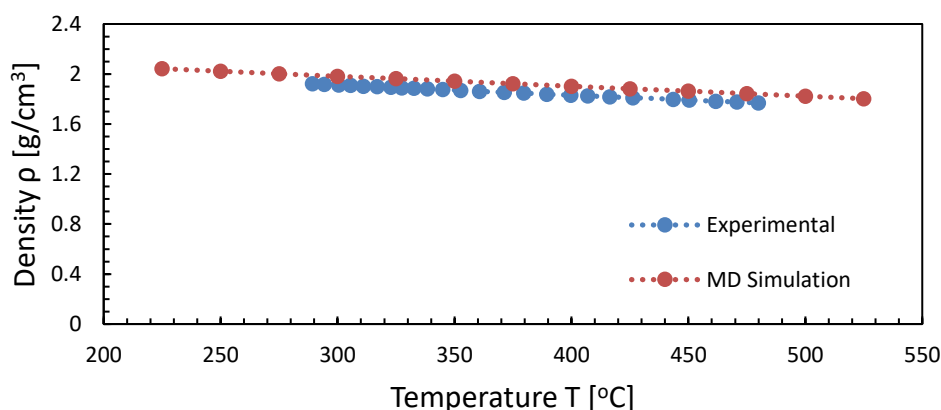


Figure 5.3. Density of Solar Salt (60% NaNO₃-40% KNO₃), comparison with experimental data¹²⁸.

5.1.4.2 Thermal Conductivity

Simulations overall agree with the available experimental data. However (Fig. 5.4), the trend is not the same for $T > 400$ °C. We do not have a clear explanation for this difference, which also occurs in other MD studies concerning molten nitrate salts, using the Buckingham potential¹⁰³. However, it must be noted that experimental thermal

conductivity measurements are particularly difficult at these temperatures and often are not consistent with each other.

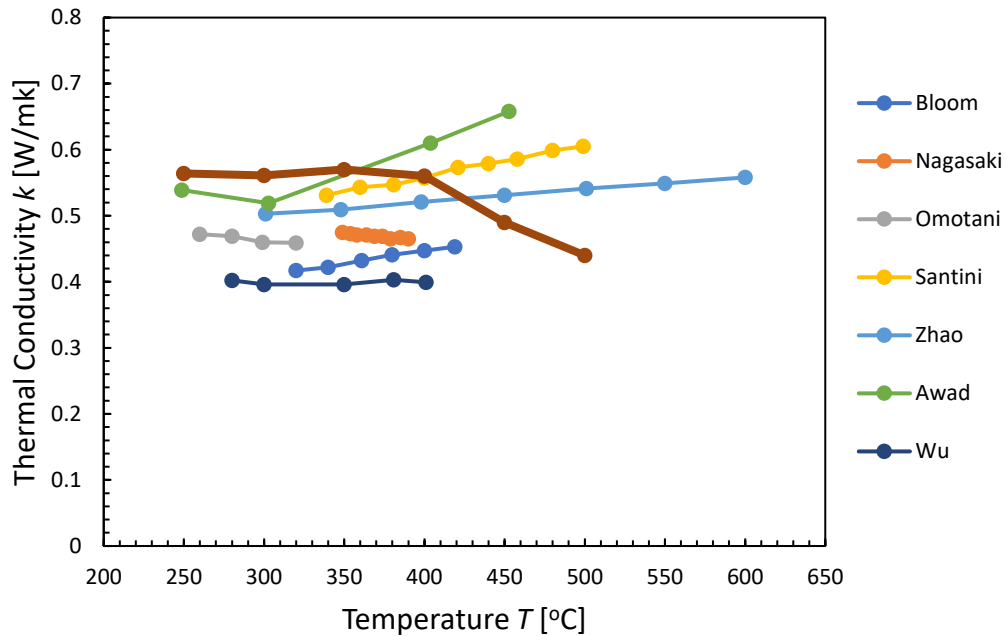


Figure 5.4. Thermal Conductivity of Solar Salt (60% NaNO₃-40% KNO₃), comparison with experimental data ¹⁵²⁻¹⁵⁷.

5.1.4.3 Viscosity

A comparison between the calculated and measured values is shown in Figure 5.5: average difference is around 10%. The trend of the molten salt density with respect to temperature (Figure. 5.3), confirms that at higher temperatures, the molten liquid becomes less dense, with distances between the atoms becoming larger, leading to a smaller resistance to shear stress and thus an expected reduction in the viscosity.

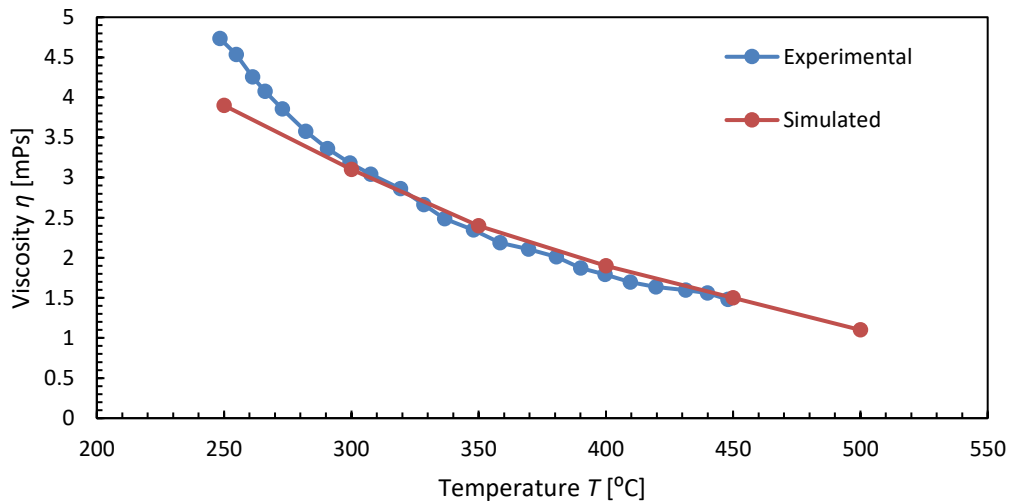


Figure 5.5. Viscosity of Solar Salt (60% NaNO₃-40% KNO₃), comparison with experimental data¹⁵⁸.

5.1.4.4 Surface Tension

Both experimental and calculated results follow the same trend (Figure 5.6). No experimental data were found for values above 400 °C. Average percentage difference between experimental and simulated values is 8.6%.

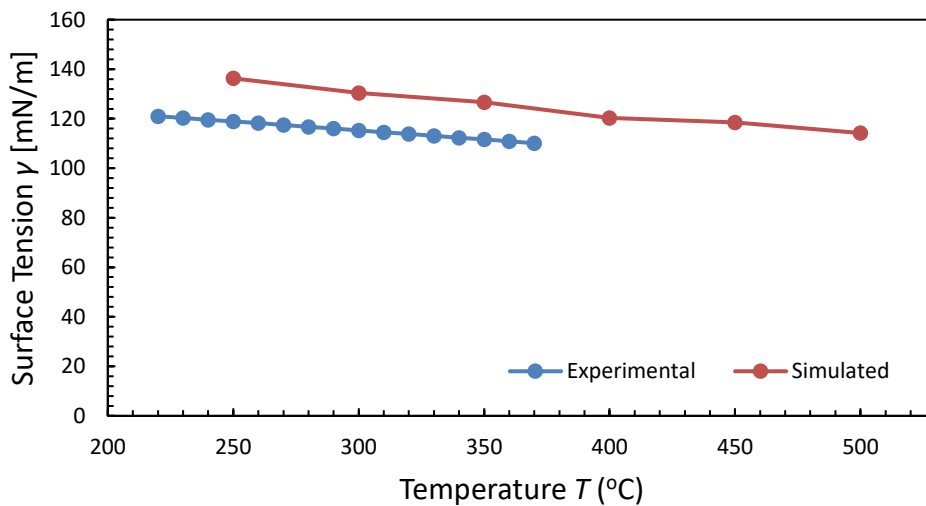


Figure 5.6. Surface Tension of Solar Salt (60% NaNO₃-40% KNO₃), comparison with experimental data¹⁵¹

5.1.4.5 Self-Diffusion Coefficient

In Figure 5.7, the self-diffusion coefficients of the solar salt are compared between experimental measurements and calculated values. Although the trends are similar, there is a more significant variation between measured and calculated values for the self-diffusivity than for other properties. In general, self-diffusivity is a property that is often not very accurate in MD simulations and the average error (94.25%) obtained here is comparable to other simulations ^{159–161}.

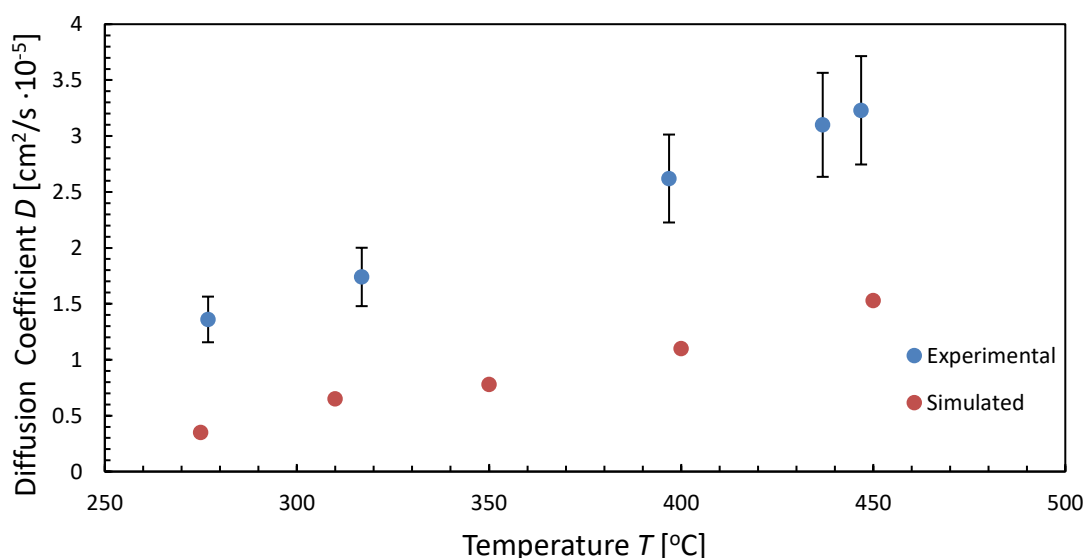


Figure 5.7. Diffusion Coefficient of Solar Salt (60% NaNO₃-40% KNO₃), comparison with experimental data¹⁵⁰.

5.1.5 Novel Lennard-Jones Parameters for simulation of Amorphous Silica

Morse type potentials have been shown to be excellent at predicting the structure of amorphous SiO₂, the transition behavior, the thermal expansion coefficient and also the formulation NPs ¹⁶². The Lennard-Jones and Morse potential are quite similar mathematically. They consist of an electrostatic and a van der Waals contribution. Correlation studies have been conducted, to formulate sets of equations, in order to fit

the energy curves of the two potentials ¹⁶³. In our case we use the Morse parameters provided by Takada ¹⁶⁴, to fit a new set of Lennard Jones parameters capable of simulating the structure of amorphous SiO₂ (Figure 5.8).

For each pair, the critical region is near the point of the potential well. At longer distances, the electrostatic potential prevails, while at shorter distances the two potentials can ‘safely’ differ since the two atoms will never overlap. Root mean square deviations (RMSD) show that a perfect fitting is achieved, with a calculated difference of 0.062, 0.012 and 0.024 (kcal/mole) for Si-Si, O-O and Si-O respectively in the aforementioned range. The list of computed parameters can be found in Table 5.4.

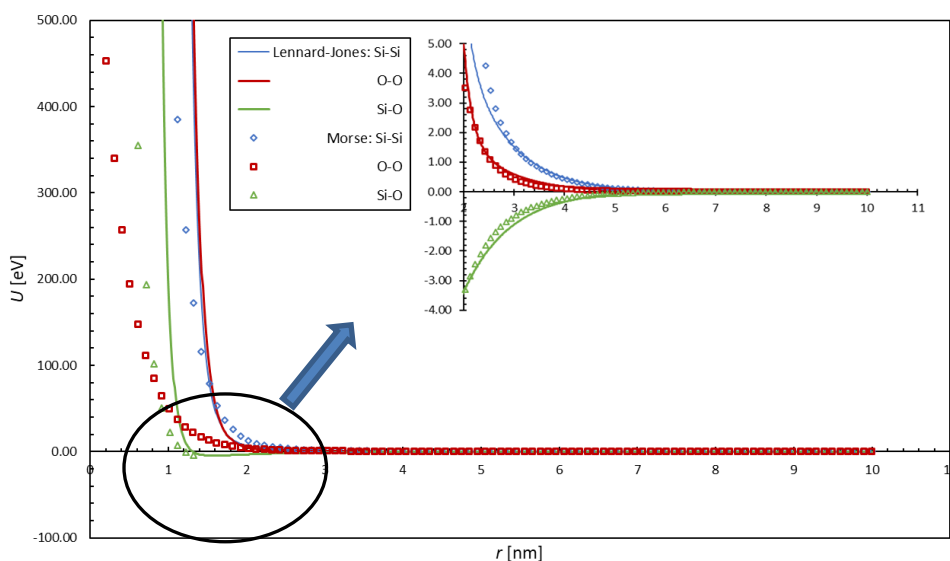


Figure 5.8 Fitting of energy curves between Morse and Lennard-Jones potentials.

Electrostatic interactions are modelled using a pair style coulombic force field and Van der Waals forces using the Lennard-Jones potential.

After the L-J parameters are determined, the accuracy of the potential is assessed by running MD simulations of amorphous silica and comparing the obtained properties with data available in the literature.

Table 5.4. Proposed Lennard-Jones Parameters for Amorphous SiO₂

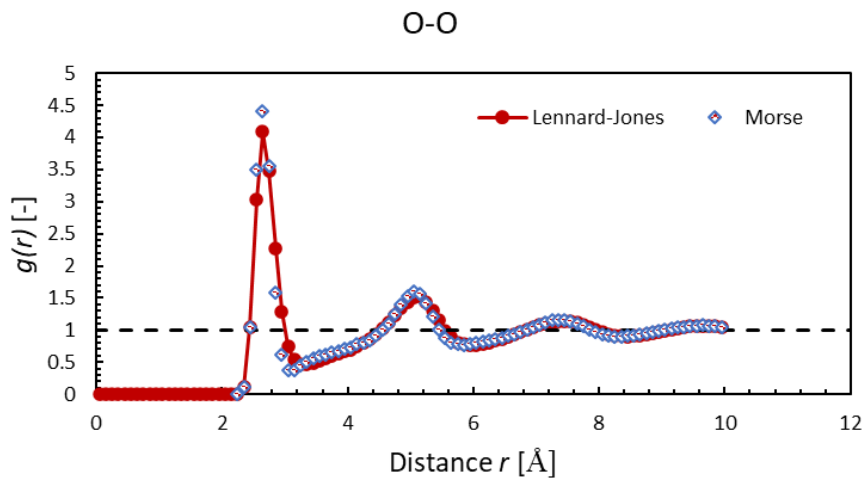
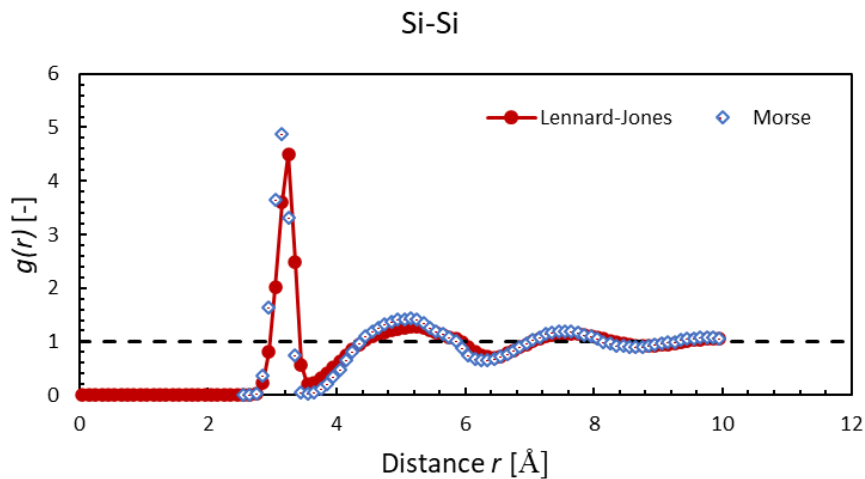
Pair	Q [e]	E [eV]	σ [Å]
Si-Si	1.7	0.0017345	3.2
O-O	-0.85	0.02536852	2.7
Si-O	-	0.000100479	2.95

5.1.6 Amorphous Silica Simulation details

All simulations are performed using the LAMMPS software package ¹²¹. Simulations are conducted starting from the initial structures of α -quartz, obtained by Gibbs et al ¹⁶⁵. A supercell consisting of 80000 atoms is created. Quenching is applied to the initial cell to obtain the amorphous silica. After a Polak-Ribiere structure minimization ¹⁴⁴, the system is rapidly heated up from 0 to 4000K for 0.3 ns, in the NVT ensemble using a Nose-Hover thermostat and barostat ¹⁴⁵. Subsequently, it is equilibrated at 4000K for 2.0 ns in the NVT ensemble followed by a slow cool down up to the melting point in the NPT ensemble with a quenching rate of 1.0 K/ps ¹⁴⁶. The final structure is obtained by further relaxing the system in the NVT ensemble for 2.0ns. The cutoff of the interatomic potential is set at 10Å, with long-term and columbic interactions being computed using Hockney's Particle-Particle Particle-Mesh (PPPM) method ¹⁴⁷. The equations of motions are solved using the Verlet leap-frog algorithm ¹⁴⁸. In all simulations, the timestep is set to 0.001ps. Periodic boundary conditions are applied.

5.1.7 Prediction of the Local Structure of Amorphous Silica

To validate the new set of parameters. The equilibrated local structure is studied and compared with results obtained from simulations conducted with the original Morse parameters. Specifically, the radial distribution function (RDF), bond distribution, angular distribution function (ADF) and coordination number are plotted (Figure 5.9).



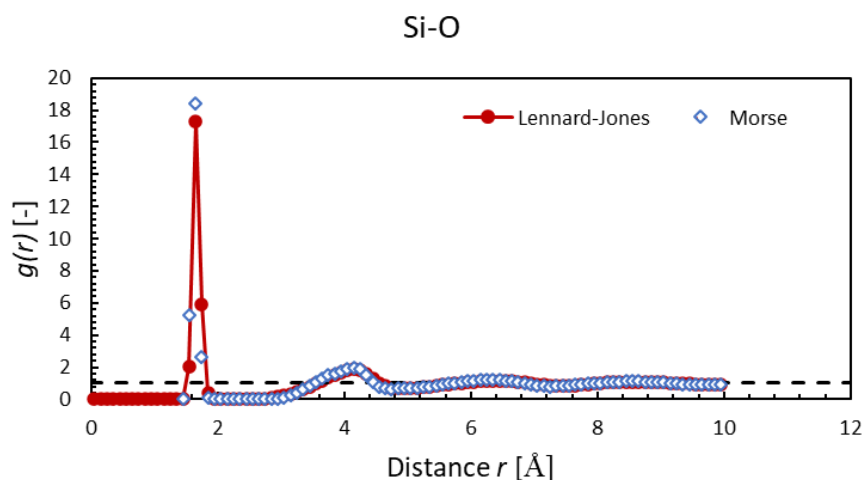


Figure 5.9 Radial Distribution function of amorphous SiO₂, comparison between Morse (red) and Lennard-Jones (blue) potentials.

RDF shows excellent accuracy in the predicted local structures (Figure 5.9). The positions of the first and second peaks of Si-Si, O-O and Si-O in the RDFs represent the first and second nearest neighbor distances the interatomic pairs. The first peaks are at 2.65, 3.25 and 1.65 Å for Lennard-Jones and 2.65, 3.15 and 1.65 Å for the Morse Force-Field. The Si energy curve with the highest difference in the fitting process, shows a minor shift of 0.1 Å in the resulting structure.

Since, the force-fields used in this study contain no intramolecular parts, the bonds and angles in amorphous SiO₂ are represented by means of Van der Waals interactions. Therefore, the mean bond distance, the ADF and the coordination number were all computed, for both the Morse and Lennard-Jones force fields, to ensure the structure is correctly predicted.

The bond length in amorphous silica are between Si-O pairs. In the bond distribution figure (5.10), it can be seen that the length of bonds ranges from 1.52 to 1.85 Å. In the

case of the Morse potential, the mode of the bond length distribution is at 1.66 Å, while in the case of the Lennard-Jones that is 1.67 Å. Experimentally, the average value is 1.618 ± 0.02 Å¹⁶⁶.

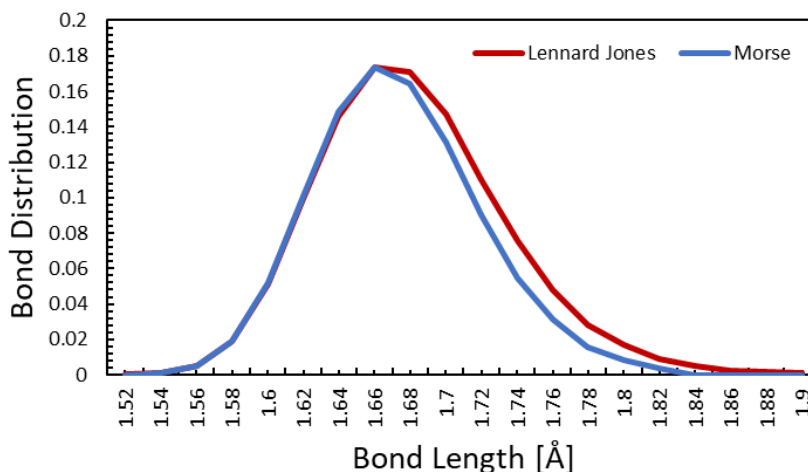


Figure 5.10 Si-O bond length distribution in amorphous SiO₂, comparison between Morse (red) and Lennard-Jones (blue) potentials.

Validation of a structure can be further achieved via coordination number curves. In amorphous SiO₂, the average coordination number is measured to be $Z_{Si-O} = 4$ and $Z_{O-Si} = 2$ ¹⁶⁷. This means that each silicon atom is surrounded by 4 oxygen atoms, while an oxygen atom is surrounded by 2 silicon atoms. In both models, coordination numbers are almost perfectly predicted (Figure 5.11). A minor fraction of the system stoichiometry, does not coincide with the measured values, leading to minimal structural defects (<4%). Further equilibration, typically eliminates these issues¹⁶⁸.

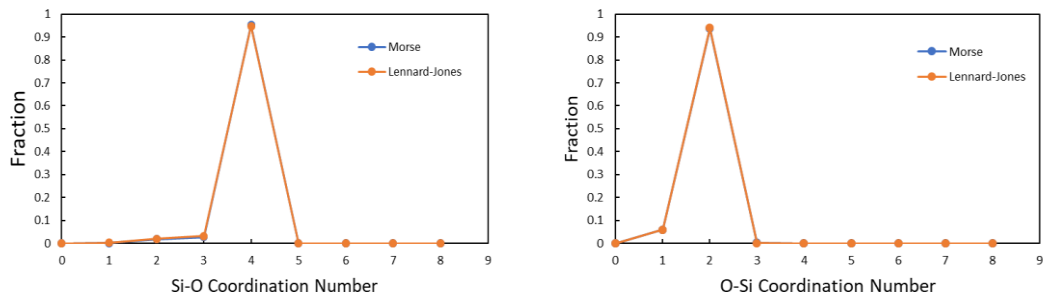


Figure 5.11 Si-O and O-Si coordination number distributions in amorphous SiO₂, comparison between Morse (blue) and Lennard-Jones (orange) potentials.

The most important angles present in amorphous SiO₂ are the O-Si-O and the Si-O-Si angles. From X-Ray diffraction these angles have been measured to peak at 109.47 and 150 ° respectively (the later peak observed mostly at 152 and secondarily 144 °) ^{167,169} . The Morse potentials predicts the O-Si-O angle to peak 109.0 °, while the Lennard-Jones predicts the highest peak at 109.5 °. In the case of the Si-O-Si, the angles are 150 ° and 155 ° for Morse and Lennard-Jones respectively (Figure 5.12). This is in agreement with another study by Kaliannan et al. using the Morse force-field ¹⁶⁸ . The angles were calculated to be 109.5 ° and 159 ° respectively.

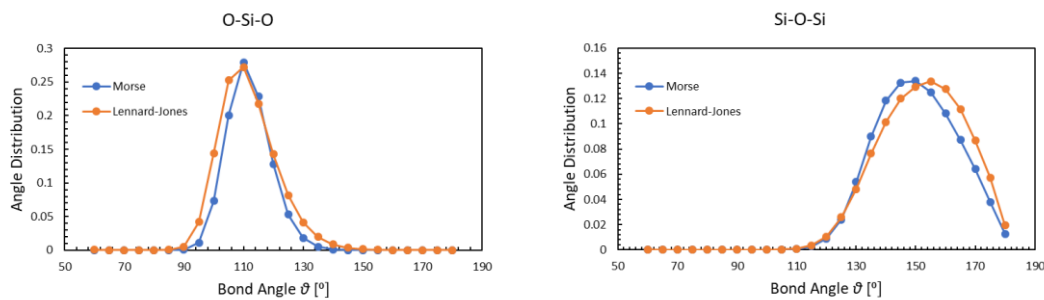


Figure 5.12 O-Si-O and Si-O-Si angular distribution in amorphous SiO₂, comparison between Morse (blue) and Lennard-Jones (orange) potentials.

5.1.8 Prediction of Bulk Properties of α -SiO₂

Besides local structures, density, thermal expansion coefficient and thermal conductivity of amorphous SiO₂ are also calculated and compared with experimental

data. The following equations are used for the calculation for density and thermal expansion coefficient, respectively. The methodologies used to calculate these properties are explained in detail in section 3.4.2.

Predicted values are found to be in very good agreement with respect to density, while in the case of the thermal expansion coefficient the difference is higher, but closer than the Morse potential (Table 5.5).

Table 5.5 Comparison of calculated density and thermal expansion coefficient of Amorphous SiO₂, with Lennard-Jones and Morse potential, with experimental data ¹⁶⁸.

Property	Lennard-Jones	Morse	Experiment
Density (g/cm ³)	2.212	2.206	2.20
Thermal Expansion Coefficient (1/K)	3.2 - 7.15 x 10 ⁻⁶	5.34 - 9.87 x 10 ⁻⁶	0.543 x 10 ⁻⁶

Overall, the calculated local structural parameters, as well as the density and thermal expansion coefficient appear to be in excellent agreement not only between the two interatomic potentials, but also with experimental data provided by the literature.

5.1.9 Summary

In this section, an original set of Lennard-Jones parameters are presented capable of accurately representing the behavior of pure molten NaNO₃ and KNO₃ and their mixtures and α-SiO₂ throughout the temperature range typical in solar applications.

The simulated local structures of pure NaNO₃ and KNO₃ are in good agreement with those obtained in a previous study on the same materials using the Buckingham

potential. Furthermore, the simulated transport properties (density, thermal conductivity, viscosity), as well as surface tension, of both pure molten NaNO_3 and KNO_3 are investigated.

In terms of $\alpha\text{-SiO}_2$ the potential is validated, in terms of structural properties, density and thermal expansion coefficient with results obtained with the Morse potential and with experimental data and found to be in excellent agreement in all cases.

Atomic interactions are of high importance and effectively govern the behavior at the interface of materials. A set Lennard-Jones parameters, such as the ones presented in this section can provide essential contribution. This is due to validated existing techniques, for cross-term interatomic parameters computation, that the Lennard-Jones potential provides. Examples of such trending scenarios are in molten salt-nanoparticle systems, where the nanoparticle-salt interface can be investigated and insight in property enchantment can be provided, composite material formulation, where information on the pores and capillary forces can be given and wetting/corrosion phenomena. With MD simulations surface alteration can be visualized in the atomic level. MD simulations can provide a solution, in conditions, where performing experiments can be difficult, expensive and in cases of microstructure analysis, problematic. A simple and computationally inexpensive tool is provided in this work to provide answers to the aforementioned problems.

5.2 Application of the new Force-Field parameters in Molten Salt/Nanoparticle interface.

Molten salts are most commonly used in concentrated solar power (CSP) plants primarily as an energy storage solution and secondarily as heat transfer fluids. Their main advantages are their large temperature operating range, thermal stability and low vapor pressure. Their most important drawback is their poor thermal properties. To counter this, metal oxide NPs are suspended in molten salts ²⁰. The resulting mixture is named molten salt nanofluid (MSNF). MSNF are of special interest in the solar energy scientific community due to the increments reported in both thermal conductivity and specific heat capacity. The magnitude of this enhancement is still controversial. Conflicting results of properties measurements are yet to be explained ²⁷. Furthermore, addition of NPs has a significant effect not only on the thermal, but also on the transport properties of the base fluids ¹¹.

Qiao et al. ⁹⁸ calculated specific heat capacity using MD simulations, and their results show an enhancement in specific heat capacity in the presence of NPs, in accordance with experimental measurements. In a subsequent study, it was shown, that NPs induce a change in the ordering of the molten NaNO_3 , which creates a compressed layer along the interface ⁹⁹. Jo et al. calculated the effect of the thickness of this layer in a molten carbonate-CNT system, as well as the effect of the change of composition in the density of the produced layer ¹⁷⁰. No studies, however, have been conducted to date, confirming the existence of this layer in mixture of molten nitrate salts in the presence of NPs.

To better validate the parameters presented in this study a molten nitrate salt-amorphous SiO_2 system is simulated in order test the capability of the new force-field

to reproduce an accurate representation of the ordering of the molecules in the nanoparticle-salt interface.

The following simulation focuses at the nanoparticle/molten-salt interface. Two separate simulations are first conducted. One involves the equilibration of a 6nm block of amorphous silica. The second the equilibration of a solar salt mixture, in a simulation of domain where the axes lengths are $x = 5 \text{ nm}$, $y = 5 \text{ nm}$ and $z = 50 \text{ nm}$. The interaction parameters for the solar salt (60% NaNO_3 – 40% KNO_3) are taken from a previous study ¹⁷¹. The SS is chosen because it primarily used heat transfer and energy storage material in the CSP industry ¹⁷². The two equilibrated systems are then merged. The block of amorphous SiO_2 is placed on the one end of the simulation domain. On the other side of the simulation domain, the z -axis is further extended to avoid periodicity issues (Figure 5.13). The timestep is set at 0.0005 ps and the cutoff-radius at 1.5 nm. The molten salt-nanoparticle system is then equilibrated in the NVT ensemble for 50ns, after which the structure is studied. The system consists of 16800 SiO_2 and 56035 molten salt atoms.

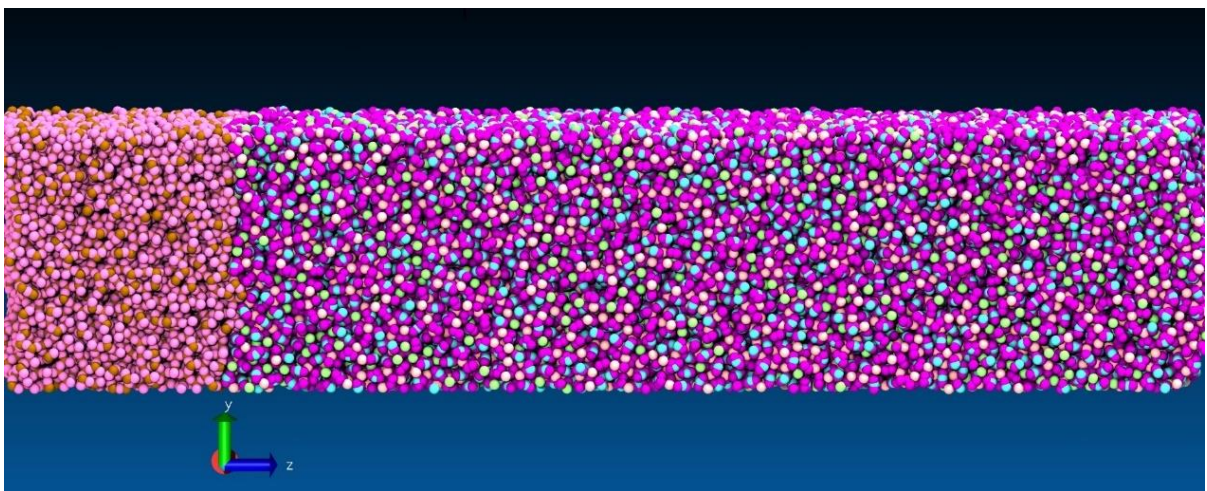


Figure 5.13 Molten solar salt (right) placed on top of an amorphous SiO_2 block (left).

The density of the SS in the liquid-solid interface, is 6.5% higher than its bulk value (Figure 5.14). This indicates the existence of a compressed layer of liquid molecules at the salt nanoparticle interface. The thickness of the compressed layer appears to be roughly 18 Å. After a distance of 30 Å from the NP surface, the density of the solar salt is normalized and fluctuates around the experimental value.

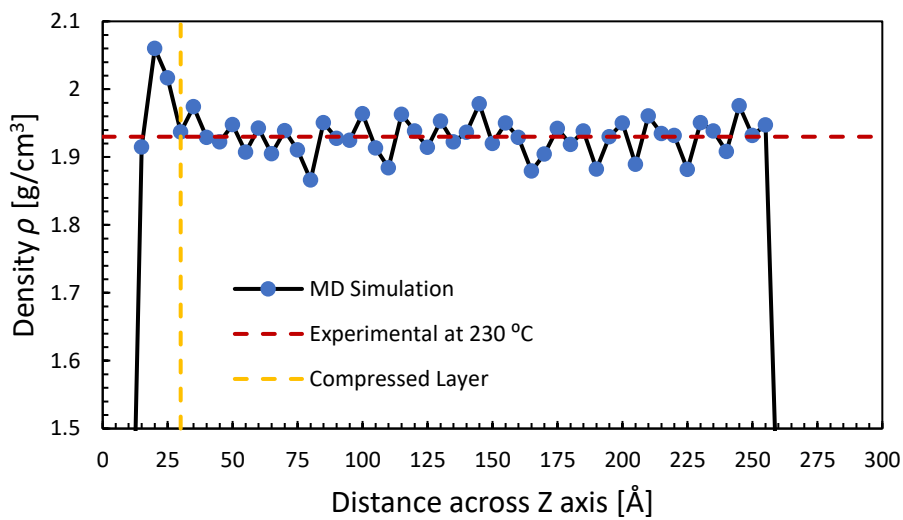


Figure 5.14 Molten solar salt (right) placed on top of an amorphous SiO₂ block (left). Experimental density from Janz et al (1981)¹⁵⁸.

Self-diffusivity D of the salt is calculated at different distances from the interface. The self-diffusion coefficient D is obtained from the slope of the linear regression of the mean squared displacement $\langle r^2 \rangle$ in the diffusive regime. The slope is then divided by a factor of 6 according to the Einstein formulation¹⁷³. It should be noted that in this study center of mass corrections are applied. Previous studies have shown that hydrodynamic interactions in a simulation with periodic boundary conditions lead to changes in the diffusion coefficient due to finite size effects¹⁷⁴. Artifacts produced from this are accounted for correctly. The formalisms behind these calculations are explained in section 3.3.2. The molten salt molecules are then divided in groups in

cubic regions of 50 Å. The values of the viscosity were taken from previous work ¹⁷¹. Mean atom displacement values are sampled for 10ns.

The self-diffusivity in the proximity of the interface is calculated to be significantly lower than in the bulk (Figure 5.15). This shows that the addition of NPs limits the mobility of atoms in the vicinity of the interface.

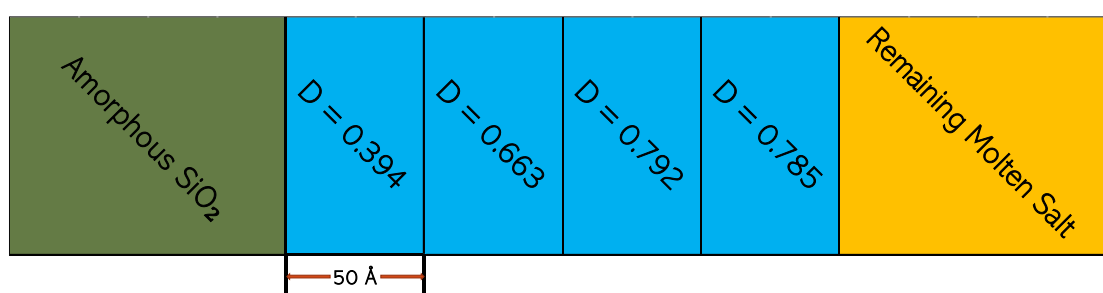


Figure 5.15 Self-diffusivity coefficients of molten salt calculated in each region. Units are in $\text{cm}^2/\text{s} \times 10^{-5}$

Additionally, RDFs, between the Na⁺, the K⁺ and the silica NP show a distinct peak that denotes a layering at the salt-nanoparticle interface (Fig. 5.16). This was also mentioned for the case of sodium by Qiao et al. ⁹⁹. The results obtained in this work suggest the existence of an almost solid-like layer with higher density and lower self-diffusivity close to the interface. which is one of the mechanisms proposed in the literature to explain the unconventional thermal enhancement ⁹⁸. Furthermore, the Na⁺ and K⁺ peaks differ in terms of distance from the surface, which implies that two of such layers (one richer in Na⁺ and another richer in K⁺) are formed in the vicinity of the amorphous interface. Since, the two salts possess most notably different melting points (308 and 335 °C for NaNO₃ and KNO₃ respectively), and secondarily properties (i.e. thermal conductivity, self-diffusivity), the existence of distinct ion separation in the

vicinity of the surface, could be closely related to firstly the reduction of the melting point of molten salts in the presence of NPs and the subsequent changes observed during the phase transition in eutectic mixtures of molten salts ¹¹. How that interplays in the enhancement of the specific heat capacity, is still in question ¹⁷⁵.

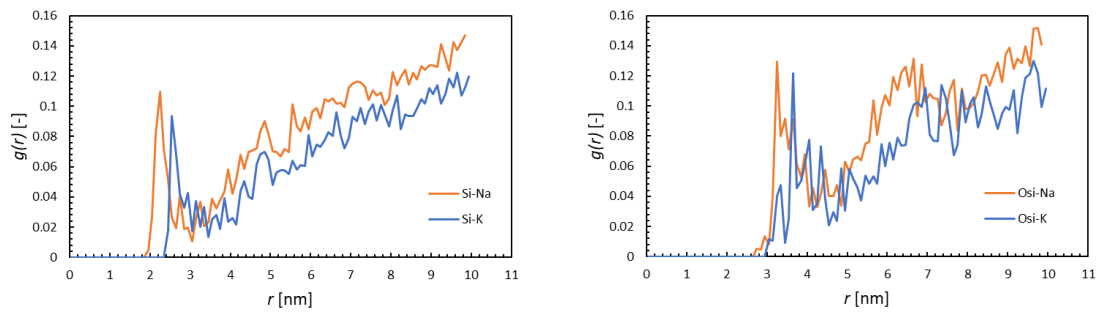


Figure 5.16 Left: Sodium and potassium interactions with silica (Si-Na, Si-K). Right: Sodium and potassium interactions with oxygen in silica (Osi-Na, Osi-K).

Jo et al ^{176,177} previously suggested that the existence of this layer could affect the specific heat capacity of the molten salt nanofluid. In a subsequent work they studied the thickness of the compressed molten salt layer and calculated its density. They related the thickness and density of the compressed layer to the molar composition of the liquid (their studies were conducted on a Li+, K+ carbonate eutectic mixture). Mixtures with higher percentage of potassium, showed a denser interfacial layer with a sharper thickness, while in compositions with lower potassium concentrations the opposite was observed. It is believed that the intramolecular interactions of the lesser sized ion (in this case Na+) cancel out, to an extent, the existence of this layer ¹⁷⁰. Their smaller size leads to a larger degree of freedom, which enables the displacement of atoms in the interfacial region, thus relaxing the solid like structure. In this study the potassium is the lesser element in terms of molar fraction and as expected the density increase in the vicinity of the interface is marginal.

The above structural observations indicate that the potential parameters proposed in this study function correctly in complex systems and are able to accurately reproduce the effect of cross-term interactions between the salt and the NP surface. Study of the structure in the proximity of the interface suggests that the change in the phase transition and the specific heat capacity obtained by adding NPs into the solar salt could be related to the formation of this ordered double layer and the change in the ion displacement and arrangement observed in the vicinity of the NP interface. Further investigation is required to identify the effect of this double layer as well as its molar compositions on the thermal properties molten nitrate mixtures doped with NPs.

5.3 Wettability of NaNO_3 and KNO_3 on MgO and Carbon Surfaces – Understanding the Substrate and the Length Scale Effects

5.3.1 Introduction

In this section, the CA of molten salts is investigated via Molecular Dynamics (MD) simulations. Due to the high melting point of the materials, as well as the demanding atmospheric conditions (inert gas and high vacuum to ensure complete absence of oxygen) involved in CA measurements (i.e. inert gas atmosphere), experiments with molten salts are difficult to conduct, and therefore, MD simulations are a valuable alternative for providing insight into the wetting behavior between materials. The concepts of surface tension and contact angle are not entirely rigorous when dealing with nanosized droplets and surfaces. Nanodrops below a certain dimension and a length scale of surface texture (roughness) become highly dependent on molecular interactions¹⁷⁸. Nonetheless, for nanodrops exceeding a few tens of Angstroms, despite the uncertainty of the Tolman length¹⁷⁹ and its effect on the line tension, MD

simulations of spherical cap droplets and cylinders are typically regarded as a valid method to assess the surface wettability of a fluid⁸⁵.

In this section the CA between the salts and the two materials (MgO, graphite) calculated by means of MD simulations and then compared with experimental measurements. The results are compared to provide a validated a modelling approach for predicting the CA of molten salts on various surfaces, thus helping to create a rapid non-experimental pathway to screen material suitability for synthesis of molten salt ceramic composites, before embarking in complex experimental analysis.

Simulations were conducted on the HPC Midlands Plus cluster computer. It consists of 512 nodes with 28 cores in each node that are Intel Xeon E5-2680v4 at 2.40 GHz (base). A typical MD simulation involves 1000 atoms/CPU. A 10nm droplet consists of 6000 salt atoms and 12000 substrate atoms. To ensure optimal speeds 28 cores were used. Using less than 100 atoms/CPU is non-optimal. However, anywhere between 1000 and 100 atoms/CPU is optimal depending on the type of system (i.e. number of atom types, electrostatic interactions etc.). Naturally, processor architecture optimization commands were also used to ensure an optimal simulation, both in terms of LINUX commands directly on the cluster, but also through some commands in the LAMMPS software. For the 10nm droplet to reach equilibration 25ns were required. Simulations at optimal speeds achieved performance rates of 2.425 ns/day. Typically, for smaller systems performance is even higher and can even reach 25 ns/day, while the opposite is true for very large simulations. For example, a system of 250 cores (with 250 thousand atoms) achieved a speed of 0.311 ns/day on the same cluster. Of

course, there are methods to further accelerate these systems by using GPU CUDA cores, which have optimal parallel processing architecture. Nevertheless, one can obtain a reasonably good estimate of the wettability of a molten salt in a time frame of a week using a small cluster computer with 28 cores.

5.3.2 Simulation details

The Buckingham potential is often chosen for the simulation of molten salts. However, due to the absence of mixing rules and hence the difficulty of calculating the cross-term interaction parameters, which are key in wetting interactions, the Lennard-Jones plus Coulombic potential is used in this study for the interatomic interactions.

Numerical values for the interatomic, electrostatic and intramolecular parameters used in this study are provided in Tables 5.1. MgO and C parameters are taken from the literature^{180,181}, while those for the molten nitrate salts are those listed in section 5.1.3¹⁷¹.

Quenching is applied to obtain the structure of the molten salt. The crystalline cell structures of NaNO₃ and KNO₃ are acquired from Gonsoerk et al and Adiwidjaja et al. respectively^{142,143}. They are replicated in all dimensions and transformed into a periodic boundary box, roughly equal in all dimensions. In both cases the system is rapidly heated from 0 to 1200K in the NVT canonical ensemble in 0.2 ns, after which, it is equilibrated at 1200K for 0.5ns. It is then slowly cooled in the NPT ensemble from 1200 K to the desired temperature for 2 ns, followed by equilibration in the NVT ensemble for 0.5 ns, to obtain the desired structure.

The obtained structures are then placed on top of a (1 1 0) MgO slab with the help of VMD TopoTools¹²². The simulation box is periodic in all dimensions, with the dimensions of the box being those of the MgO slab in the x and y axis and double in the z direction (Figure 5.18). The kinetic energy of the slab's atoms is assessed at the beginning of the simulation according to the initially assigned temperature. During the simulation, however, the positions and velocities of these atoms are not updated to save computational time. The same approach is used also in the case of the graphite. This has been proposed and demonstrated for carbon atoms by Koumoutsakos et al⁷⁵, who showed that thermostating the slab atoms throughout the simulation does not affect the resulting contact angle, but significantly reduces the required computational time. The system is simulated in the NVT ensemble for 20 ns. Data collection is conducted in the last 5ns. The thermostat is applied only to the liquid¹⁸².

Unlike the case of the MgO, the graphite surface is characterized by much higher roughness. As mentioned, roughness can significantly affect the CA of a liquid on a surface (Section 2). From the roughness measurements conducted in this work, the S_{dr} (developed interface ratio), is also calculated. This parameter is used to account for the roughness in the Wenzel and Cassie-Baxter equations. The S_{dr} is the ratio of the real measured area of a surface to the projected area of an ideal smooth surface¹⁸³. Since it is a ratio and thus a dimensionless parameter it can be used to link the roughness of a macroscopic to a nanoscale surface as it is independent of scale. Thus, the measured S_{dr} values of the graphite surface that is used in the experiments are used to design the molecular surface for the MD simulations. Although the surface of the graphite has a non-consistent pattern, here a texture type of rough surface is

assumed¹⁸⁴. The flat smooth-edged surface consists of isotropic cuboid posts as shown schematically in Figure 5.17. The side and the top of the pillars have identical properties to the graphite surface below them. Lundgren et al., in their work examined the sensitivity of the CA of a hydrophobic liquid with respect to the pillar height. They identified that above a pillar height (h_p) of 9 Å, the calculated value of the CA becomes stable¹⁸⁵. The height is therefore selected accordingly. Regarding the spacing between pillars (S_p), the authors showed that by increasing the gap between the pillars the droplet shifts towards a Wenzel state, while if the gap is reduced it shifts to a Cassie-Baxter state. In this study, since the experimental measurements show a clear hydrophobic behavior by the graphite, and thus a Cassie-Baxter state, the gap is adjusted accordingly. The above observations are also verified by Yaghoubi et al., who further noted that when the pillars exceed a certain height (roughly 10 Å), increasing their width has no effect on the wettability and the nanodroplets remain in the Cassie-Baxter state¹⁸⁶. Finally, the graphite face selected is the (1 1 1), which has been proven to accurately predict the CA of water^{75,187}.

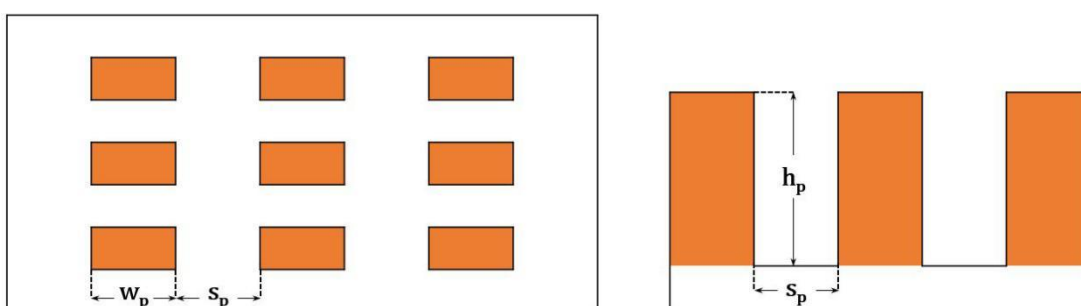


Figure 5.17 Schematic description of the texture rough surface formed with square pillars. The left and image depict the top and side view of the surface respectively. W_p is the width and h_p the height of the pillar. S_p is the distance between pillars.

Simulations of the two molten salts inside a single-wall carbon nanotube (CNT) are also conducted. The CNT is created by the Nanotube Builder plugin builder available in VMD. The salt is first simulated outside the CNT and compressed to the desired CNT diameter using a cylindrical indenter for a total time of 20 ps. Subsequently, the salt is displaced inside the CNT (the indenter is removed), where it is equilibrated in the NVT ensemble for 30 ps. The thermostat is then removed, and the system evolves in the NVE ensemble for another 30 ps, after which the contact angle and density of the salt inside the CNT is sampled for 20 ps.

All simulations are performed with a timestep of 0.0002 ps. Particle-Particle Particle-Mesh (PPPM) solver is used to calculate the long-range electrostatic interactions with accuracy of 10^{-5} ¹⁴⁷. For the simulations of the molten salts on the surfaces the cutoff is set at a value 5 times the equilibrium separation of the molten salt with the MgO and the graphite respectively. This is conducted in order to avoid any artificial wetting due to a small cutoff value¹⁸².

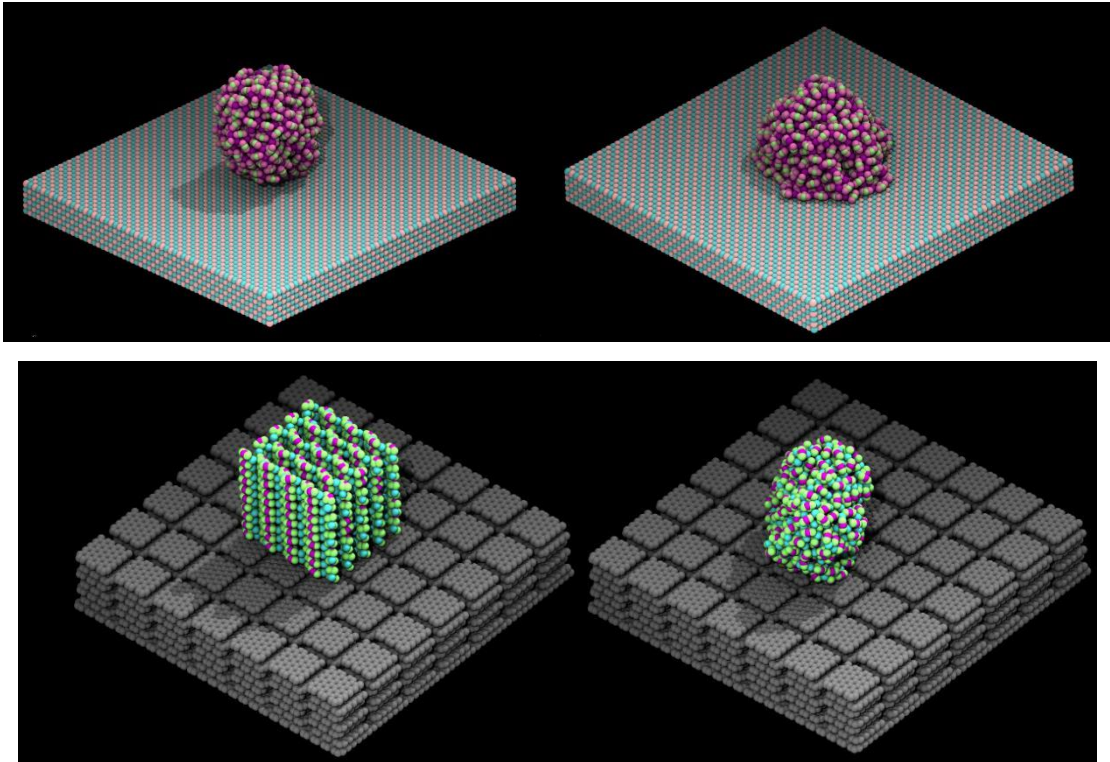


Figure 5.18 Molten salt placed on the MgO substrate (top row) and on graphite (bottom row): screenshots at the beginning (left column) and at the end of the simulation (right column).

Topology information is extracted every 1000 timesteps and post-processed in MATLAB to calculate the CA. The methodology for calculating the CA is described in Kalali et al ⁷⁴ and is based on ‘coarse-graining’ the density from the instantaneous atomic coordinates . The liquid-vapor interface of the drop is defined as the point, where the coarse-grain density is equal to half of the bulk. Angles between the unit normal vectors to the average LV interface and unit normal vectors to the solid surface are calculated as a function of the distance normal to the solid surface. The CA is then estimated by extrapolating the cosines of the obtained angles to the triple-phase CA. The value of the CA is calculated by averaging the last $2 \cdot 10^5$ timesteps.

The CA is calculated using the modified Young's equation to account for the size dependence of the wetting behavior in the nanoscale¹⁸⁸:

$$\cos\theta = \frac{\gamma_{SV} - \gamma_{SL}}{\gamma_{LV}} - \frac{\tau}{\gamma_{LV}R} = \cos\theta_{\infty} - \frac{\tau}{\gamma_{LV}R}, \quad (5.2)$$

where, θ is the equilibrium contact angle obtained from the simulations; the subscripts in γ stands for the surface tension of three different interfaces: SV solid–vapor, SL solid–liquid, and LV liquid–vapor, R is the radius of the CA obtained from MD simulation, θ_{∞} is the equilibrium contact angle of a macroscopic drop (in our case the experimental measurements), and τ is the line tension.

The actual value of the line tension is still debated. Its value in the literature spans 7 order magnitudes depending on the system studied and the approach¹⁸⁸. Studies, have shown that its magnitude depends on the size of the droplet¹⁸⁹. This would be consistent with the fact that data obtained by MD simulations have significantly lower values⁷⁷ than those obtained by experimental measurements¹⁹⁰. Furthermore, the sign of the line tension (positive or negative) is also still in question⁷⁷. Most studies involve organic materials and most commonly water. No studies have been conducted on the calculation of the value of the line tension for molten salts. In this work, the procedure suggested by Jaffe et al. is followed¹⁹¹ for calculating the line tension. This method is based upon the calculation of the cosine of the CA ($\cos\theta$) in several MD simulations with drops of different radii of curvature, as well as the value of the cosine of the macroscopic drop ($\cos\theta_{\infty}$). After obtaining the value of all variables in Eq. (5.2)

the line tension τ is averaged for different system sizes. In this work, droplets ranging from 4.6 (2000 atoms) to 20nm (67000 atoms) are investigated.

The effect of droplet size is also considered in the calculation of the surface tension. Surface tension is essentially the macroscopic manifestation of cohesion forces on liquids. For interfaces with a small radius of curvature R , the surface tension of a liquid differs from its bulk value ¹⁹². The drop length dependent value of the surface tension is given by the following approximate formula given by Tolman¹⁹³:

$$\frac{\gamma(D)_{LV}}{\gamma_{LV0}} \approx 1/1(1 + \frac{4\delta}{D}) \quad (5.3)$$

Where $\gamma(D)_{LV}$ denotes the value of the liquid vapor surface tension due to its dependency on the size of the droplet in the nanoscale, γ_{LV0} is the bulk surface tension value of the liquid, δ is a constant length commonly referred to as the Tolman length and D the diameter of the droplet.

The Tolman length is obtained from the thermodynamic relation involving the isothermal compressibility of the liquid, originally proposed by Bartell¹⁹⁴ and revisited by Blokuis and Kuipers¹⁹⁵

$$\delta \approx -\kappa_l \sigma \quad (5.4)$$

where δ is the Tolman length, κ the isothermal compressibility of the liquid and σ the surface tension. Data regarding the isothermal compressibility of the two molten salts are obtained from Marcus (2013) ¹⁹⁶.

Based on the above equations the dependence of the surface tension on the size of the droplet is plotted in Figure 5.19. The values plotted refer to the melting temperature points of the liquids; minimal differences are observed at higher temperatures, as the values of the surface tension are almost constant with temperature. For drops above 3 nm, the surface tension reaches the bulk value. Therefore, the MD simulations are conducted for systems larger than this size.

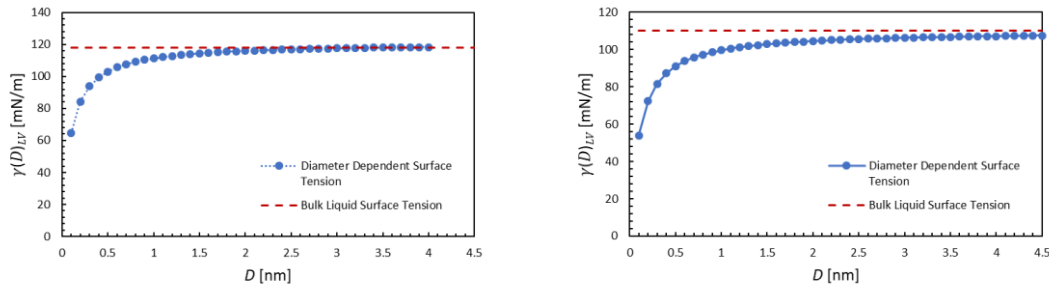


Figure 5.19 Effect of drop diameter on surface tension of molten NaNO_3 (right) and molten KNO_3 (left).

To reduce the effect of the surface tension on nanoscale systems of spherical caps, MD simulations of wetting on surfaces a cylindrical geometry has been also used⁷⁸. In theory, with this approach, the line tension effect is reduced due to the periodicity along one dimension. However, other studies have reported that, even for cylindrical drops, the line tension effect is present in ceramic¹⁹⁷ and carbon surfaces⁷⁶. For comparison, in this study, we also used this method (but only for small systems cylinder radius <4nm).

5.3.3 Experimental Results

CA measurements of the two molten salts on both surfaces can be found in Figure 5. In both cases the CA decreases with temperature (Figure 5.20). This is in agreement with previous studies in molten fluoride salts⁶³. The decrease in the angle presents a linear trend, as the temperature increases. However, the trend in reduction is significantly faster in the case of the MgO and slower in the case of the graphite.

It can be seen that the CA of the both molten salts on the graphite surface is significantly higher than that of the ceramic (Figure 5.20). Generally, much better densification can be obtained if the sintered material is wetted by the liquid solution. A material is considered have good wettability if its CA on the surface is $\geq 90^\circ$. Results from this study on the molten nitrate salt graphite system indicate a poor wettability. Similar measurements have been conducted by Li et al, involving carbonate salts on MgO surfaces with different loadings of graphite⁶². Higher loadings of graphite led to a higher CA. In such systems (of poor wettability) the liquid phase would rather leak out from the sintering die under high pressure, than eliminate porosity¹⁹⁸. In their analyses the authors, suggest that the poor wettability of the graphite can hinder the particle movement inside the composite structure, during the melting and solidification cycles. Generally, if during the liquid-phase sintering, there is a CA transition to the non-wetting range (i.e. $CA > 90^\circ$) the liquid will start to uncover the solid phase thereby creating porosity and a concomitant decrease in density (swelling of the composite), or alternatively move out of the compact structure as a result of mechanical pressure

¹⁹⁹.

Knowledge of the CA can potentially help address these issues during the design phase, through prediction of this type of phenomena by selection of suitable thermal property enhancers, which are predicted to have good wettability with the respective ceramic materials.

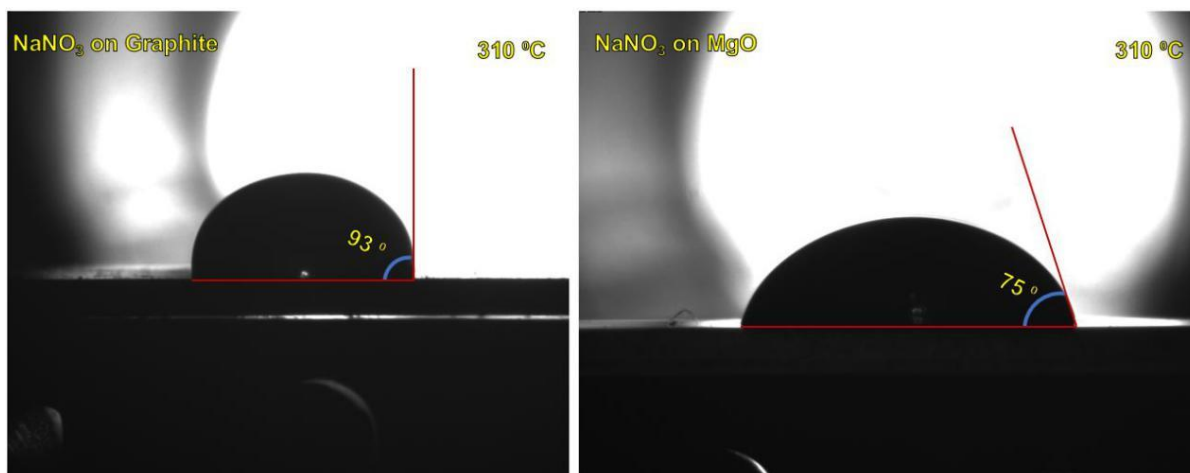


Figure 5.20 Contact angle of molten NaNO₃ on Graphite (left) and MgO {1 0 0} (right).

Additionally, the CA of both salts with respect to time is found to be stable in the duration of the experiments in all cases.

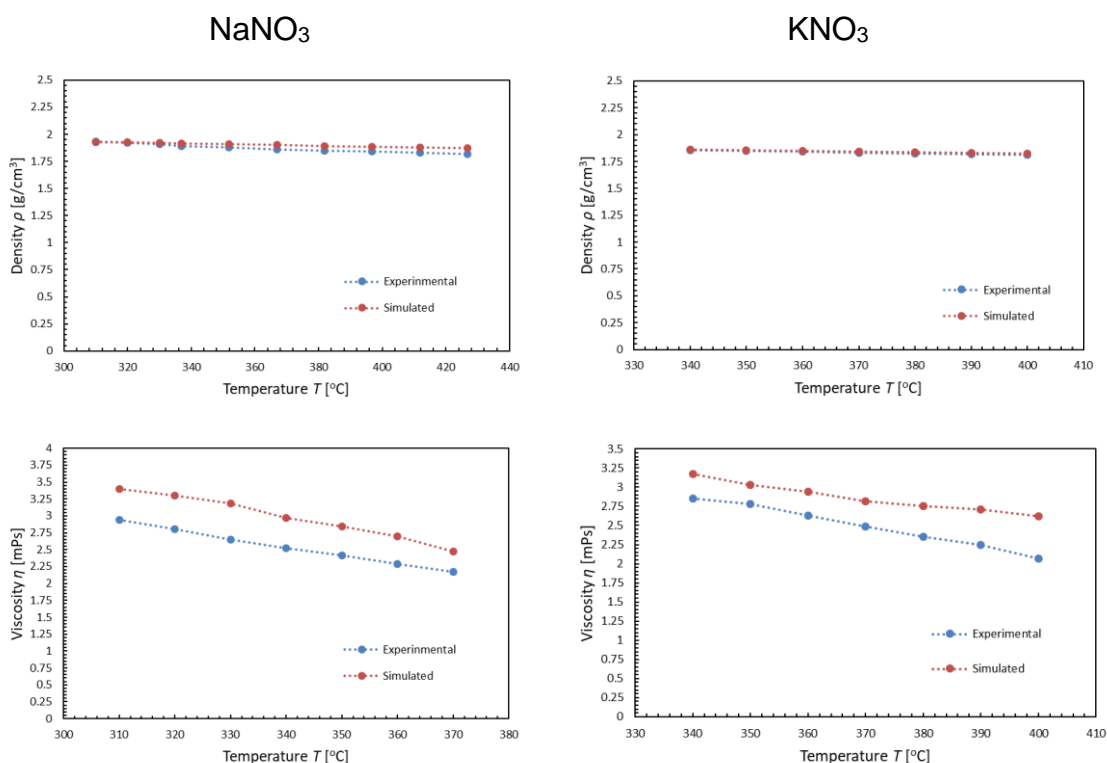
5.3.4 Simulation Results

Before validating the CA results, validation is sought for other molten salt properties such as density, viscosity and surface tension. These, in fact, are all properties, that affect surface wetting and, to ensure that the molten salt interatomic potential used in this study is suitable to study the wetting process, the MD calculations of these properties are also validated with experimental measurements. Density is calculated by dividing the total mass of atoms with the volume of the simulation box, after NPT equilibration. Viscosity is calculated using the Green-Kubo method: the system is equilibrated for 0.1 ns in the NVT ensemble following value averaging for 0.3 ns.

Surface tension is calculated with the Irving Kirkwood method: the system is equilibrated for 0.1 ns in the NVT ensemble following value averaging for 0.3 ns.

5.3.5 Prediction of Molten Salt Properties related to Wettability

Satisfactory agreement between experimental results, from Janz et al. (1972)¹⁵¹, and MD simulations is obtained for all calculated properties (Fig. 5.21). In the case of the density, the overall average deviation from experimental values is around 9%. Viscosity values are in excellent agreement with the experimental values with an average error of around 8%. Surface tension is also in satisfactory agreement with experimental results with an average error of around 11%. Similar overestimations of the surface tension have been observed also in the cases of carbonate salts²⁰⁰.



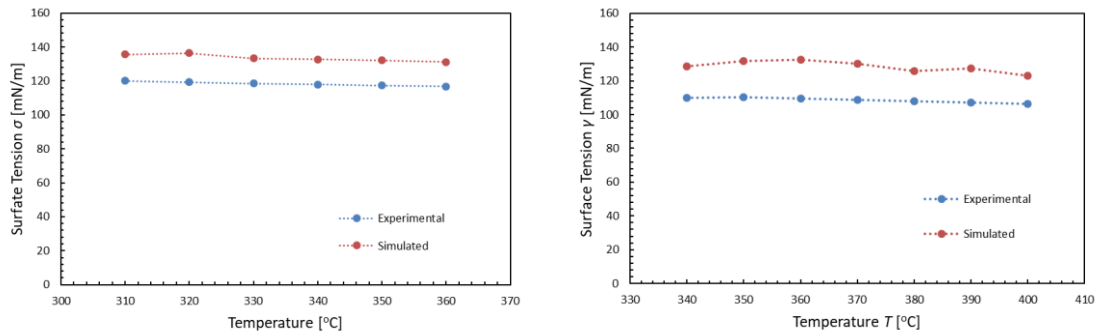


Figure 5.21 Density, viscosity and surface tension of NaNO₃ (left column) and KNO₃ (right column), comparison with experimental data¹⁵¹.

5.3.6 Influence of Drop Size and Temperature

Based on the methodology described in Section 5.3.2, a set of systems consisting of different drop diameters is simulated. The salt atom number ranges from 400 to 65.000 atoms. It should be noted that minimum droplet size is limited by the drop instability issues related to the Rayleigh-Plateau, which leads to fluid thread breakup and subsequent formation of smaller drops²⁰¹. The CA versus the drop diameter and the equilibrated radius of its curvature is plotted in Figure 5.22. As the radius increases the CA of the drop stabilizes. However, a plateau is not observed even at very large drops of 40nm. This is consistent with studies measuring angles of ionic liquids on silicon, and suggesting that the range where a constant CA is observed is typically around 300 nm¹⁸⁸. Additionally, using Equation (5.2), the line tension is found to be ranging between 3×10^{-10} J/m and 4×10^{-11} J/m for NaNO₃ and KNO₃ depending on the system, with the graphite system showing lower values than ceramic. By using the calculated value of the line tension, the macroscopic CA of NaNO₃ on MgO is found to be 70.6 ° using the calculated CA from a system with a drop radius of curvature of 2 nm.

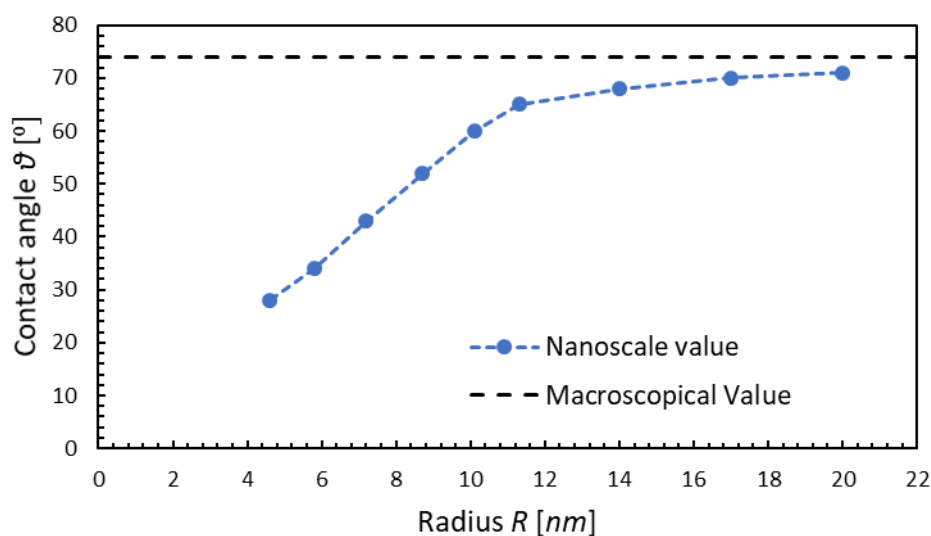


Figure 5.22 Contact angle versus drop radius of curvature R for NaNO_3 on MgO {1 0 0}.

Aside from the simulations in the NVT ensemble (as described in section 5.3.2); a second methodology is also tested for the simulation of the wetting process. The system is first equilibrated in the NVT ensemble for 500ps, after which the ensemble is switched to NVE and the thermostat is removed. The system is then further simulated for 1ns, 500 ps involving further evolution in NVE and the final 500ps sampling of CA values. Significantly high temperature fluctuations are observed. Error accumulation in the NVE ensemble leads to excessive temperature oscillations (i.e. 30K >) during the evolution of the system. Despite trying several thermostats before switching to the NVE ensemble (Andersen, Brendesen, Nose-Hoove and nose-hoover chains), none avoid subsequent temperature increase, upon their removal. Finally, these molten salt systems are found to be highly dependent on atom number and do not equilibrate in 500ps, as often stated in the literature for the case of water. Very long simulations in the NVT ensemble are required to obtain a zero-spreading coefficient (i.e. an equilibrated drop) which typically range between 15 to 20 ns. Moreover, the

equilibration time is found to be independent of the droplet size. This fact has been also observed for water⁸⁰ and ionic liquids¹⁰⁸.

5.3.7 Contact Angle and Work of Adhesion

The correction added by the line tension in the modified Young equation is indeed substantial (section 5.3.5), but nevertheless the difference between the simulated and measured CAs, even for small systems above 6000 atoms, remains in the range of 10° (Figure 5.22). Looking at the wetting behavior of the molten salt on the ceramic surface the observed chemical polarity is clearly positive, and the liquid presents definitively wetting behavior (i.e. the CA is substantially lower than 90°). The CA value obtained from the simulation although not completely accurate is able to capture to a satisfactory degree this behavior. Based on this observation, the CA is calculated at temperature intervals of 10°C , between 310 and 400°C (Figure 5.23) for the molten NaNO_3 and 340 and 390°C for KNO_3 using a 12nm radius droplet (6.000 salt atoms). The fluctuation of the temperature is within 5K . The model correctly predicts, even without accounting for the line tension, the wetting behavior of molten NaNO_3 and KNO_3 on the MgO and graphite surfaces. It should be noted that the CAs presented are the instantaneous CA values measured in the experiments. These have been found to be stable with time in the duration of the experiments. The final equilibrated value of the CA is impossible to obtain through MD simulations of CA and can only be obtained from free energy sampling with long durations.

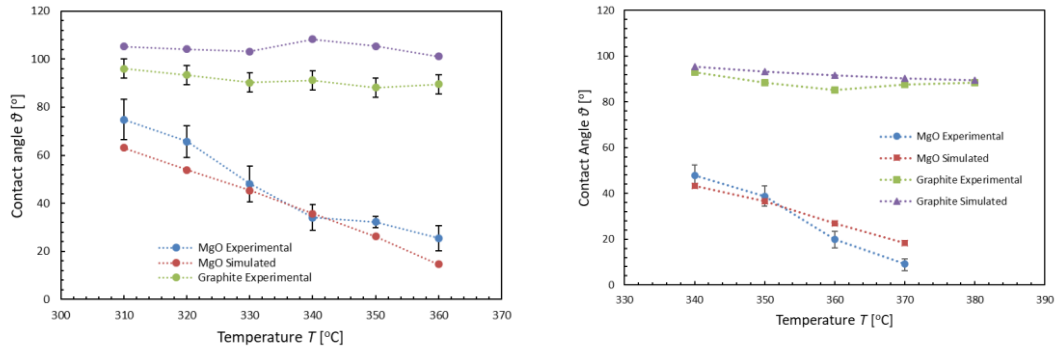


Figure 5.23 Contact angle of NaNO₃ (left) and KNO₃ (right) on MgO and graphite. Comparison with experimental data.

The work of adhesion W_a is also calculated using the Young-Durpe equation

$$W_a = \sigma_l [1 + \cos(\theta)] \quad (5.5)$$

where, σ_l is the liquid surface tension and θ the liquid-solid CA. Often, in MD simulations, the work of adhesion is computed by means of free energy calculations with 3 independent simulations, but this approach has been found to have the same accuracy of the simple Young-Durpe equation²⁰².

The MD simulations show, a reasonable agreement with the experimental data with an average error of around 12% and 15% for the NaNO₃ and KNO₃ respectively. Since, the work of adhesion of the molten salt is much higher on the graphite surfaces, the presence of the graphite is a barrier to the effective sintering of the mixture, as suggested in the literature^{56,61}. It should be noted that the CA values used to calculate the work of adhesion through Eq. (5.5) are these presented in Figure 5.24 and not those obtained from Eq. (5.2) accounting for the line tension.

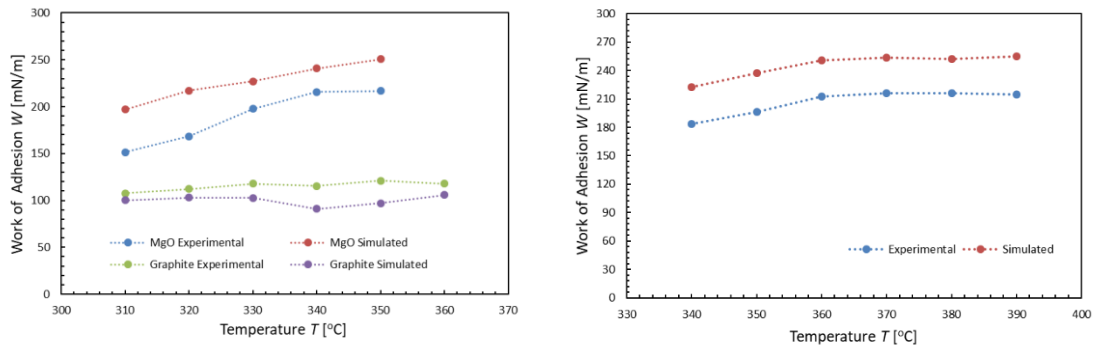


Figure 5.24 Work of adhesion, comparison with experimental data

5.3.8 Influence of substrate thickness on the contact angle

For computational efficiency reasons the thickness of the substrate, is represented by one layer of atoms. Simulations are conducted for 1 to 7 layers of substrate to investigate the effect of the substrate thickness on the CA (Figure 5.25). In the case of the graphite, since the cuboid posts do extend the height of the surface no significant fluctuation is expected. However, also for the case of the MgO no effect on the calculated CA is observed in terms of the substrate thickness.

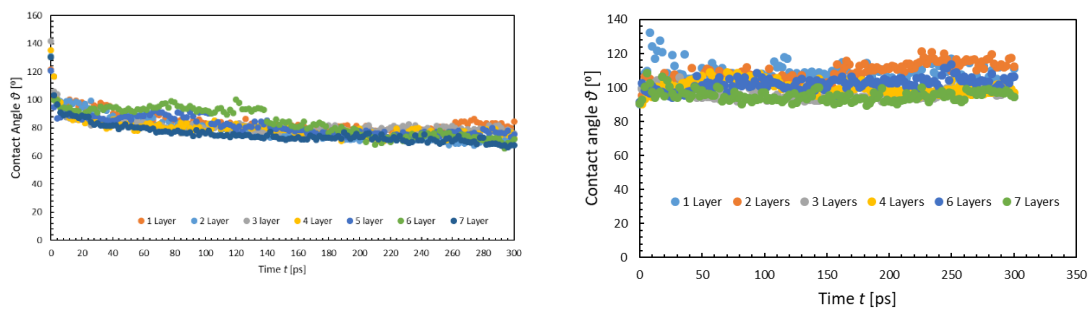


Figure 5.25 Evolution of contact angle with different substrate thickness.

5.3.9 Inside the Carbon Nanotube

The roughness of a surface can play a significant role on the wetting behavior of a liquid on its surface. Furthermore, carbon materials, as discussed in the introduction,

are used both as matrixes for the storage of the molten salt or in the form of nanosuspensions. To this end the wetting behavior of the molten salt is simulated inside a CNT (nanosuspensions) as well as on the top of an unwrapped CNT (smooth graphene surface), through MD simulations to identify that indeed the non-wetting behavior of the graphite is not solely related to the roughness and secondarily to show how MD simulations can provide insight in the flow of the salt in nanopores.

A range of CNT diameters are simulated from 10 to 80 Å. An increase of the molten salt density inside the CNT is observed analogous to the diameter length. Up to 50 Å the density is significantly lower than its bulk molten value. Similar observations are present in the literature for the case of water, but the transition to bulk density occurs in smaller diameters²⁰³. For CNT systems, where bulk density is achieved the CA of the molten salt with the inner surface of the CNT is sampled. A hydrophobic behavior is observed. In all cases the CA of the salt is above 103 ° (Table 5.6). Unfortunately no measurements involving sodium or potassium nitrate have been conducted in CNTs, but experiments involving other molten nitrates (e.g. AlNO_3), denote a hydrophobic behavior^{204,205}.

Additionally, the density of the salt near the carbon/liquid interface is significantly altered (Figure 5.26). In the center of the CNT the density retains its bulk value. However, in the vicinity of the inner surface of the CNT the density appears to increase up to 30%. This is due to the non-polar relationship between the carbon and the salt, which leads to the formation of a compressed layer of atoms.

Studies on a smooth graphene surface also result in a non-wetting behavior suggesting that the wetting behavior of graphite is indeed hydrophobic regardless of roughness. This poor wettability as discussed above can lead to the swelling effects observed in composites.

Table 5.6 Calculated Contact Angle values for NaNO₃ and KNO₃ in CNT of different diameters. The last column represents graphene.

Carbon Nanotube	Diameter	50 Å	60 Å	70 Å	80 Å	--
NaNO ₃	Contact Angle	125°	123°	124°	121°	108°
KNO ₃	Contact Angle	112°	111°	107°	108°	103°

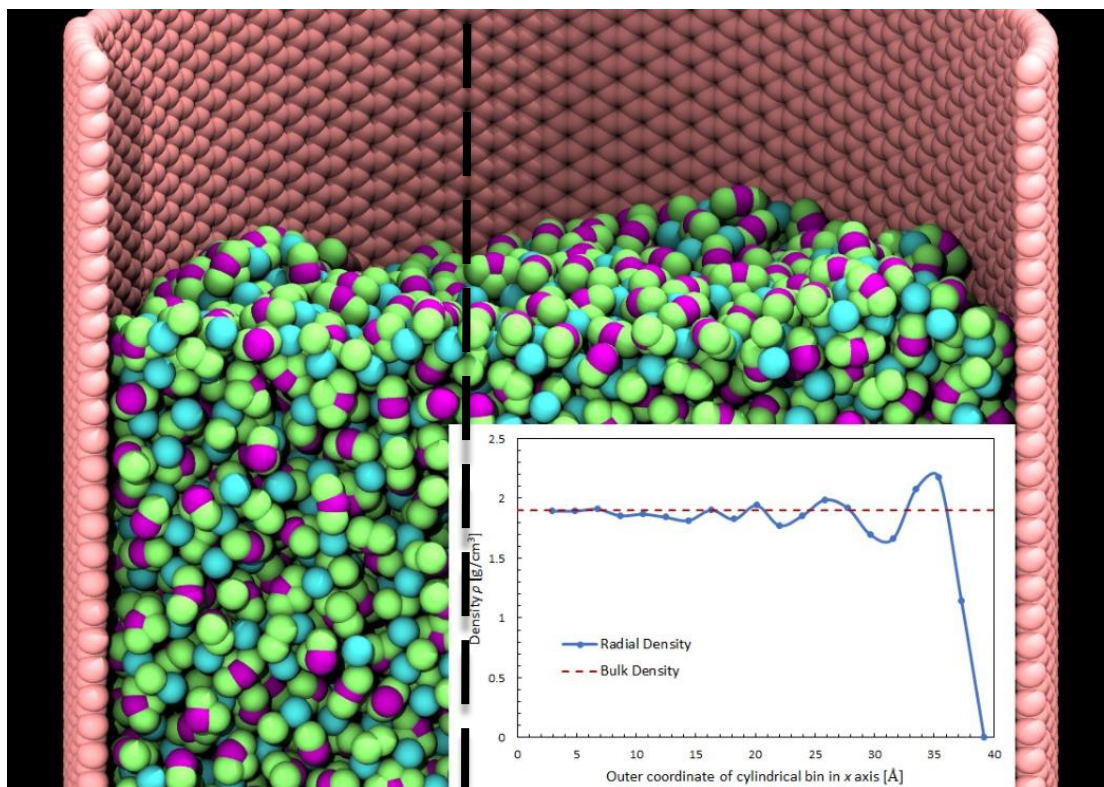


Figure 5.26 Density of molten NaNO_3 inside the CNT, for different diameters.

5.4 Simulation of the wetting of molten $\text{NaNO}_3\text{-KNO}_3$ mixtures with and without $\alpha\text{-SiO}_2$ on MgO

Developing and validating two novel set of intermolecular parameters is as mentioned a prerequisite for modelling correctly the cross-term interatomic interactions between the molten salt, MgO and silica NPs. In this section the novel set of Lennard-Jones parameters are used to simulate the wetting of molten nitrate salt amorphous silica mixtures on MgO.

The salt is first equilibrated on its own using the process discussed in section 5.1.3. To account for line tension effects the number of salt molecules translates to a droplet

size of 10nm. Subsequently an intender is used to create holes for the silica NPs to be placed inside the salt. The concentration of silica is set at 1.5 wt. %. This is expressed as 10 particles with a diameter of 1nm. The particles are treated as rigid bodies and simulated using the rigid package available in LAMMPS. After equilibrating the salt-nanoparticle mixture, for 2ns in the NPT ensemble followed by 0.5ns in the NVT ensemble, it is placed on the ceramic surface. The wetting simulation is conducted using the methodology described in detail in section 4.3. Two systems are modelled, one with and one without silica NPs. Independent simulations are run for temperatures ranging from 523 to 673K at intervals of 25K.

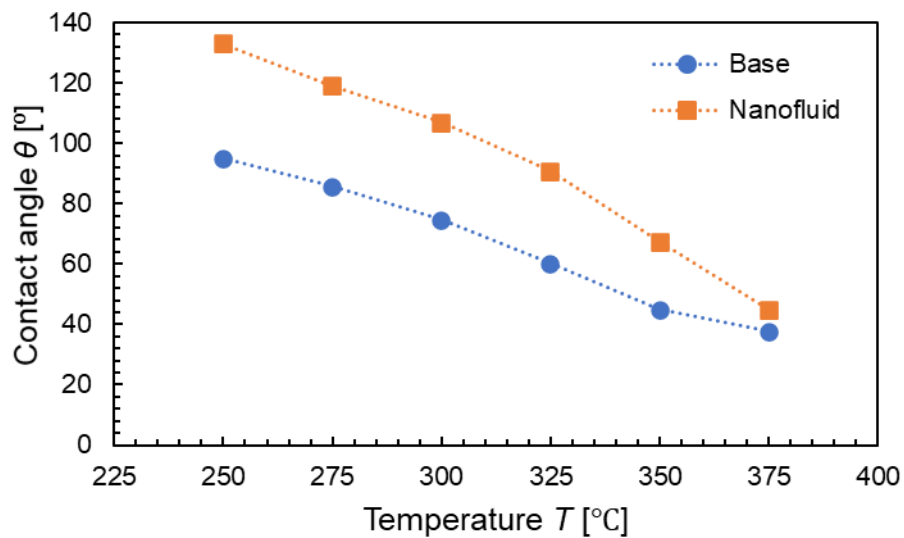


Figure 5.27 Contact Angle versus Temperature of Solar Salt and Solar Salt doped with silica Nanoparticles

The addition of NPs significantly affects the wetting process (Figure 5.27). The SS displays a linear decrease in its CA with an increase in the temperature. This does not occur in the presence of NPs. In both cases the initial CA is non-wetting. However, the base salt transitions to a wetting state at 573K. On the other hand, the MSNF

transitions from non-wetting at 623K. Furthermore, the initial CA of the MSNF is considerably higher than that of the base salt. What is evident is that the silica NPs due to solid-liquid layer formation lead to the creation of a matrix that increases the cohesive forces on the salt droplet. In order to break this structure more vibration (kinetic energy) is required and thus the transition from non-wetting to wetting occurs at high temperatures, where more kinetic energy is readily available. In the cases of the independent component salts, this transition is not observed, probably due to the fact that their melting points are significantly higher (Figure 5.28). Thus, the microstructure formed by the well-dispersed NPs is more rapidly dissolved due to the higher kinetic energy. Suggestive of this phenomenon is a subsequent study conducted on MSNFs composed of carbonate salts with alumina particles. The carbonate ternary salt, doped with Al_2O_3 NPs, is melted at 410 °C and is observed to instantly wet the surface despite the presence of NPs.

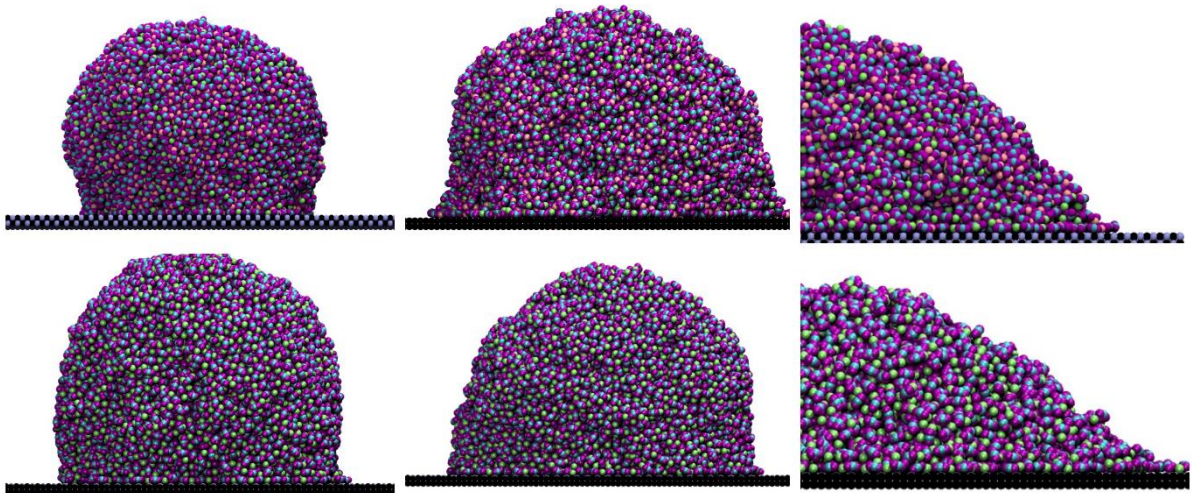


Figure 5.28 Contact angle evolution with temperature of Solar Salt with (top) and without (bottom) silica NPs. Left column 520K, middle 575K and right 625K.

One notable difference between the simulations (Figure 5.27) and the experimental results (Section 4.1.1) is the absence of a plateau in the first case. In the experiments the CA is observed to retain stable values up until 300 °C (Figure 4.1). However, in the case of the MD even at 275 °C a steady decay is observed. Many factors can explain this behavior. They are all, to an extent, linked to macroscale effects that are impossible to capture in MD. The first is the absence of a phase transition and a heat source outside the salt. In the case of the MD, the salt initiates as already molten and slowly equilibrates on the surface. The heat is given through a thermostat directly to the liquid and not provided through a heat source from the surrounding atmosphere. Furthermore, simulations are conducted independently at each temperature point. In the case of the experiments the phenomena is continuous; the salt slowly melts firstly from the top side, due to the heat coming uniformly, from the hot gas in the CA chamber, and then the regions under it. This causes the outer layer of the pellet to melt and slowly wet the salt under it. Convection phenomena start to interplay and affect the movement and clustering of NPs. This phenomenon cannot be captured in MD, as the scale is too low for liquid convection and also due to the fact that periodicity is present affect the way heat fluxes are modeled. These NPs can then as discussed be slowly clustering in particular regions of the droplet, affecting its force balance at the triplet contact line and thus preventing the wetting, particularly at lower temperatures, where viscosity and surface tension are higher. More simulations should be conducted at the same temperature points with NPs at different initial positions to better understand the effect that can have in the CA evolution.

Chapter 6 CONCLUSIONS AND FUTURE PLANS

6.1 Conclusions

The main outcome of this research work is the improvement on the current understanding of the effect of NP addition on the wetting behavior of molten salts. Mixtures of molten nitrate salts, as well as their independent components are doped with various concentrations of silica NPs. An effect on the wetting behavior is observed in the case of molten nitrate mixtures, but not for independent salts. In the case of the Solar Salt (60% NaNO_3 – 40% KNO_3) addition of a small fraction of NPs has a significant impact on the temperature point at which the salt transitions from wetting to non-wetting. In the absence of NPs this occurs roughly at 260 °C. Adding NPs shifts this to 300 °C. Higher, concentrations of NPs elevate this transition at even higher temperatures. Unlike the case of mixtures solely NaNO_3 and KNO_3 do not display similar behavior, when doped with NPs.

Further measurements of the viscosity of these salts is also conducted. Similar behavior to the CA is observed. In the case of the Solar Salt addition of NPs leads to a higher value at the melting point (220 °C), which normalizes to base value at higher temperatures. NaNO₃ and KNO₃ independently, do not display similar behavior.

DSC measurements show that the addition of NPs widens the transition of the Solar Salt shifting the onset and endset to lower and higher temperature points respectively. In the case of the independent component salts, this is not observed. At higher concentrations the endset temperature arrives up to 251 °C coinciding with the temperature range at which the drop in the value of the viscosity is observed. Compression of pellets of different temperatures, shows that at lower compression rates the effect is more prevalent, while at very high ones is almost diminished. This is found to justify why the drop in the CA is observed at significantly higher temperatures than the viscosity. To rule out reactions as the possible reason behind these observations, XRD measurements are conducted on the salt-nanoparticle mixtures before and after melting overnight, showing no change in the observed peaks neither on the salt nanoparticle mixture or the ceramic surface.

Since, the change of the behavior is identified in the case of mixtures, mixtures with different ratios of NaNO₃ and KNO₃ are tested at intervals of 20%. The mixtures with high differences in component ratios showed the highest initial CA. However, differences in the initial CA at the melting points are eliminated after a couple of tens of degrees Celsius. Nevertheless, this initial behavior is suggestive to the higher energy required in certain cases to conclude the phase transition process.

Finally, the wetting behavior of NaNO_3 , KNO_3 and LiNO_3 is compared. KNO_3 displays the least wetting behavior, while LiNO_3 the most. Looking at the ionic properties and electronic configuration of the 3 different ions, a larger ionic radius and a more complex electronic configuration lead to a less wetting behavior and vice versa.

To develop a better understanding of the effect of NPs on the wetting behavior, subsequent measurements are conducted on the SS with various types of graphite particles this time on MgO (1 1 0). Different particle sizes display a different behavior with smaller sized particles displaying a big decrease at 280 °C, medium sized particles a gradual decrease and micro sized particles almost no difference compared to the base case. Finally, medium sized particles shift the full wetting point to 450 °C from 380 °C. Comparing the results with viscosity values from the literature shows a correlation between the two properties. The nanosized particles have a viscosity 900% higher than the base up until 300 °C, after which the value is reduced to the base case. Similar patterns are observed for the other two sizes, with the flakes showing a gradual decrease never coinciding with the base and the micron sized particles initially higher values that coincide with the base at 350 °C. Concussively, different particle sizes displayed different behavior that to an extent coincides with their rheological trends.

Further studies were conducted on the effect of surface type on the evolution of the CA of the SS. Ceramic type polar surfaces revealed a wetting behavior with slight variations, despite almost identical roughness levels, attributed to different surface energy. A rough stainless-steel surface revealed a non-wetting behavior up until 350 °C.

Similarly, a rough graphite surface also revealed a non-wetting behavior, but this time constant up until 500 °C.

Surface graphitization through spraying is a state-of-art method for corrosion prevention. To investigate the nature of this inhibition the wettability of a carbonate tenary salt on two types of stainless steel as well as an alumina surface is investigated. The initial behavior of the molten salt on both graphitized steel surfaces is non-wetting. On the other hand, the non-graphitized surfaces showed an instantly wetting behavior. However, with time also the graphitized surface revealed to be wetted by the salt. On the other hand, the alumina surface when graphitized showed no wetting behavior up until 24h. Furthermore, in the case of the graphitized steel surfaces the transitions from non-wetting to wetting are found to coincide with the reaction time required to form the protective carbide layer, that is the main mechanism behind the inhibition to corrosion. This suggests that the CA can not only be used as a measurement of the wetting behavior but can also have an observational role in identifying possible reactions that occur at an interface.

To improve the understanding of the effect of NPs on the wetting behavior of the SS, MD simulations are also conducted. Since wetting behavior is mostly governed by the interactions between the materials at their interface, the cross-term interatomic parameters are crucial to the correct simulation of the system. The only type of force-field that provides validated equations for the calculation of the cross-term parameters between different species is the L-J pair potential. Both the amorphous silica and the molten salts are typically simulated using Buckingham type of potentials, for which no

cross-term interaction equations are available. To tackle this, new force field parameters are created for both the salt and the NP elements by fitting the energy curves of the Buckingham type potential in the case of the SS and of the Morse type in the case of α -SiO₂. The new force fields are then checked for local structures and transport properties and are found to be in good agreement in all cases. In the case of the silica more emphasis is placed on the local structure of the solid material since no intramolecular constraints are used. Therefore, also the ADF, coordination number and mean bond length are checked and found to be in perfect agreement with both the Morse type potential and experimental measurements.

In order to validate the obtained cross-term interactions a simulation of molten salt on a block of α -SiO₂ is also conducted. The bulk density of the salt is found to be significantly higher close to the interface, reaching values close to that of a solid. At longer distances from the surface the SS reverts to each experimental value of 1.9 g/cm³. The MSD of the salt atoms is also examined and found to be significantly lower suggesting a more solid-like structure with less atom mobility. Finally, the RDF of the cross-term elements is also studied. The ions in the vicinity of the surface are found to be aligned and at separated in two distinct layers.

To develop a better understanding of the physics that govern the wetting phenomena in the nano-scale the new parameters are first used on the simulation of the molten NaNO₃ and KNO₃ on MgO on graphite as well as inside a CNT. Various system sizes are examined. It is observed that a droplet of a radius of 10nm is necessary to obtain a result that is close to that obtain through experimental measurements. This is due to

line tension effects. The line tension is also calculated through comparison of the obtained CA at various system sizes with that in the macroscopic scale. It is found to be in the range of $-3.6 \cdot 10^{-11}$ for the case of the MgO and $-2.0 \cdot 10^{-11}$ in the case of the carbon surface. Furthermore, both simulated molten salts are found to be non-wetting on the carbon surface, while a hydrophilic behavior is obtained for the ceramic surface. Subsequently, also the work of adhesion is found to be much lower in the case of the carbon surface compared with the ceramic, obtained from the Young-Dupré equation. Additionally, no significant variation in the obtained CA value is observed, when varying the thickness of surface in either case. Finally, the CA of the molten salts inside the CNT are studied and found to also display a non-wetting behavior.

The last section of this thesis involves the simulation of the wetting behavior of the MSNF. SS with silica NPs at 1.5 wt.% concentration is simulated. The NPs are modelled as 10 rigid bodies of 1 nm diameter. Considerable difference is observed in the wetting of the salt doped with NPs. Both with and without NPs the initial CA is non-wetting, but significantly higher in the case of NPs. Furthermore, the transition from non-wetting to wetting occurs at higher temperatures in the presence of NPs. Overall, CA values of the 10 nm radius droplets tested are in good agreement in all cases. The model shows that the silica NPs formulate a certain matrix that increases the cohesion of the salt thus preventing it from wetting the surface. At higher temperatures where atom vibrations are stronger the structure is slowly loosened and the MSNF wets the ceramic surface. It is thus concluded that perhaps the behavior caused by the addition of well-dispersed nano sized particles can be the formation of this matrix which traps the salt in a solid-like state.

6.2 Future Plans

The effect of NP doping on the wetting behavior of the SS was identified. The CA was found to vary in the case of the Solar Salt, but similar behaviors were not identified for independent components. However, all the salts in this study with or without NPs wetted the ceramic surfaces at some temperature. Perhaps studies on non-wetting surfaces, such as that of graphitized alumina or other known hydrophobic surfaces like carbon foil, could provide a better comparison frame between normal and NP doped salt.

Furthermore, it would be interesting to investigate the wetting behavior of the salts with time. As discussed in the literature review and observed also in the case of the graphitization, the wetting behavior of the salts changes with time. Keeping the salt at liquid state for long hours and afterwards performing SEM measurements could provide insight into the change of properties with time, such as the specific heat capacity, and give the CA a role of a indicator of the stability of the NF.

On the other hand, in the case of the graphite particles only the behavior of the SS doped with graphite particles was investigated. Cross-checking the wetting and rheological behavior of the independent components when doped with this type of particles, would be an interesting comparison frame.

In terms of simulations only the MSNF with silica NPs is investigated. NaNO_3 and KNO_3 independently should also be examined, when doped with NPs to examine if indeed the suggestions regarding the required kinetic energy to overcome the matrix created

by the well-dispersed silica is valid. Furthermore, substituting the silica NPs with carbon ones would be interesting in order to see how a hydrophobic particle, as discovered by the wetting simulations, behaves and perhaps draw conclusions, as to why when adding carbon particles of similar size to silica, does the transition from wetting to non-wetting occur at lower temperatures.

REFERENCES

- (1) Schiffer, H.-W.; Kober, T.; Panos, E. World Energy Council's Global Energy Scenarios to 2060. *Zeitschrift für Energiewirtschaft* **2018**, *42* (2), 91–102.
- (2) Zou, C.; Zhao, Q.; Zhang, G.; Xiong, B. Energy Revolution: From a Fossil Energy Era to a New Energy Era. *Nat. Gas Ind. B* **2016**, *3* (1), 1–11.
- (3) Ahmed, S. F.; Khalid, M.; Rashmi, W.; Chan, A.; Shahbaz, K. Recent Progress in Solar Thermal Energy Storage Using Nanomaterials. *Renew. Sustain. Energy Rev.* **2017**, *67*, 450–460.
- (4) Moore, J.; Shabani, B. A Critical Study of Stationary Energy Storage Policies in Australia in an International Context: The Role of Hydrogen and Battery Technologies. *Energies* **2016**, *9* (9), 674.
- (5) Tian, Y.; Zhao, C. Y. A Review of Solar Collectors and Thermal Energy Storage in Solar Thermal Applications. *Appl. Energy* **2013**, *104*, 538–553.
- (6) Liu, L.; Su, D.; Tang, Y.; Fang, G. Thermal Conductivity Enhancement of Phase

- Change Materials for Thermal Energy Storage: A Review. *Renewable and Sustainable Energy Reviews*. 2016.
- (7) Seitz, M.; Johnson, M.; Hübner, S. Economic Impact of Latent Heat Thermal Energy Storage Systems within Direct Steam Generating Solar Thermal Power Plants with Parabolic Troughs. *Energy Convers. Manag.* **2017**, *143*, 286–294.
 - (8) Liu, M.; Saman, W.; Bruno, F. Review on Storage Materials and Thermal Performance Enhancement Techniques for High Temperature Phase Change Thermal Storage Systems. *Renew. Sustain. Energy Rev.* **2012**, *16* (4), 2118–2132.
 - (9) Nithyanandam, K.; Pitchumani, R. Computational Studies on a Latent Thermal Energy Storage System with Integral Heat Pipes for Concentrating Solar Power. *Appl. Energy* **2013**, *103*, 400–415.
 - (10) Mahdi, J. M.; Nsofor, E. C. Solidification Enhancement in a Triplex-Tube Latent Heat Energy Storage System Using Nanoparticles-Metal Foam Combination. *Energy* **2017**, *126*, 501–512.
 - (11) Chieruzzi, M.; Cerritelli, G. F.; Miliozzi, A.; Kenny, J. M. Effect of Nanoparticles on Heat Capacity of Nanofluids Based on Molten Salts as PCM for Thermal Energy Storage. *Nanoscale Res. Lett.* **2013**, *8* (1), 448.
 - (12) Jacob, R.; Bruno, F. Review on Shell Materials Used in the Encapsulation of Phase Change Materials for High Temperature Thermal Energy Storage. *Renew. Sustain. Energy Rev.* **2015**, *48*, 79–87.
 - (13) Muñoz-Sánchez, B.; Nieto-Maestre, J.; Iparraguirre-Torres, I.; García-Romero, A.; Sala-Lizarraga, J. M. Molten Salt-Based Nanofluids as Efficient Heat Transfer and Storage Materials at High Temperatures. An Overview of the Literature. *Renew. Sustain. Energy Rev.* **2018**, *82*, 3924–3945.
 - (14) Kaggwa, A.; Carson, J. K.; Atkins, M.; Walmsley, M. The Effect of Surfactants on Viscosity and Stability of Activated Carbon, Alumina and Copper Oxide Nanofluids. *Mater. Today Proc.* **2019**, *18*, 510–519.
 - (15) Mondragón, R.; Juliá, J. E.; Cabedo, L.; Navarrete, N. On the Relationship between the Specific Heat Enhancement of Salt-Based Nanofluids and the Ionic Exchange Capacity of Nanoparticles. *Sci. Rep.* **2018**, *8* (1), 7532.
 - (16) Lasfargues, M.; Cao, H.; Geng, Q.; Ding, Y. Rheological Analysis of Binary

- Eutectic Mixture of Sodium and Potassium Nitrate and the Effect of Low Concentration CuO Nanoparticle Addition to Its Viscosity. *Materials (Basel)*. **2015**, 8 (8), 5194–5204.
- (17) Gomez-Vidal, J. C.; Tirawat, R. Corrosion of Alloys in a Chloride Molten Salt (NaCl-LiCl) for Solar Thermal Technologies. *Sol. Energy Mater. Sol. Cells* **2016**, 157, 234–244.
- (18) Grosu, Y.; Nithiyantham, U.; Zaki, A.; Faik, A. A Simple Method for the Inhibition of the Corrosion of Carbon Steel by Molten Nitrate Salt for Thermal Storage in Concentrating Solar Power Applications. *npj Mater. Degrad.* **2018**, 2 (1), 34.
- (19) Wu, J.; Li, J.; Xu, X.; Yang, L.; Wu, J.; Zhao, F.; Li, C. Molten Salts/Ceramic-Foam Matrix Composites by Melt Infiltration Method as Energy Storage Material. *J. Wuhan Univ. Technol. Sci. Ed.* **2009**, 24 (4), 651–653.
- (20) Jiang, Z.; Palacios, A.; Lei, X.; Navarro, M. E.; Qiao, G.; Mura, E.; Xu, G.; Ding, Y. Novel Key Parameter for Eutectic Nitrates Based Nanofluids Selection for Concentrating Solar Power (CSP) System. *Appl. Energy* **2019**, 235, 529–542.
- (21) Andreu-Cabedo, P.; Mondragon, R.; Hernandez, L.; Martinez-Cuenca, R.; Cabedo, L.; Julia, J. Increment of Specific Heat Capacity of Solar Salt with SiO₂ Nanoparticles. *Nanoscale Res. Lett.* **2014**, 9 (1), 582.
- (22) Muñoz-Sánchez, B.; Nieto-Maestre, J.; Iparraguirre-Torres, I.; Julià, J. E.; García-Romero, A. Silica and Alumina Nano-Enhanced Molten Salts for Thermal Energy Storage: A Comparison. In *AIP Conference Proceedings*; 2017; p 080018.
- (23) Kim, H.; Jo, B. Anomalous Increase in Specific Heat of Binary Molten Salt-Based Graphite Nanofluids for Thermal Energy Storage. *Appl. Sci.* **2018**, 8 (8), 1305.
- (24) Riazi, H.; Mesgari, S.; Ahmed, N. A.; Taylor, R. A. The Effect of Nanoparticle Morphology on the Specific Heat of Nanosalts. *Int. J. Heat Mass Transf.* **2016**, 94, 254–261.
- (25) Shin, D.; Tiznobaik, H.; Banerjee, D. Specific Heat Mechanism of Molten Salt Nanofluids. *Appl. Phys. Lett.* **2014**, 104 (12), 121914.
- (26) Wang, W.; Wu, Z.; Li, B.; Sundén, B. A Review on Molten-Salt-Based and Ionic-Liquid-Based Nanofluids for Medium-to-High Temperature Heat Transfer. *J.*

- Therm. Anal. Calorim.* **2019**, *136* (3), 1037–1051.
- (27) Muñoz-Sánchez, B.; Nieto-Maestre, J.; Veca, E.; Liberatore, R.; Sau, S.; Navarro, H.; Ding, Y.; Navarrete, N.; Juliá, J. E.; Fernández, Á. G.; García-Romero, A. Rheology of Solar-Salt Based Nanofluids for Concentrated Solar Power. Influence of the Salt Purity, Nanoparticle Concentration, Temperature and Rheometer Geometry. *Sol. Energy Mater. Sol. Cells* **2018**, *176*, 357–373.
- (28) Palacios, A.; Navarro, M. E.; Ding, Y. Thermal and Rheological Behavior of Solar Salt Containing Highly Thermally Conductive Particles. In *AIP Conference Proceedings*; 2018; p 080003.
- (29) Lasfargues, M.; Cao, H.; Geng, Q.; Ding, Y. Rheological Analysis of Binary Eutectic Mixture of Sodium and Potassium Nitrate and the Effect of Low Concentration CuO Nanoparticle Addition to Its Viscosity. *Materials (Basel)*. **2015**, *8* (8), 5194–5204.
- (30) Riazi, H.; Murphy, T.; Webber, G. B.; Atkin, R.; Tehrani, S. S. M.; Taylor, R. A. Specific Heat Control of Nanofluids: A Critical Review. *Int. J. Therm. Sci.* **2016**, *107*, 25–38.
- (31) Peiró, G.; Prieto, C.; Gasia, J.; Jové, A.; Miró, L.; Cabeza, L. F. Two-Tank Molten Salts Thermal Energy Storage System for Solar Power Plants at Pilot Plant Scale: Lessons Learnt and Recommendations for Its Design, Start-up and Operation. *Renew. Energy* **2018**, *121*, 236–248.
- (32) Gottschalk, A.; Ramamoorthi, U. Parametric Simulation and Economic Estimation of Thermal Energy Storage in Solar Power Tower. *Mater. Today Proc.* **2018**, *5* (1), 1571–1577.
- (33) Walczak, M.; Pineda, F.; Fernández, Á. G.; Mata-Torres, C.; Escobar, R. A. Materials Corrosion for Thermal Energy Storage Systems in Concentrated Solar Power Plants. *Renew. Sustain. Energy Rev.* **2018**, *86*, 22–44.
- (34) Federsel, K.; Wortmann, J.; Ladenberger, M. High-Temperature and Corrosion Behavior of Nitrate Nitrite Molten Salt Mixtures Regarding Their Application in Concentrating Solar Power Plants. *Energy Procedia* **2015**, *69*, 618–625.
- (35) Wang, W.; Guan, B.; Li, X.; Lu, J.; Ding, J. Corrosion Behavior and Mechanism of Austenitic Stainless Steels in a New Quaternary Molten Salt for Concentrating Solar Power. *Sol. Energy Mater. Sol. Cells* **2019**, *194*, 36–46.

- (36) Li, X. L.; Wei, X.; Lu, J.; Ding, J.; Wang, W. Corrosion Resistance of 310S and 316L Austenitic Stainless Steel in a Quaternary Molten Salt for Concentrating Solar Power. *Energy Procedia* **2017**, *142*, 3590–3596.
- (37) Goods, S. H.; Bradshaw, R. W. Corrosion of Stainless Steels and Carbon Steel by Molten Mixtures of Commercial Nitrate Salts. *J. Mater. Eng. Perform.* **2004**, *13* (1), 78–87.
- (38) Bauer, T.; Pflieger, N.; Breidenbach, N.; Eck, M.; Laing, D.; Kaesche, S. Material Aspects of Solar Salt for Sensible Heat Storage. *Appl. Energy* **2013**, *111*, 1114–1119.
- (39) Ruiz-Cabañas, F. J.; Prieto, C.; Osuna, R.; Madina, V.; Fernández, A. I.; Cabeza, L. F. Corrosion Testing Device for In-Situ Corrosion Characterization in Operational Molten Salts Storage Tanks: A516 Gr70 Carbon Steel Performance under Molten Salts Exposure. *Sol. Energy Mater. Sol. Cells* **2016**, *157*, 383–392.
- (40) Dorcheh, A. S.; Durham, R. N.; Galetz, M. C. High Temperature Corrosion in Molten Solar Salt: The Role of Chloride Impurities. *Mater. Corros.* **2017**, *68* (9), 943–951.
- (41) Ding, W.; Bonk, A.; Bauer, T. Corrosion Behavior of Metallic Alloys in Molten Chloride Salts for Thermal Energy Storage in Concentrated Solar Power Plants: A Review. *Front. Chem. Sci. Eng.* **2018**, *12* (3), 564–576.
- (42) Fernández, A. G.; Pineda, F.; Walczak, M.; Cabeza, L. F. Corrosion Evaluation of Alumina-Forming Alloys in Carbonate Molten Salt for CSP Plants. *Renew. Energy* **2019**, *140*, 227–233.
- (43) de Miguel, M. T.; Encinas-Sánchez, V.; Lasanta, M. I.; García-Martín, G.; Pérez, F. J. Corrosion Resistance of HR3C to a Carbonate Molten Salt for Energy Storage Applications in CSP Plants. *Sol. Energy Mater. Sol. Cells* **2016**, *157*, 966–972.
- (44) Takeuchi, K.; Nishijima, A.; Ui, K.; Koura, N.; Loong, C.-K. Corrosion Behavior of Fe-Cr Alloys in $\text{Li}_2\text{CO}_3\text{-K}_2\text{CO}_3$ Molten Carbonate. *J. Electrochem. Soc.* **2005**, *152* (9), B364.
- (45) Frangini, S.; Loreti, S. The Role of Temperature on the Corrosion and Passivation of Type 310S Stainless Steel in Eutectic (Li+K) Carbonate Melt. *J. Power Sources* **2006**, *160* (2), 800–804.

- (46) Liu, M.; Steven Tay, N. H.; Bell, S.; Belusko, M.; Jacob, R.; Will, G.; Saman, W.; Bruno, F. Review on Concentrating Solar Power Plants and New Developments in High Temperature Thermal Energy Storage Technologies. *Renew. Sustain. Energy Rev.* **2016**, *53*, 1411–1432.
- (47) Agüero, A.; Audigié, P.; Rodríguez, S.; Encinas-Sánchez, V.; de Miguel, M. T.; Pérez, F. J. Protective Coatings for High Temperature Molten Salt Heat Storage Systems in Solar Concentration Power Plants; 2018; p 090001.
- (48) Encinas-Sánchez, V.; Batuecas, E.; Macías-García, A.; Mayo, C.; Díaz, R.; Pérez, F. J. Corrosion Resistance of Protective Coatings against Molten Nitrate Salts for Thermal Energy Storage and Their Environmental Impact in CSP Technology. *Sol. Energy* **2018**, *176*, 688–697.
- (49) Porcayo-Calderon, J.; Sotelo-Mazon, O.; Salinas-Bravo, V. M.; Arrieta-Gonzalez, C. D.; Ramos-Hernandez, J. J.; Cuevas-Arteaga, C. Electrochemical Performance of Ni20Cr Coatings Applied by Combustion Powder Spray in ZNCL2-KCL Molten Salts. *Int. J. Electrochem. Sci.* **2012**.
- (50) Gomez-Vidal, J. C. Corrosion Resistance of MCrAlX Coatings in a Molten Chloride for Thermal Storage in Concentrating Solar Power Applications. *npj Mater. Degrad.* **2017**, *1* (1), 7.
- (51) Ding, W.; Shi, H.; Jianu, A.; Xiu, Y.; Bonk, A.; Weisenburger, A.; Bauer, T. Molten Chloride Salts for next Generation Concentrated Solar Power Plants: Mitigation Strategies against Corrosion of Structural Materials. *Sol. Energy Mater. Sol. Cells* **2019**, *193*, 298–313.
- (52) Frangini, S.; Loreti, S. The Role of Alkaline-Earth Additives on the Molten Carbonate Corrosion of 316L Stainless Steel. *Corros. Sci.* **2007**, *49* (10), 3969–3987.
- (53) Piquot, J.; Nithiyantham, U.; Grosu, Y.; Faik, A. Spray-Graphitization as a Protection Method against Corrosion by Molten Nitrate Salts and Molten Salts Based Nanofluids for Thermal Energy Storage Applications. *Sol. Energy Mater. Sol. Cells* **2019**, *200*, 110024.
- (54) Gonzalez, M.; Nithiyantham, U.; Carbó-Argibay, E.; Bondarchuk, O.; Grosu, Y.; Faik, A. Graphitization as Efficient Inhibitor of the Carbon Steel Corrosion by Molten Binary Nitrate Salt for Thermal Energy Storage at Concentrated Solar

- Power. *Sol. Energy Mater. Sol. Cells* **2019**, *203*, 110172.
- (55) Wang, Y. B.; Li, H. F.; Zheng, Y. F.; Wei, S. C.; Li, M. Correlation between Corrosion Performance and Surface Wettability in ZrTiCuNiBe Bulk Metallic Glasses. *Appl. Phys. Lett.* **2010**, *96* (25), 251909.
- (56) Ge, Z.; Ye, F.; Cao, H.; Leng, G.; Qin, Y.; Ding, Y. Carbonate-Salt-Based Composite Materials for Medium- and High-Temperature Thermal Energy Storage. *Particuology* **2014**, *15*, 77–81.
- (57) Acem, Z.; Lopez, J.; Palomo Del Barrio, E. KNO₃/NaNO₃ – Graphite Materials for Thermal Energy Storage at High Temperature: Part I. – Elaboration Methods and Thermal Properties. *Appl. Therm. Eng.* **2010**, *30* (13), 1580–1585.
- (58) CELZARD, A.; MARECHE, J.; FURDIN, G. Modelling of Exfoliated Graphite. *Prog. Mater. Sci.* **2005**, *50* (1), 93–179.
- (59) Zhang, Z.; Shao, G.; Fang, X. Study on Paraffin/Expanded Graphite Composite Phase Change Thermal Energy Storage Material. *Taiyangneng Xuebao/Acta Energiae Solaris Sin.* **2005**.
- (60) RHEE, S. K. Critical Surface Energies of Al₂O₃ and Graphite. *J. Am. Ceram. Soc.* **1972**, *55* (6), 300–303.
- (61) Ge, Z.; Ye, F.; Ding, Y. Composite Materials for Thermal Energy Storage: Enhancing Performance through Microstructures. *ChemSusChem* **2014**, *7* (5), 1318–1325.
- (62) Li, C.; Li, Q.; Cong, L.; Li, Y.; Liu, X.; Xuan, Y.; Ding, Y. Carbonate Salt Based Composite Phase Change Materials for Medium and High Temperature Thermal Energy Storage: A Microstructural Study. *Sol. Energy Mater. Sol. Cells* **2019**, *196*, 25–35.
- (63) Morel, C. F. Surface Tensions of Molten Salts and Contact Angle Measurements of Molten Salts on Solids. *Euratom* **1970**.
- (64) Baumli, P.; Kaptay, G. Wettability of Carbon Surfaces by Molten Alkali Chloride Mixtures. *Mater. Sci. Forum* **2008**, *589*, 355–359.
- (65) Baumli, P.; Kaptay, G. Wettability of Carbon Surfaces by Pure Molten Alkali Chlorides and Their Penetration into a Porous Graphite Substrate. *Mater. Sci. Eng. A* **2008**, *495* (1–2), 192–196.
- (66) Stepanov, V. P. Wetting of a Charged Surface of Glassy Carbon by Molten Alkali-

- Metal Chlorides. *Russ. J. Phys. Chem. A* **2018**, *92* (3), 570–574.
- (67) He, Z.; Gao, L.; Qi, W.; Zhang, B.; Wang, X.; Song, J.; He, X.; Zhang, C.; Tang, H.; Holmes, R.; Xia, H.; Zhou, X. Molten FLiNaK Salt Infiltration into Degassed Nuclear Graphite under Inert Gas Pressure. *Carbon N. Y.* **2015**, *84*, 511–518.
- (68) Lian, P.; Song, J.; Liu, Z.; Zhang, J.; Zhao, Y.; Gao, Y.; Tao, Z.; He, Z.; Gao, L.; Xia, H.; Guo, Q.; Huai, P.; Zhou, X. Preparation of Ultrafine-Grain Graphite by Liquid Dispersion Technique for Inhibiting the Liquid Fluoride Salt Infiltration. *Carbon N. Y.* **2016**, *102*, 208–215.
- (69) Fisher, J. M.; Bennett, P. S. Corrosion and Wetting Behaviour of Metals and Steels with Molten Alkali Carbonates. *J. Mater. Sci.* **1991**, *26* (3), 749–755.
- (70) Li, C.; Li, Q.; Cao, H.; Leng, G.; Li, Y.; Wang, L.; Zheng, L.; Ding, Y. Wettability of Eutectic NaLiCO₃ Salt on Magnesium Oxide Substrates at 778 K. *Appl. Surf. Sci.* **2018**, *442*, 148–155.
- (71) Morrow, N. R. Wettability and Its Effect on Oil Recovery. *J. Pet. Technol.* **1990**, *42* (12), 1476–1484.
- (72) Wu, K.; Chen, Z.; Li, J.; Li, X.; Xu, J.; Dong, X. Wettability Effect on Nanoconfined Water Flow. *Proc. Natl. Acad. Sci.* **2017**, *114* (13), 3358–3363.
- (73) Nguyen, C. T.; Barisik, M.; Kim, B. Wetting of Chemically Heterogeneous Striped Surfaces: Molecular Dynamics Simulations. *AIP Adv.* **2018**, *8* (6), 065003.
- (74) Khalkhali, M.; Kazemi, N.; Zhang, H.; Liu, Q. Wetting at the Nanoscale: A Molecular Dynamics Study. *J. Chem. Phys.* **2017**, *146* (11), 114704.
- (75) Werder, T.; Walther, J. H.; Jaffe, R. L.; Halicioglu, T.; Koumoutsakos, P. On the Water–Carbon Interaction for Use in Molecular Dynamics Simulations of Graphite and Carbon Nanotubes. *J. Phys. Chem. B* **2003**, *107* (6), 1345–1352.
- (76) Scocchi, G.; Sergi, D.; D’Angelo, C.; Ortona, A. Wetting and Contact-Line Effects for Spherical and Cylindrical Droplets on Graphene Layers: A Comparative Molecular-Dynamics Investigation. *Phys. Rev. E* **2011**, *84* (6), 061602.
- (77) Zhang, J.; Wang, P.; Borg, M. K.; Reese, J. M.; Wen, D. A Critical Assessment of the Line Tension Determined by the Modified Young’s Equation. *Phys. Fluids* **2018**, *30* (8), 082003.
- (78) Kanduč, M.; Eixeres, L.; Liese, S.; Netz, R. R. Generalized Line Tension of Water Nanodroplets. *Phys. Rev. E* **2018**, *98* (3), 032804.

- (79) Santiso, E.; Herdes, C.; Müller, E. On the Calculation of Solid-Fluid Contact Angles from Molecular Dynamics. *Entropy* **2013**, *15* (12), 3734–3745.
- (80) Ravipati, S.; Aymard, B.; Kalliadasis, S.; Galindo, A. On the Equilibrium Contact Angle of Sessile Liquid Drops from Molecular Dynamics Simulations. *J. Chem. Phys.* **2018**, *148* (16), 164704.
- (81) Vafaei, S.; Podowski, M. Z. Analysis of the Relationship between Liquid Droplet Size and Contact Angle. *Adv. Colloid Interface Sci.* **2005**, *113* (2–3), 133–146.
- (82) Giljean, S.; Bigerelle, M.; Anselme, K.; Haidara, H. New Insights on Contact Angle/Roughness Dependence on High Surface Energy Materials. *Appl. Surf. Sci.* **2011**, *257* (22), 9631–9638.
- (83) Vafaei, S.; Podowski, M. Z. Theoretical Analysis on the Effect of Liquid Droplet Geometry on Contact Angle. *Nucl. Eng. Des.* **2005**, *235* (10–12), 1293–1301.
- (84) Zhang, C.; Liu, Z.; Deng, P. Contact Angle of Soil Minerals: A Molecular Dynamics Study. *Comput. Geotech.* **2016**, *75*, 48–56.
- (85) Jiang, H.; Patel, A. J. Recent Advances in Estimating Contact Angles Using Molecular Simulations and Enhanced Sampling Methods. *Curr. Opin. Chem. Eng.* **2019**, *23*, 130–137.
- (86) Edwards, F. G.; Enderby, J. E.; Howe, R. A.; Page, D. I. The Structure of Molten Sodium Chloride. *J. Phys. C Solid State Phys.* **1975**, *8* (21), 3483–3490.
- (87) Caccamo, C.; Dixon, M. Molten Alkali-Halide Mixtures: A Molecular-Dynamics Study of Li/KCl Mixtures. *J. Phys. C Solid State Phys.* **1980**, *13* (10), 1887–1900.
- (88) Mitchell, E. W. J.; Poncet, P. F. J.; Stewart, R. J. The Ion Pair Distribution Functions in Molten Rubidium Chloride. *Philos. Mag.* **1976**, *34* (5), 721–732.
- (89) Wu, J.; Ni, H.; Liang, W.; Lu, G.; Yu, J. Molecular Dynamics Simulation on Local Structure and Thermodynamic Properties of Molten Ternary Chlorides Systems for Thermal Energy Storage. *Comput. Mater. Sci.* **2019**, *170*, 109051.
- (90) Ding, J.; Pan, G.; Du, L.; Lu, J.; Wei, X.; Li, J.; Wang, W.; Yan, J. Theoretical Prediction of the Local Structures and Transport Properties of Binary Alkali Chloride Salts for Concentrating Solar Power. *Nano Energy* **2017**, *39*, 380–389.
- (91) Bengtson, A.; Nam, H. O.; Saha, S.; Sakidja, R.; Morgan, D. First-Principles Molecular Dynamics Modeling of the LiCl–KCl Molten Salt System. *Comput. Mater. Sci.* **2014**, *83*, 362–370.

- (92) Wang, J.; Sun, Z.; Lu, G.; Yu, J. Molecular Dynamics Simulations of the Local Structures and Transport Coefficients of Molten Alkali Chlorides. *J. Phys. Chem. B* **2014**, *118* (34), 10196–10206.
- (93) Wang, J.; Wu, J.; Sun, Z.; Lu, G.; Yu, J. Molecular Dynamics Study of the Transport Properties and Local Structures of Molten Binary Systems (Li, Na)Cl, (Li, K)Cl and (Na, K)Cl. *J. Mol. Liq.* **2015**, *209*, 498–507.
- (94) Sun, Z.; Cai, L.; Ni, H.; Lu, G.; Song, X.; Yu, J. Investigation of the Local Structures and Transport Properties of Quaternary Molten Alkali Chloride Systems by MD Simulations for Liquid Metal Batteries. *J. Appl. Electrochem.* **2018**, *48* (10), 1175–1187.
- (95) Ding, J.; Pan, G.; Du, L.; Lu, J.; Wang, W.; Wei, X.; Li, J. Molecular Dynamics Simulations of the Local Structures and Transport Properties of Na₂CO₃ and K₂CO₃. *Appl. Energy* **2018**, *227*, 555–563.
- (96) Ding, J.; Pan, G.; Du, L.; Lu, J.; Wang, W.; Wei, X.; Li, J. Molecular Dynamics Simulations of the Local Structures and Transport Properties of Na₂CO₃ and K₂CO₃. *Appl. Energy* **2018**, *227*, 555–563.
- (97) Adya, A. K.; Takagi, R.; Kawamura, K.; Mikami, M. Structural Determination of Molten NaNO₃, NaNO₂ and Their Eutectic Mixture by Molecular Dynamics Simulation and X-Ray Diffraction. *Mol. Phys.* **1987**, *62* (1), 227–238.
- (98) Qiao, G.; Lasfargues, M.; Alexiadis, A.; Ding, Y. Simulation and Experimental Study of the Specific Heat Capacity of Molten Salt Based Nanofluids. *Appl. Therm. Eng.* **2017**, *111*, 1517–1522.
- (99) Qiao, G.; Alexiadis, A.; Ding, Y. Simulation Study of Anomalous Thermal Properties of Molten Nitrate Salt. *Powder Technol.* **2017**, *314*, 660–664.
- (100) Jayaraman, S.; Thompson, A. P.; von Lilienfeld, O. A.; Maginn, E. J. Molecular Simulation of the Thermal and Transport Properties of Three Alkali Nitrate Salts. *Ind. Eng. Chem. Res.* **2010**, *49* (2), 559–571.
- (101) Jayaraman, S.; Thompson, A. P.; von Lilienfeld, O. A. Molten Salt Eutectics from Atomistic Simulations. *Phys. Rev. E* **2011**, *84* (3), 030201.
- (102) Hu, Y.; He, Y.; Zhang, Z.; Wen, D. Effect of Al₂O₃ Nanoparticle Dispersion on the Specific Heat Capacity of a Eutectic Binary Nitrate Salt for Solar Power Applications. *Energy Convers. Manag.* **2017**, *142*, 366–373.

- (103) Ni, H.; Wu, J.; Sun, Z.; Lu, G.; Yu, J. Molecular Simulation of the Structure and Physical Properties of Alkali Nitrate Salts for Thermal Energy Storage. *Renew. Energy* **2019**, *136*, 955–967.
- (104) Telo Da Gama, M. M.; Evans, R.; Sluckin, T. J. The Structure and Surface Tension of the Liquid-Vapour Interface of a Model of a Molten Salt. *Mol. Phys.* **1980**, *41* (6), 1355–1372.
- (105) Aguado, A.; Wilson, M.; Madden, P. A. Molecular Dynamics Simulations of the Liquid–Vapor Interface of a Molten Salt. I. Influence of the Interaction Potential. *J. Chem. Phys.* **2001**, *115* (18), 8603–8611.
- (106) Aguado, A.; Scott, W.; Madden, P. A. Molecular Dynamics Simulations of the Liquid–Vapor Interface of a Molten Salt. II. Finite Size Effects and Comparison to Experiment. *J. Chem. Phys.* **2001**, *115* (18), 8612–8619.
- (107) Aguado, A.; Madden, P. A. Molecular Dynamics Simulations of the Liquid–Vapor Interface of a Molten Salt. III. Size Asymmetry Effects and Binary Mixtures. *J. Chem. Phys.* **2002**, *117* (16), 7659–7668.
- (108) Burt, R.; Birkett, G.; Salanne, M.; Zhao, X. S. Molecular Dynamics Simulations of the Influence of Drop Size and Surface Potential on the Contact Angle of Ionic-Liquid Droplets. *J. Phys. Chem. C* **2016**, *120* (28), 15244–15250.
- (109) Guan, Y.; Shao, Q.; Chen, W.; Liu, S.; Zhang, X.; Deng, Y. Dynamic Three-Dimensional Nanowetting Behavior of Imidazolium-Based Ionic Liquids Probed by Molecular Dynamics Simulation. *J. Phys. Chem. C* **2017**, *121* (42), 23716–23726.
- (110) Malali, S.; Foroutan, M. Study of Wetting Behavior of BMIM + /PF 6 – Ionic Liquid on TiO₂ (110) Surface by Molecular Dynamics Simulation. *J. Phys. Chem. C* **2017**, *121* (21), 11226–11233.
- (111) Chen, Q.; Zhang, Y.; Ding, Y. Wettability of Molten Sodium Sulfate Salt on Nanoscale Calcium Oxide Surface in High-Temperature Thermochemical Energy Storage. *Appl. Surf. Sci.* **2020**, *505*, 144550.
- (112) Qiang, W.; Wang, B.; Li, Q.; Wang, W. Molecular Dynamics Simulation of Wetting and Evaporation Characteristics for Sessile Nanofluid Nanodroplets. *Chem. Phys. Lett.* **2018**, *695*, 112–118.
- (113) Li, Y.; Wang, F.; Liu, H.; Wu, H. Nanoparticle-Tuned Spreading Behavior of

- Nanofluid Droplets on the Solid Substrate. *Microfluid. Nanofluidics* **2015**, *18* (1), 111–120.
- (114) Madathil, P. K.; Balagi, N.; Saha, P.; Bharali, J.; Rao, P. V. C.; Choudary, N. V.; Ramesh, K. Preparation and Characterization of Molten Salt Based Nanothermic Fluids with Enhanced Thermal Properties for Solar Thermal Applications. *Appl. Therm. Eng.* **2016**, *109*, 901–905.
- (115) Che Sidik, N. A.; Mahmud Jamil, M.; Aziz Japar, W. M. A.; Muhammad Adamu, I. A Review on Preparation Methods, Stability and Applications of Hybrid Nanofluids. *Renewable and Sustainable Energy Reviews*. 2017, pp 1112–1122.
- (116) Chau, T. T.; Bruckard, W. J.; Koh, P. T. L.; Nguyen, A. V. A Review of Factors That Affect Contact Angle and Implications for Flotation Practice. *Adv. Colloid Interface Sci.* **2009**, *150* (2), 106–115.
- (117) Ribeiro, J. V.; Bernardi, R. C.; Rudack, T.; Stone, J. E.; Phillips, J. C.; Freddolino, P. L.; Schulten, K. QwikMD — Integrative Molecular Dynamics Toolkit for Novices and Experts. *Sci. Rep.* **2016**, *6* (1), 26536.
- (118) Rapaport, D. C.; Blumberg, R. L.; McKay, S. R.; Christian, W. The Art of Molecular Dynamics Simulation. *Comput. Phys.* **1996**, *10* (5), 456.
- (119) Gibbs, J. W. *Elementary Principles in Statistical Mechanics*; 1902.
- (120) Yang, X.; Zhang, H.; Li, L.; Ji, X. Corrections of the Periodic Boundary Conditions with Rectangular Simulation Boxes on the Diffusion Coefficient, General Aspects. *Mol. Simul.* **2017**, *43* (17), 1423–1429.
- (121) Plimpton, S. Fast Parallel Algorithms for Short-Range Molecular Dynamics. *J. Comput. Phys.* **1995**, *117* (1), 1–19.
- (122) Humphrey, W.; Dalke, A.; Schulten, K. VMD: Visual Molecular Dynamics. *J. Mol. Graph.* **1996**, *14* (1), 33–38.
- (123) Chen, H.; Ding, Y.; Tan, C. Rheological Behaviour of Nanofluids. *New J. Phys.* *New J. Phys.* **2007**, *9* (9), 367–367.
- (124) Arthur, O.; Karim, M. A. An Investigation into the Thermophysical and Rheological Properties of Nanofluids for Solar Thermal Applications. *Renew. Sustain. Energy Rev.* **2016**, *55*, 739–755.
- (125) Nunes, V. M. B.; Lourenço, M. J. V.; Santos, F. J. V.; Nieto De Castro, C. A. Viscosity of Molten Sodium Nitrate. *Int. J. Thermophys.* **2006**, *27* (6), 1638–1649.

- (126) Sharma, S. K.; Jotshl, C. K.; Singh, A. Viscosity of Molten Sodium Salt Hydrates. *J. Chem. Eng. Data* **1984**, 29 (3), 245–246.
- (127) Lança, M. J. C.; Lourenço, M. J. V.; Santos, F. J. V.; Nunes, V. M. B.; Nieto De Castro, C. A. Viscosity of Molten Potassium Nitrate. *High Temp. - High Press.* **2001**, 33 (4), 427–434.
- (128) Janz, G. J. Molten Salts Data as Reference Standards for Density, Surface Tension, Viscosity, and Electrical Conductance: KNO₃ and NaCl. *J. Phys. Chem. Ref. Data* **1980**, 9 (4), 791–830.
- (129) Jin, Y.; Cheng, J.; An, X.; Su, T.; Zhang, P.; Li, Z. Accurate Viscosity Measurement of Nitrates/Nitrites Salts for Concentrated Solar Power. *Sol. Energy* **2016**, 137, 385–392.
- (130) Raud, R.; Jacob, R.; Bruno, F.; Will, G.; Steinberg, T. A. A Critical Review of Eutectic Salt Property Prediction for Latent Heat Energy Storage Systems. *Renew. Sustain. Energy Rev.* **2017**, 70, 936–944.
- (131) Zhang, X.; Tian, J.; Xu, K.; Gao, Y. Thermodynamic Evaluation of Phase Equilibria in NaNO₃-KNO₃ System. *J. Phase Equilibria* **2003**, 24 (5), 441–446.
- (132) Gimenez-Gavarrell, P.; Fereres, S. An Experimental Study of the Effect of SiO₂ Nanoparticles on the Phase Change Characteristics of KNO₃-NaNO₃ Mixtures for Thermal Energy Storage. In *Volume 8B: Heat Transfer and Thermal Engineering*; American Society of Mechanical Engineers, 2015; p 9.
- (133) Wei, X.; Wang, Y.; Peng, Q.; Yang, J.; Yang, X.; Ding, J. NO_x Emissions and NO₂ - Formation in Thermal Energy Storage Process of Binary Molten Nitrate Salts. *Energy* **2014**, 74, 215–221.
- (134) Liu, M.; Severino, J.; Bruno, F.; Majewski, P. Experimental Investigation of Specific Heat Capacity Improvement of a Binary Nitrate Salt by Addition of Nanoparticles/Microparticles. *J. Energy Storage* **2019**, 22, 137–143.
- (135) Hu, Y.; He, Y.; Zhang, Z.; Wen, D. Enhanced Heat Capacity of Binary Nitrate Eutectic Salt-Silica Nanofluid for Solar Energy Storage. *Sol. Energy Mater. Sol. Cells* **2019**, 192, 94–102.
- (136) Cingarapu, S.; Singh, D.; Timofeeva, E. V.; Moravek, M. R. Nanofluids with Encapsulated Tin Nanoparticles for Advanced Heat Transfer and Thermal Energy Storage. *Int. J. Energy Res.* **2014**, 38 (1), 51–59.

- (137) Methods for the Calculation of Surface Free Energy of Solids. *J. Achiev. Mater. Manuf. Eng.* **2007**.
- (138) Kozbial, A.; Li, Z.; Conaway, C.; McGinley, R.; Dhingra, S.; Vahdat, V.; Zhou, F.; D'Urso, B.; Liu, H.; Li, L. Study on the Surface Energy of Graphene by Contact Angle Measurements. *Langmuir* **2014**, *30* (28), 8598–8606.
- (139) Quan, X.; Wang, D.; Cheng, P. An Experimental Investigation on Wettability Effects of Nanoparticles in Pool Boiling of a Nanofluid. *Int. J. Heat Mass Transf.* **2017**, *108*, 32–40.
- (140) Nazir, H.; Batool, M.; Bolivar Osorio, F. J.; Isaza-Ruiz, M.; Xu, X.; Vignarooban, K.; Phelan, P.; Inamuddin; Kannan, A. M. Recent Developments in Phase Change Materials for Energy Storage Applications: A Review. *Int. J. Heat Mass Transf.* **2019**, *129*, 491–523.
- (141) Grosu, Y.; Anagnostopoulos, A.; Navarro, M. E.; Ding, Y.; Faik, A. Inhibiting Hot Corrosion of Molten $\text{Li}_2\text{CO}_3\text{-Na}_2\text{CO}_3\text{-K}_2\text{CO}_3$ Salt through Graphitization of Construction Materials for Concentrated Solar Power. *Sol. Energy Mater. Sol. Cells* **2020**, *215*, 110650.
- (142) Gonschorek, G.; Weitzel, H.; Miehe, G.; Fuess, H.; Schmahl, W. W. The Crystal Structures of NaNO_3 at 100 K, 120 K and 563 K. *Zeitschrift für Krist. - Cryst. Mater.* **2000**, *215* (12).
- (143) Adiwidjaja, G.; Pohl, D. Superstructure of α -Phase Potassium Nitrate. *Acta Crystallogr. Sect. C Cryst. Struct. Commun.* **2003**, *59* (12), i139–i140.
- (144) Sheppard, D.; Terrell, R.; Henkelman, G. Optimization Methods for Finding Minimum Energy Paths. *J. Chem. Phys.* **2008**, *128* (13), 134106.
- (145) Martyna, G. J.; Tobias, D. J.; Klein, M. L. Constant Pressure Molecular Dynamics Algorithms. *J. Chem. Phys.* **1994**, *101* (5), 4177–4189.
- (146) Tuckerman, M. E.; Alejandre, J.; López-Rendón, R.; Jochim, A. L.; Martyna, G. J. A Liouville-Operator Derived Measure-Preserving Integrator for Molecular Dynamics Simulations in the Isothermal–Isobaric Ensemble. *J. Phys. A. Math. Gen.* **2006**, *39* (19), 5629–5651.
- (147) Beckers, J. V. L.; Lowe, C. P.; De Leeuw, S. W. An Iterative PPPM Method for Simulating Coulombic Systems on Distributed Memory Parallel Computers. *Mol. Simul.* **1998**, *20* (6), 369–383.

- (148) Van Gunsteren, W. F.; Berendsen, H. J. C. A Leap-Frog Algorithm for Stochastic Dynamics. *Mol. Simul.* **1988**, *1* (3), 173–185.
- (149) Pflieger, N.; Bauer, T.; Martin, C.; Eck, M.; Wörner, A. Thermal Energy Storage – Overview and Specific Insight into Nitrate Salts for Sensible and Latent Heat Storage. *Beilstein J. Nanotechnol.* **2015**, *6*, 1487–1497.
- (150) Janz, G. J.; Bansal, N. P. Molten Salts Data: Diffusion Coefficients in Single and Multi-Component Salt Systems. *J. Phys. Chem. Ref. Data* **1982**, *11* (3), 505–693.
- (151) Janz, G. J.; Krebs, U.; Siegenthaler, H. F.; Tomkins, R. P. T. Molten Salts: Volume 3 Nitrates, Nitrites, and Mixtures: Electrical Conductance, Density, Viscosity, and Surface Tension Data. *J. Phys. Chem. Ref. Data* **1972**, *1* (3), 581–746.
- (152) Zhao, Q.-G.; Hu, C.-X.; Liu, S.-J.; Guo, H.; Wu, Y.-T. The Thermal Conductivity of Molten NaNO₃, KNO₃, and Their Mixtures. *Energy Procedia* **2017**, *143*, 774–779.
- (153) Nagasaka, Y.; Nagashima, A. The Thermal Conductivity of Molten NaNO₃ and KNO₃. *Int. J. Thermophys.* **1991**, *12* (5), 769–781.
- (154) Omotani, T.; Nagasaka, Y.; Nagashima, A. Measurement of the Thermal Conductivity of KNO₃-NaNO₃ Mixtures Using a Transient Hot-Wire Method with a Liquid Metal in a Capillary Probe. *Int. J. Thermophys.* **1982**, *3* (1), 17–26.
- (155) Santini, R.; Tadrist, L.; Pantaloni, J.; Cerisier, P. Measurement of Thermal Conductivity of Molten Salts in the Range 100–500°C. *Int. J. Heat Mass Transf.* **1984**, *27* (4), 623–626.
- (156) Awad, A.; Navarro, H.; Ding, Y.; Wen, D. Thermal-Physical Properties of Nanoparticle-Seeded Nitrate Molten Salts. *Renew. Energy* **2018**, *120*, 275–288.
- (157) Wu, Y.; Li, J.; Wang, M.; Wang, H.; Zhong, Y.; Zhao, Y.; Wei, M.; Li, Y. Solar Salt Doped by MWCNTs as a Promising High Thermal Conductivity Material for CSP. *RSC Adv.* **2018**, *8* (34), 19251–19260.
- (158) Janz, G. J.; Tomkins, R. P. T. Physical Properties Data Compilations Relevant to Energy Storage: IV Molten Salts: Data on Additional Single and Multi-Component Salt Systems. *Natl. Stand. Ref. Data Syst. Natl. Bur. Stand. Rep. NSRDS-NBS 61 Part IV* **1981**.

- (159) Pranami, G.; Lamm, M. H. Estimating Error in Diffusion Coefficients Derived from Molecular Dynamics Simulations. *J. Chem. Theory Comput.* **2015**, *11* (10), 4586–4592.
- (160) Hummer, G. Position-Dependent Diffusion Coefficients and Free Energies from Bayesian Analysis of Equilibrium and Replica Molecular Dynamics Simulations. *New J. Phys.* **2005**, *7*, 34–34.
- (161) Lin, Y. C.; Chen, X. Investigation of Moisture Diffusion in Epoxy System: Experiments and Molecular Dynamics Simulations. *Chem. Phys. Lett.* **2005**, *412* (4–6), 322–326.
- (162) Hoang, V. Van. Molecular Dynamics Simulation of Amorphous SiO₂ Nanoparticles. *J. Phys. Chem. B* **2007**, *111* (44), 12649–12656.
- (163) Lim, T.-C. The Relationship between Lennard-Jones (12-6) and Morse Potential Functions. *Zeitschrift für Naturforsch. A* **2003**, *58* (11).
- (164) Takada, A.; Richet, P.; Catlow, C. R. A.; Price, G. D. Molecular Dynamics Simulations of Vitreous Silica Structures. *J. Non. Cryst. Solids* **2004**, *345–346*, 224–229.
- (165) Bragg, W.; Gibbs, R. E. The Structure of Formula and Formula Quartz. *Proc. R. Soc. A Math. Phys. Eng. Sci.* **1925**, *109* (751), 405–427.
- (166) Devine, R. A. B.; Arndt, J. Si — O Bond-Length Modification in Pressure-Densified Amorphous SiO₂. *Phys. Rev. B* **1987**, *35* (17), 9376–9379.
- (167) Mozzi, R. L.; Warren, B. E. The Structure of Vitreous Silica. *J. Appl. Crystallogr.* **1969**, *2* (4), 164–172.
- (168) Kaliannan, N. K.; Krishnamurthy, K.; Sreerama, S.; Rathnam, A. M. R. J. J. Monte Carlo Simulations of Bulk and Nano Amorphous Silica (a-SiO₂) Melts. *Comput. Mater. Sci.* **2018**, *146*, 90–101.
- (169) Da Silva, J. R. G.; Pinatti, D. G.; Anderson, C. E.; Rudee, M. L. A Refinement of the Structure of Vitreous Silica. *Philos. Mag.* **1975**, *31* (3), 713–717.
- (170) Jo, B.; Banerjee, D. Effect of Solvent on Specific Heat Capacity Enhancement of Binary Molten Salt-Based Carbon Nanotube Nanomaterials for Thermal Energy Storage. *Int. J. Therm. Sci.* **2015**, *98*, 219–227.
- (171) Anagnostopoulos, A.; Alexiadis, A.; Ding, Y. Molecular Dynamics Simulation of Solar Salt (NaNO₃-KNO₃) Mixtures. *Sol. Energy Mater. Sol. Cells* **2019**, *200*,

109897.

- (172) González-Roubaud, E.; Pérez-Osorio, D.; Prieto, C. Review of Commercial Thermal Energy Storage in Concentrated Solar Power Plants: Steam vs. Molten Salts. *Renew. Sustain. Energy Rev.* **2017**, *80*, 133–148.
- (173) Montero de Hijes, P.; Sanz, E.; Joly, L.; Valeriani, C.; Caupin, F. Viscosity and Self-Diffusion of Supercooled and Stretched Water from Molecular Dynamics Simulations. *J. Chem. Phys.* **2018**, *149* (9), 094503.
- (174) Yeh, I.-C.; Hummer, G. System-Size Dependence of Diffusion Coefficients and Viscosities from Molecular Dynamics Simulations with Periodic Boundary Conditions. *J. Phys. Chem. B* **2004**, *108* (40), 15873–15879.
- (175) Engelmann, S.; Hentschke, R. Specific Heat Capacity Enhancement Studied in Silica Doped Potassium Nitrate via Molecular Dynamics Simulation. *Sci. Rep.* **2019**, *9* (1), 7606.
- (176) Shin, D.; Banerjee, D. Enhancement of Specific Heat Capacity of High-Temperature Silica-Nanofluids Synthesized in Alkali Chloride Salt Eutectics for Solar Thermal-Energy Storage Applications. *Int. J. Heat Mass Transf.* **2011**, *54* (5–6), 1064–1070.
- (177) Shin, D.; Banerjee, D. Enhanced Thermal Properties of SiO₂ Nanocomposite for Solar Thermal Energy Storage Applications. *Int. J. Heat Mass Transf.* **2015**, *84*, 898–902.
- (178) Daub, C. D.; Wang, J.; Kudesia, S.; Bratko, D.; Luzar, A. The Influence of Molecular-Scale Roughness on the Surface Spreading of an Aqueous Nanodrop. *Faraday Discuss.* **2010**, *146*, 67.
- (179) Bahadur, R.; Russell, L. M. Effect of Surface Tension from MD Simulations on Size-Dependent Deliquescence of NaCl Nanoparticles. *Aerosol Sci. Technol.* **2008**, *42* (5), 369–376.
- (180) Rushton, M. J. D.; Grimes, R. W.; Owens, S. L. Partial Ordering of Glass Networks Adjacent to Simulated Glass–Crystal Interfaces. *J. Non. Cryst. Solids* **2011**, *357* (16–17), 3278–3287.
- (181) Alexiadis, A.; Kassinos, S. Molecular Simulation of Water in Carbon Nanotubes. *Chem. Rev.* **2008**, *108* (12), 5014–5034.
- (182) Rafiee, J.; Mi, X.; Gullapalli, H.; Thomas, A. V.; Yavari, F.; Shi, Y.; Ajayan, P. M.;

- Korotkar, N. A. Wetting Transparency of Graphene. *Nat. Mater.* **2012**, *11* (3), 217–222.
- (183) Sánchez López, O.; Rosas González, A.; Hernández Castillo, I. Statistical Analysis of Surface Roughness of Machined Graphite by Means of CNC Milling. *Ing. e Investig.* **2016**, *36* (3), 89.
- (184) Khan, S.; Singh, J. K. Wetting Transition of Nanodroplets of Water on Textured Surfaces: A Molecular Dynamics Study. *Mol. Simul.* **2014**, *40* (6), 458–468.
- (185) Lundgren, M.; Allan, N. L.; Cosgrove, T. Modeling of Wetting: A Study of Nanowetting at Rough and Heterogeneous Surfaces. *Langmuir* **2007**, *23* (3), 1187–1194.
- (186) Yaghoubi, H.; Foroutan, M. Molecular Investigation of the Wettability of Rough Surfaces Using Molecular Dynamics Simulation. *Phys. Chem. Chem. Phys.* **2018**, *20* (34), 22308–22319.
- (187) Daub, C. D.; Bratko, D.; Leung, K.; Luzar, A. Electrowetting at the Nanoscale. *J. Phys. Chem. C* **2007**, *111* (2), 505–509.
- (188) Heim, L.-O.; Bonaccorso, E. Measurement of Line Tension on Droplets in the Submicrometer Range. *Langmuir* **2013**, *29* (46), 14147–14153.
- (189) David, R.; Neumann, A. W. Empirical Equation to Account for the Length Dependence of Line Tension. *Langmuir* **2007**, *23* (24), 11999–12002.
- (190) Marmur, A. Line Tension and the Intrinsic Contact Angle in Solid–Liquid–Fluid Systems. *J. Colloid Interface Sci.* **1997**, *186* (2), 462–466.
- (191) Jaffe, R. L.; Gonnet, P.; Werder, T.; Walther, J. H.; Koumoutsakos, P. Water–Carbon Interactions 2: Calibration of Potentials Using Contact Angle Data for Different Interaction Models. *Mol. Simul.* **2004**, *30* (4), 205–216.
- (192) Bruot, N.; Caupin, F. Curvature Dependence of the Liquid-Vapor Surface Tension beyond the Tolman Approximation. *Phys. Rev. Lett.* **2016**, *116* (5), 056102.
- (193) Tolman, R. C. The Effect of Droplet Size on Surface Tension. *J. Chem. Phys.* **1949**, *17* (3), 333–337.
- (194) Bartell, L. S. Tolman's δ , Surface Curvature, Compressibility Effects, and the Free Energy of Drops †. *J. Phys. Chem. B* **2001**, *105* (47), 11615–11618.
- (195) Blokhuis, E. M.; Kuipers, J. Thermodynamic Expressions for the Tolman Length.

- J. Chem. Phys.* **2006**, 124 (7), 074701.
- (196) Marcus, Y. The Compressibility of Molten Salts. *J. Chem. Thermodyn.* **2013**.
- (197) Kanduč, M. Going beyond the Standard Line Tension: Size-Dependent Contact Angles of Water Nanodroplets. *J. Chem. Phys.* **2017**, 147 (17), 174701.
- (198) Ziemnicka-Sylwester, M. Vaporization and Poor Wettability as the Main Challenges in Fabrication of TiB₂-Cu Cermets Studied by SPS. *Metals (Basel)*. **2014**, 4 (4), 623–638.
- (199) Biswas, K.; Sharma, A. S.; Basu, B. On the Densification Mechanisms and Properties of Cu–Pb and Cu–Pb–TiB₂ Nanocomposites Densified Using Spark Plasma Sintering. *Scr. Mater.* **2013**, 69 (2), 122–126.
- (200) Desmaele, E.; Sator, N.; Vuilleumier, R.; Guillot, B. The MgCO₃–CaCO₃–Li₂CO₃–Na₂CO₃–K₂CO₃ Melts: Thermodynamics and Transport Properties by Atomistic Simulations. *J. Chem. Phys.* **2019**, 150 (21), 214503.
- (201) Mechkov, S.; Oshanin, G.; Rauscher, M.; Brinkmann, M.; Cazabat, A. M.; Dietrich, S. Contact Line Stability of Ridges and Drops. *Europhys. Lett.* **2007**, 80 (6), 66002.
- (202) Król, D. J.; Wymysłowski, A.; Allaf, K. N. Adhesion Work Analysis through Molecular Modeling and Wetting Angle Measurement. *Microelectron. Reliab.* **2015**, 55 (5), 758–764.
- (203) Alexiadis, A.; Kassinos, S. The Density of Water in Carbon Nanotubes. *Chem. Eng. Sci.* **2008**, 63 (8), 2047–2056.
- (204) Ugarte, D.; Stöckli, T.; Bonard, J. M.; Châtelain, A.; de Heer, W. A. Filling Carbon Nanotubes. *Appl. Phys. A Mater. Sci. Process.* **1998**, 67 (1), 101–105.
- (205) Ugarte, D.; Chatelain, A.; de Heer, W. A. Nanocapillarity and Chemistry in Carbon Nanotubes. *Science (80-.)*. **1996**, 274 (5294), 1897–1899.

APPENDIX A: CODE FOR SIMULATIONS

A.1 LAMMPS Simulations code

A.1.1 Crystal cell data for NaNO₃

COMPND UNNAMED

AUTHOR GENERATED BY OPEN BABEL 2.3.2

CRYST1 7.414 9.166 7.431 90.00 90.00 90.00 P1 1

HETATM	1	Na	LIG	1	1.854	3.819	5.624	1.00	0.00	Na
HETATM	2	N	LIG	2	1.854	6.918	6.801	1.00	0.00	N
HETATM	3	O	HOH	3	1.854	8.159	6.768	1.00	0.00	O
HETATM	4	O	HOH	4	3.330	6.293	6.800	1.00	0.00	O
HETATM	5	Na	LIG	5	1.854	0.764	1.908	1.00	0.00	Na
HETATM	6	Na	LIG	6	5.561	8.401	5.522	1.00	0.00	Na
HETATM	7	Na	LIG	7	5.561	5.347	1.807	1.00	0.00	Na
HETATM	8	N	LIG	8	1.854	6.830	3.085	1.00	0.00	N
HETATM	9	N	LIG	9	5.561	2.335	4.346	1.00	0.00	N
HETATM	10	N	LIG	10	5.561	2.247	0.630	1.00	0.00	N
HETATM	11	O	HOH	11	1.854	5.589	3.052	1.00	0.00	O
HETATM	12	O	HOH	12	5.561	3.577	4.379	1.00	0.00	O
HETATM	13	O	HOH	13	5.561	1.006	0.663	1.00	0.00	O
HETATM	14	O	HOH	14	0.377	6.293	6.800	1.00	0.00	O
HETATM	15	O	HOH	15	3.330	7.456	3.084	1.00	0.00	O

```

HETATM 16 O HOH 16 7.037 1.710 4.346 1.00 0.00 O
HETATM 17 O HOH 17 4.084 2.873 0.631 1.00 0.00 O
HETATM 18 O HOH 18 7.037 2.873 0.631 1.00 0.00 O
HETATM 19 O HOH 19 4.084 1.710 4.346 1.00 0.00 O
HETATM 20 O HOH 20 0.377 7.456 3.084 1.00 0.00 O
MASTER 0 0 0 0 0 0 0 0 0 20 0 20 0
END

```

A.1.2 Obtain equilibrated molten structure from crystal cell, example for NaNO_3 at 593K

```

#####
# simulation parameters
#####

units          metal
dimension      3
atom_style     full
boundary       p p p

# creation

# Simulation box

# Read data structure in A.1.1
read_data data.nano3

#Replicate cell depending on desired number of atoms
replicate 5 4 5

# Grouping

```

```

group sodiumatoms type 1
group nitrogen type 2
group oxygenatoms type 3
group nano type 1 2 3
mass 1 22.989771

set group sodiumatoms charge 1.00
set group nitrogen charge 0.95
set group oxygenatoms charge -0.65

#####

# interaction

#####

pair_style lj/cut/coul/long 10.0

bond_style harmonic
bond_coeff 1 22.7662 1.2676

angle_style harmonic
angle_coeff 1 4.55323 120.0

improper_style harmonic
improper_coeff 1 2.601847 0

pair_coeff 2 2 0.0056373 2.3
#Na-Na parameters

pair_coeff 1 1 0.0000719 3.04
#N-N parameters

pair_coeff 3 3 0.000018258 2.9
#O-O parameters

pair_coeff 1 2 0.000636648937798532 2.6
#Na-N parameters

pair_coeff 2 3 0.000320820547035254 2.67
#Na-O parameters

pair_coeff 1 3 0.0000362318947889839 2.97
#N-O parameters

```

```

kspace_style pppm 1.0e-5

neighbor 0.3 bin
neigh_modify delay 0 every 1 check yes

#Minimization of Original Structure

minimize 1.0e-15 1.0e-15 100000000000 1000000

thermo 10

thermo_style custom step time fmax fnorm

min_style fire

timestep 0.001

#Dynamic Simulation

thermo 1000
thermo_style custom step time atoms temp press pe ke density vol

# NPH

velocity all create 1200.000 123453123 dist gaussian

#processors. Below fixes are aimed at optimization of processor loads
comm_style brick
balance 1.1 x uniform y uniform z uniform
fix 9 all balance 1000 1.0 shift xyz 30 1.05

# calculation/dynamics

fix 1 all nvt temp 1200.000000 1200.000000 0.002

# dumb topology every 10000 timesteps. Last timestep is equilibrated
structure
dump 7 all custom 10000 nano3.lammpstrj id x y z mass q type

run_style verlet
run 650000

unfix 1

fix 1 all npt temp 1200.000000 593.150000 0.003 iso 1.0 1.0 1.00000

```

```

run_style verlet
run                      850000

unfix 1

fix 1 all nvt temp 593.150000 593.150000 0.002

run_style verlet
run                      200000

unfix 1

write_restart restart.nano3equilibrated

```

A.1.3 Density Calculation

After obtaining the structure from the simulation one should the following line to invoke the equilibrated structure obtained in A.1.2

```
read_restart restart.nano3equilibrated
```

then after setting the force-field and kspace parameters as above the simulation is:

```

variable dens equal density

fix 1 all nvt temp 593.150000 593.150000 0.002

fix 2 all ave/time 100 10 1000 v_dens ave running file density.profile

run_style verlet
run                      200000

```

A.1.4 Radial Distribution

Similar to density but the commands to invoke RDF are:

```

compute myRDF all rdf 100 1 1 2 2 3 3 1 2 1 3 2 3
fix 1 all ave/time 100 1 100 c_myRDF[*] file nano3_lj.rdf mode vector

run 100

```

A.1.5 Thermal conductivity calculation:

Identical to density but the commands for Green-Kubo are:

```
# Input parameters
variable T equal 613.15
variable V equal vol
variable dt equal 0.001
variable p equal 200      # correlation length
variable s equal 5        # sample interval
variable d equal $p*$s    # dump interval

# convert from LAMMPS real units to SI
variable kB equal 1.38064852e-23 # [J/K]** Boltzmann
variable bar2Pa equal 100000.0
variable A2m equal 1.0e-10
variable ps2s equal 1.0e-12
variable convert equal ${bar2Pa}*${bar2Pa}*${ps2s}*${A2m}*${A2m}*${A2m}

fix NVT all nvt temp $T $T 0.005
run 8000

# thermal conductivity calculation

unfix NVT
fix NVE all nve

reset_timestep 0
compute myKE all ke/atom
compute myPE all pe/atom
compute myStress all stress/atom NULL virial
compute flux all heat/flux myKE myPE myStress
variable Jx equal c_flux[1]/vol
variable Jy equal c_flux[2]/vol
variable Jz equal c_flux[3]/vol
fix JJ all ave/correlate $s $p $d &
c_flux[1] c_flux[2] c_flux[3] type auto file J0Jt.dat ave

running
variable scale equal ${convert}/${kB}/${T}/${T}/${V*$s*${dt}
variable k11 equal trap(f_JJ[3])*${scale}
variable k22 equal trap(f_JJ[4])*${scale}
variable k33 equal trap(f_JJ[5])*${scale}
thermo_style custom step temp v_Jx v_Jy v_Jz v_k11 v_k22 v_k33
run 300000
variable k equal (v_k11+v_k22+v_k33)/3.0
variable ndens equal count(all)/vol
print "average conductivity: $k[W/mK] @ $T K, ${ndens} /A^3"
```

A.1.6 Viscosity calculation:

```
# Input parameters
variable T equal 613.15
variable V equal vol
variable dt equal 0.001
variable p equal 200 # correlation length
variable s equal 5 # sample interval
variable d equal $p*$s # dump interval

# convert from LAMMPS real units to SI
variable kB equal 1.38064852e-23 # [J/K]** Boltzmann
variable bar2Pa equal 100000.0
variable A2m equal 1.0e-10
variable ps2s equal 1.0e-12
variable convert equal ${bar2Pa}*${bar2Pa}*${ps2s}*${A2m}*${A2m}*${A2m}

fix 1 all nve
fix 2 all langevin $T $T 0.1 498094

thermo $d
run 20000

velocity all scale $T

unfix 2

# Define distinct components of symmetric traceless stress tensor

reset_timestep 0
variable pxy equal pxy
variable pxz equal pxz
variable pyz equal pyz
fix SS all ave/correlate $s $p $d &
v_pxy v_pxz v_pyz type auto file S0St.dat ave running
variable scale equal ${convert}/(${kB}*T)*V*$s*${dt}
variable v11 equal trap(f_SS[3])*${scale}
variable v22 equal trap(f_SS[4])*${scale}
variable v33 equal trap(f_SS[5])*${scale}
#thermo_style custom step temp press v_pxy v_pxz v_pyz v_v11 v_v22 v_v33

run 30000

variable v equal (v_v11+v_v22+v_v33)/3.0
variable ndens equal count(all)/vol
print "average viscosity: $v [Pa.s] @ $T K, ${ndens} /A^3"
```

A.1.7 Specific heat capacity calculation:

Here the specific heat capacity is calculated based on the difference in enthalpy at $T-T1$ and $T+T1$. In the example below T is 613 and $T1$ 10K. The code calculates the enthalpy at the two points and the volume and density. The obtained enthalpy difference needs to be converted to SI units. The formula should be then used and the results should be divided by the volume and the density (converted in SI) in order to add the mass in the units to obtain J/gK.

```
fix 1 ss npt temp 623.15000 623.15000 $(dt*100) iso 1.0 1.0 $(dt*1000)
```

```
run_style verlet  
run 1250000
```

```
variable toten equal enthalpy  
variable volum equal vol  
variable dens equal density
```

```
fix 3 all ave/time 100 10 1000 v_toten v_volum v_dens ave running file  
enthalpy623.dat
```

```
run_style verlet  
run 2500000
```

```
unfix 1  
unfix 3
```

```
fix 1 ss npt temp 623.15000 603.15000 $(dt*100) iso 1.0 1.0 $(dt*1000)
```

```
run_style verlet  
run 650000
```

```
fix 1 ss npt temp 603.15000 603.15000 $(dt*100) iso 1.0 1.0 $(dt*1000)
```

```
run_style verlet  
run 400000
```

```
write_restart restart.sssio2largeNPTready613
```

```
run_style verlet  
run 250000
```

```
fix 3 all ave/time 100 10 1000 v_toten v_volum v_dens ave running file  
enthalpy603.dat
```

```
run_style verlet  
run 2500000
```

A.1.8 Obtain Amorphous Silica Bulk from randomly generated topology and check RDF

```
#####  
# parameters  
#####  
  
units          metal  
dimension      3  
atom_style     full  
boundary       p p p  
  
# creation  
  
# Simulation box  
region 2 block 0.0 40.0 0.0 40.0 0.0 40.0  
  
# Two atom type Si and O  
create_box 2 2  
  
# Here one should calculate based on expected density how many atoms of  
each species should there be in the desired volume defined in the  
simulation box  
  
create_atoms 1 random 1482 1231 2  
create_atoms 2 random 741 12321 2  
  
# Grouping  
  
group oxygen type 1  
group silicon type 2  
group silica type 1 2  
  
set group silicon charge 1.7  
set group oxygen charge -0.85  
  
mass 1 15.9999  
mass 2 28.085  
  
variable totmas equal mass(silica)
```

```

#####
# interaction
#####

pair_style lj/cut/coul/long 10.0

pair_coeff 2 2 0.0017345 3.3
#Si-Si parameters

pair_coeff 1 1 0.02536852 2.7
#O-O parameters

pair_coeff 1 2 0.000100479 3.0
#Si-O parameters

kspace_style ppm 1.0e-5

neighbor 0.2 bin
neigh_modify delay 0 every 1 check yes

#Minimization of Original Structure

minimize 1.0e-15 1.0e-15 10000000000 100000

thermo 10

thermo_style custom step time fmax fnorm

min_style fire

neighbor 0.3 bin
neigh_modify delay 0 every 1 check yes

#Dynamic Simulation

thermo 1000
thermo_style custom step time atoms temp press pe ke density v_totmas
vol

velocity all create 2000.000 123453123 dist gaussian

#processors
comm_style brick
balance 1.1 x uniform y uniform z uniform

```

```
# calcul(s)

timestep          0.0005

fix 9 all balance 1000 1.0 shift xyz 30 1.05

fix 1 all nvt temp 2000.000000 2000.000000 0.200

dump 1 all custom 50000 sio2substrate.lampstrj id x y z mass q type

run_style verlet
run              20000

unfix 1

fix 1 all npt temp 2000.000000 623.000000 0.06000 iso 1.0 1.0 1.00000

run_style verlet
run              1350000

unfix 1

write_restart restart.sio2forcp

fix 1 all npt temp 623.00000 623.00000 0.0500 iso 1.0 1.0 1.00000

run_style verlet
run 450000

unfix 1

fix 1 all nvt temp 623.00000 623.00000 0.200

run_style verlet
run              300000

unfix 1
```

```

compute myRDF all rdf 100 1 1 2 2 1 2
fix 1 all ave/time 100 1 100 c_myRDF[*] file asio2cube.rdf mode vector

run 100

```

A.2 MATLAB Contact angle calculation program

Functions:

- `% read_LAMMPS_traj`: reads a LAMMPS trajectory file and returns the positions of centre of masses of water molecules.
- `% hit_and_count`: runs hit and count algorithm to identify points in liquid droplet from those in the gas phase.
- `% fine_precision`: applied the fine precision droplet identification process to remove near-droplet gas molecules.
- `% contact_angle`: calculates the contact angles along the contact line using
- `% convex_hull`. This function also returns the area of the base of the droplet and the area of corresponding triangles used to calculate each contact angle value.
- `% weighted_distribution`: calculates weighted histogram of contact angles according to the area of corresponding triangles

The following example is to calculate the contact angle of NaNO_3 on MgO using the trajectory files obtained for LAMMPS through timesteps 4000000 to 43000000.

```

for rep = 45400000:1000000.0:45500000.0

trajName = 'C:\...\Contact-angle-calculation-
master\nano3mgo.lammpstrj';
% This format_spec is needed when reading LAMMPS
trajectories in the read_LAMMPS_traj function.
format_spec = '%f %f %f %f %f';
StartStep = 0+rep;
EndStep = StartStep;

```

```

step = 1000000;

% Parameters of hit-and-count function
binsize=2;
numer_atom_in_bin=5;

% Parameters of fine_percision function
% hit and count step is usually sufficient
fine_percision_check = 1; % calls fine_percision function
if is 1
delta_R = 5;
R_step = 1;

% Draws graphs corresponding to each step for the first
timestep. It is recommended to check if parameters droplet
identification process are adjusted properly.
graphcheck = 0;

% Triangles with at least one vertex position lower than
z_min*max(z) are contributing in the contact angle
calculation.
z_min = 0.08;

% This parameter is used to recognize triangles
contributing to the area of % the base of the droplet.
precision = 1.0;

Distribution=[];
Weight=[];
BaseA = 0;

for tt = StartStep:step:EndStep

    fprintf('Current time step = %d\r', tt);
    Filename = sprintf('%s.%d',trajName,tt); %trajectory
file name

    % Reading box dimentions to calculates centre of mass
of water
    % molecules correctly.

    if (tt == StartStep)
        fileID = fopen(Filename, 'r');
        if (fileID < 0)
            fprintf('can not open %s file',Filename);
            break;
        end
        %reading box sizes

```

```

header = textscan(fileID, '%s',9,'delimiter',
'\n');
data = textscan(header{1}{6}, '%f %f');
Box_x = data{2}-data{1};
data = textscan(header{1}{7}, '%f %f');
Box_y = data{2}-data{1};
data = textscan(header{1}{8}, '%f %f');
Box_z = data{2}-data{1};
fclose(fileID);
end

[fileID,x_org,y_org,z_org] =
read_LAMMPS_traj(Filename,Box_x,...
Box_y,Box_z,format_spec);

if (fileID < 0)
fprintf('can not open %s file',Filename);
break;
end

% Drawing the droplet before applying hit-and-run
if (tt == StartStep && graphcheck == 1)
figure;
scatter3(x_org,y_org,z_org,...
'MarkerEdgeColor','k',...
'MarkerFaceColor',[0 .25 .25]);
view(45,45)
title('original');
size1 = size(x_org,1);
axis tight
end

% Applying hit and count method to remove outliers
[x_final,y_final,z_final] = hit_and_count(x_org,...
y_org,z_org,binsize,numer_atom_in_bin);

if (tt == StartStep && graphcheck == 1)
figure;
scatter3(x_final,y_final,z_final,...
'MarkerEdgeColor','k',...
'MarkerFaceColor',[0 .25 .25]);
view(45,45)
size2 = size(x_final,1);
str = sprintf('After hit-and-count (%d points
were removed) ', ...
size1-size2);
title(str);

```

```

        axis tight
    end

    % Applying fine precision method to remove near
    droplet outliers
    if (fine_precision_check == 1)
        [x_final,y_final,z_final] =
fine_precision(x_final,y_final,...
                z_final,R_step,delta_R);
    end

    if (tt == StartStep && graphcheck == 1)
        figure;
        scatter3(x_final,y_final,z_final,...
                'MarkerEdgeColor','k',...
                'MarkerFaceColor',[0 .25 .25]);
        view(45,45)
        size3 = size(x_final,1);
        str = sprintf('After hit-and-count and fine-
precision (%d points were removed)', ...
                size2-size3);
        title(str);
        axis tight
    end

    % Calculating contact angle distribution and
    interfacial area using convex hull
    [K,V,angle,BaseA_temp] =
contact_angle(x_final,y_final,z_final,...
                z_min,precision);

    if (tt == StartStep && graphcheck == 1)
        figure;
        hold on;

        trisurf(K,x_final,y_final,z_final,'facecolor','r','faceal
pha',0.5)
        scatter3(x_final,y_final,z_final,...
                'MarkerEdgeColor','k',...
                'MarkerFaceColor',[0 .75 .75], ...
                'MarkerFaceAlpha',0.5);
        view(45,45)
        axis tight
    end

    BaseA = BaseA + BaseA_temp;

```

```

    Distribution = cat(2,Distribution,angle(1,:));
    Weight = cat(2,Weight,angle(2,:));

    % Calculating weighted histogram of angular values

end

fprintf('\n');

w = weighted_distribution(Distribution,Weight);
BaseA = 0.5*BaseA/((EndStep-StartStep)/step+1);

angle = 0:180;
s0=w;
s1=conv(w,hanning(30),'same');

theta_ave = sum(angle.*w)/sum(w);
disp(theta_ave);

clear;
fclose('all');
close('all');

end

```

hit_and_count

```

function [x_final,y_final,z_final] =
hit_and_count(x_org,y_org,z_org,...
    binsize,numer_atom_in_bin)
% binning of the data using binsize

x_bin=floor(x_org/binsize)+1;
y_bin=floor(y_org/binsize)+1;
z_bin=floor(z_org/binsize)+1;

% applying hit-and-run in X direction
B=unique(x_bin);
C=histc(x_bin(:),B);
e=find(C>=numer_atom_in_bin);
KK=find(x_bin>=B(e(1)) & x_bin<=B(e(end)));

x=x_bin(KK);
y=y_bin(KK);
z=z_bin(KK);

```

```

% ID_drop=ID_org(KK);
% Type_drop=Type_org(KK);
x_drop=x_org(KK);
y_drop=y_org(KK);
z_drop=z_org(KK);

% applying hit-and-run in Y direction
B=unique(y);
C=histc(y(:),B);
e=find(C>=numer_atom_in_bin);
KK=find(y>=B(e(1)) & y<=B(e(end)));

x=x(KK);
y=y(KK);
z=z(KK);
% ID_drop=ID_drop(KK);
% Type_drop=Type_drop(KK);
x_drop=x_drop(KK);
y_drop=y_drop(KK);
z_drop=z_drop(KK);

% applying hit-and-run in Z direction
B=unique(z);
C=histc(z(:),B);
e=find(C>=numer_atom_in_bin);
KK=find(z>=B(e(1)) & z<=B(e(end)));

x=x(KK);
y=y(KK);
z=z(KK);
% ID_final=ID_drop(KK);
% Type_final=Type_drop(KK);
x_drop=x_drop(KK);
y_drop=y_drop(KK);
z_drop=z_drop(KK);

x_final=x_drop;
y_final=y_drop;
z_final=z_drop;

end

fine_precision

```

```

function [x_final,y_final,z_final] =
fine_percision(x_final,y_final,...
    z_final,R_step,delta_R)

dx_ave=max(x_final)-min(x_final);
dy_ave=max(y_final)-min(y_final);

D=max(dx_ave,dy_ave);
d=D/2;
Z_max=max(z_final);

%radius calculation
R=(d.^2+Z_max.^2)./(2*Z_max);
x_ave=min(x_final)+dx_ave/2;
y_ave=min(y_final)+dy_ave/2;
z_ave=Z_max-R;
%Find the distance from origin of the remaining points
% after his-and-count
l2=zeros(size(x_final));
for j=1:length(l2)
    l2(j)= sqrt((x_final(j)-x_ave).^2+...
        (y_final(j)-y_ave).^2+(z_final(j)-z_ave).^2);
end
%Define radius search region for evaluation of
scattered points
R_interval=R-R_step*delta_R:delta_R:R+R_step*delta_R;
R_interval(end)=R_interval(end)+3;

% define three regions:smaller than search zone radius,
% search zone and bigger than search limit radius.

%First remove bigger than limit radius data
e=find(l2<R_interval(end));
x_final=x_final(e);
y_final=y_final(e);
z_final=z_final(e);
l2=l2(e);
%Second keep data less than minimum radius evaluation
% (do not touch)
e=find(l2<R_interval(1));
x_pass=x_final(e);
y_pass=y_final(e);
z_pass=z_final(e);

%Third evaluate data in the search zone for further
action
e=find(l2>=R_interval(1) & l2<=R_interval(end));

```

```

x_zone=x_final(e);
y_zone=y_final(e);
z_zone=z_final(e);
l2=l2(e);

x_temp=0;
y_temp=0;
z_temp=0;

for j=1:length(R_interval)-1
    e=find(l2 >= R_interval(j) & l2 <= R_interval(j+1));
    x=x_zone(e);
    y=y_zone(e);
    z=z_zone(e);

    for m=1:length(x)
        count=0;
        for n=2:length(x_zone)
            distance=sqrt((x(m)-x_zone(n)).^2+ ...
                (y(m)-y_zone(n)).^2 ...
                +(z(m)-z_zone(n)).^2);
            if (distance<4.5 && distance>0)
                count=count+1;
            end
        end
        if count>=1
            x_temp=[x_temp;x(m)];
            y_temp=[y_temp;y(m)];
            z_temp=[z_temp;z(m)];
        end
    end
end

x_final=[x_pass;x_temp(2:end)];
y_final=[y_pass;y_temp(2:end)];
z_final=[z_pass;z_temp(2:end)];
end

```

weighted_distribution

```

function w = weighted_distribution(Distribution,Weight)

D=find(Distribution>-1);

```

```

% calculating weighted histogram according to the area of
triangles
edges = [0:180];
vals = Distribution(D);
weights = Weight(D);

Nedge = length(edges);
w = zeros(size(edges));

for n = 1:Nedge-1
    ind = find(vals >= edges(n) & vals < edges(n+1));
    if ~isempty(ind)
        w(n) = sum(weights(ind));
    end
end

ind = find(vals == edges(end));
if ~isempty(ind)
    w(Nedge) = sum(weights(ind));
end
end

```

convex_hull

```

function [V,S] = VS_Fan(x_final,y_final,z_final);

[K,V] =
convhull(x_final,y_final,z_final,'simplify',true);

S = sum(sqrt(sum(( ...
    [y_final(K(:,1)).*z_final(K(:,2)) -
z_final(K(:,1)).*y_final(K(:,2)) ...
    z_final(K(:,1)).*x_final(K(:,2)) -
x_final(K(:,1)).*z_final(K(:,2)) ...
    x_final(K(:,1)).*y_final(K(:,2)) -
y_final(K(:,1)).*x_final(K(:,2))] + ...
    [y_final(K(:,2)).*z_final(K(:,3)) -
z_final(K(:,2)).*y_final(K(:,3)) ...
    z_final(K(:,2)).*x_final(K(:,3)) -
x_final(K(:,2)).*z_final(K(:,3)) ...
    x_final(K(:,2)).*y_final(K(:,3)) -
y_final(K(:,2)).*x_final(K(:,3))] + ...
    [y_final(K(:,3)).*z_final(K(:,1)) -
z_final(K(:,3)).*y_final(K(:,1)) ...

```

```

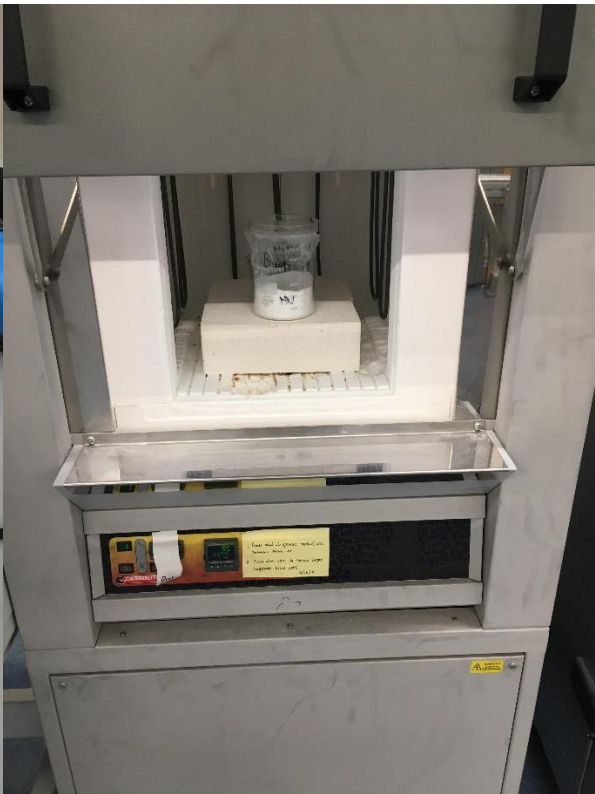
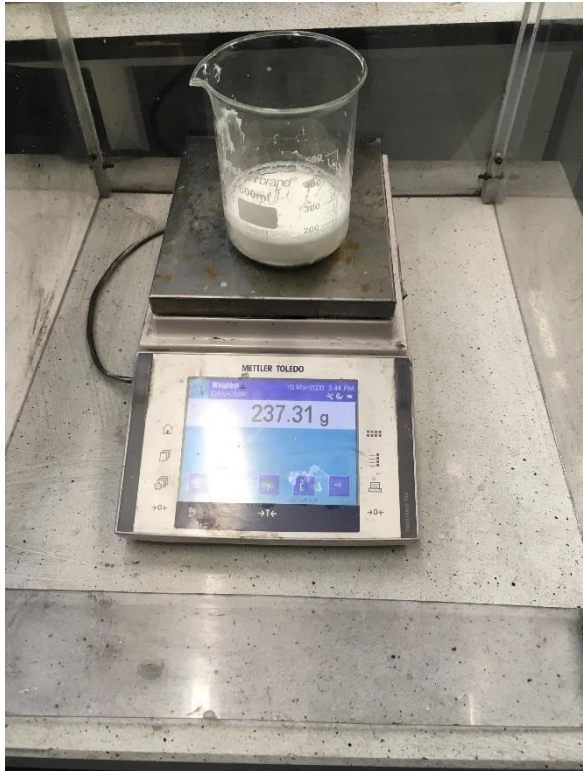
z_final(K(:,3)).*x_final(K(:,1)) -
x_final(K(:,3)).*z_final(K(:,1)) ...
x_final(K(:,3)).*y_final(K(:,1)) -
y_final(K(:,3)).*x_final(K(:,1))] ...
.^2,2))/2;

```

```
end
```

APPENDIX B: SAMPLE PREPERATION AND EQUIPMENT

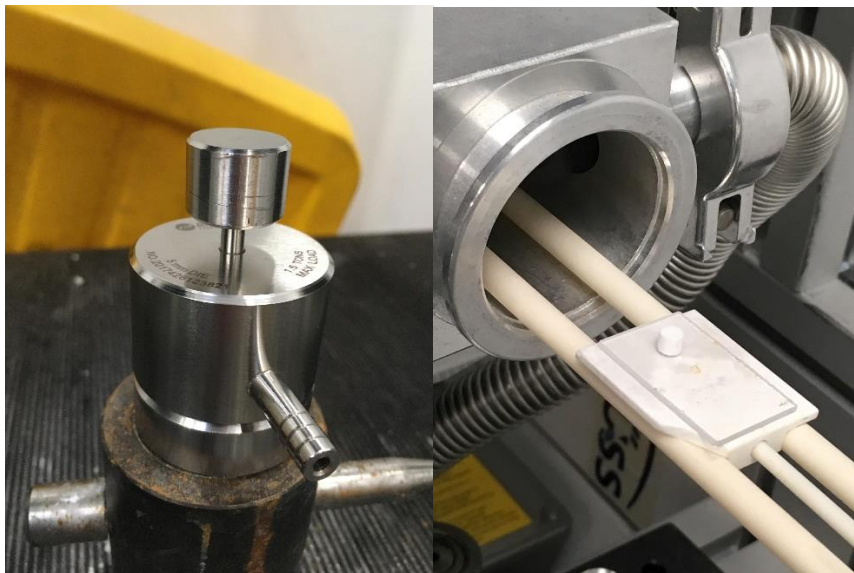
Preparation of binary salt nanofluid. The dried salt is weighted (top left) and melted in the furnace at 390 °C (top right) to produce the eutectic. Then the nanoparticles are added and the sample is sonicated in water (2nd row left). The sonicated mixture is then dried in the oven (2nd row right) and then milled bottom row.





Preparation of pellets for contact angle measurements:

The sample is firstly milled (top left) then placed in the compression dye (top right) and compressed (bottom left), after which it is introduced in the CA sample holder (bottom right)



DSC sample preparation:

The DSC crucible is first measured without the salt (top left). Then the salt is placed in the crucible and it is compressed (top right). The produced crucible (bottom left) is weighted again and then placed in the DSC (bottom right)

